



**University of
Zurich**^{UZH}

Soil Erosion and Age Determination of Soils in a Forest-steppe Ecosystem in Cluj-Napoca, Romania

GEO 511 Master's Thesis

Author

Dario Püntener
15-710-288

Supervised by

Prof. Dr. Markus Egli
Prof. Dr. Pavel Samonil (pavel.samonil@vukoz.cz)

Faculty representative

Prof. Dr. Markus Egli

20.09.2021

Department of Geography, University of Zurich



**University of
Zurich**^{UZH}

Department of Geography

Soil Erosion and Age Determination of Soils in a Forest-steppe Ecosystem in Cluj-Napoca, Romania

GEO 511 Master's Thesis

Author

Dario Püntener

15-710-288

Supervised by:

Prof. Dr. Markus Egli Department of Geography,
University of Zurich

Prof. Dr. Pavel Šamonil VUKOZ/Department of Forest Botany,
Dendrology and Geobiocoenology,
Mendel University in Brno, CZ

20.09.2021

Department of Geography, University of Zurich

Abstract

Large parts of Central and Eastern Europe are covered by extremely biodiverse forest-steppe landscapes. For many of these sites, there is a presumption that they have existed for very long periods of time, despite a climatic suitability for forest vegetation. The forest-grasslands around the city of Cluj-Napoca in Transylvania, Romania, were studied to find evidence of such a Holocene continuity of grasslands with open patches of forest. Three sites currently covered with grass vegetation show evidence of soil polygenesis. Chemical soil properties as well as the presence of thick root channels are indications of former forest cover. This may be an indication of the change in ground-covering vegetation that has taken place in the course of soil formation.

A minimum soil age was calculated for the four sites investigated. The investigated soils show relatively high ages between 20 ka to about 125 ka, indicating an onset of soil genesis before the onset of the Holocene.

In addition, erosion rates were calculated on different time scales. The calculated long-term erosion rates for the entire period since the onset of soil formation of the present-day soils range between $0.18 \text{ t ha}^{-1} \text{ a}^{-1}$ and $0.78 \text{ t ha}^{-1} \text{ a}^{-1}$. The short-term erosion rates of the last 60 years or so are many times higher and in some cases ten times higher between $1.35 \text{ t ha}^{-1} \text{ a}^{-1}$ and $5.4 \text{ t ha}^{-1} \text{ a}^{-1}$. These large differences are an indication of the large, mainly anthropogenic, threats posed by soil erosion to these ecosystems.

Contents

1	Introduction	1
1.1	General Introduction	1
1.2	Holocene Continuity of Forest-steppe Ecosystems	1
1.3	Objectives and Hypotheses	2
1.4	Study Area	4
1.4.1	Sampling Sites	5
2	Methods	6
2.1	Terrestrial Cosmogenic Nuclides	6
2.2	Surface Exposure Dating	7
2.3	Exposure Dating and Long-time erosion rate: Tor exhumation process and in-situ ^{10}Be	8
2.3.1	Sample Preparation for in-situ ^{10}Be Analysis	8
2.3.2	Age modelling using exposure in-situ ^{10}Be	9
2.4	Meteoritic ^{10}Be	9
2.4.1	Sample Preparation for meteoritic ^{10}Be Analysis	10
2.4.2	Soil Age Modelling using Meteoritic ^{10}Be	11
2.4.3	Long- and Mid-term Soil Erosion Rates using Meteoritic ^{10}Be	12
2.5	Fallout Radionuclides	12
2.5.1	Sample Preparation for $^{239+240}\text{Pu}$ Analysis	13
2.5.2	Models for $^{239+240}\text{Pu}$ Inventories and Soil Redistribution Rate Calculations	13
2.6	Long-term Soil Erosion Determination using Soil Formation Modelling	16
2.6.1	Determination of Grain Size Distribution	17
2.7	Elemental Composition	17
2.8	Field Sampling Strategies	17
2.8.1	In-situ ^{10}Be	17
2.8.2	Meteoritic ^{10}Be	18
2.8.3	$^{239+240}\text{Pu}$	18
3	Results	19
3.1	Soil Profiles	19
3.2	Bulk Density	21
3.3	Elemental Composition	22

3.4	$^{239+240}\text{Pu}$ Activities	28
3.5	$^{239+240}\text{Pu}$ Inventories	28
3.6	Short-term Erosion Rates using $^{239+240}\text{Pu}$	31
3.7	In-Situ ^{10}Be Inventory	36
3.8	Surface Exposure Age using In-Situ ^{10}Be	36
3.9	Long-term Erosion Rate using In-Situ ^{10}Be	37
3.10	Meteoritic ^{10}Be Inventory	37
3.11	Soil Age Estimation using Meteoritic ^{10}Be	38
3.12	Long-term Soil Erosion Rates using Meteoritic ^{10}Be	40
3.13	Grain Size Distribution	42
3.14	Long-term Soil Erosion Determination using Soil Formation Modelling	44
4	Discussion	45
4.1	Soil Profiles	45
4.2	Fallout Nuclides	46
4.2.1	$^{239+240}\text{Pu}$ Inventory	46
4.2.2	Erosion Rate	47
4.3	Meteoritic ^{10}Be	50
4.3.1	Meteoritic ^{10}Be Inventory	50
4.3.2	Soil Age Determination with Meteoritic ^{10}Be	51
4.3.3	Long-term Soil Erosion Rate with Meteoritic ^{10}Be	53
4.4	In-situ ^{10}Be	54
4.4.1	In-situ ^{10}Be Age Determination	54
4.4.2	In-situ ^{10}Be Erosion Rate Determination	54
4.5	Erosion Rate from Soil Formation Modelling	55
4.6	Comparison of Different Soil Erosion Rates	55
4.6.1	Comparison of the Long-term Erosion Rates	55
4.6.2	Comparison Long-term Erosion Rates – Short-term Erosion Rates	56
4.7	Holocene Continuity	57
5	Conclusions, Outlook and Perspectives	58
A	Appendix	69

List of Figures

1	Dry Grasslands North of the city of Cluj-Napoca with a very high plant diversity, with the highest known number of individual species on a scale of 0.1 m ² and 10m ²	5
2	Location of the four soil profiles 1 - 4, the outcrop sites and the control/reference site around the city of Cluj-Napoca, Romania. The inset-map shows the location of Cluj County within Romania.	6
3	Rock sampling strategy for in situ ¹⁰ Be analysis	18
4	Soil Profile 1 CJ-1	19
5	Soil Profile 2 CJ-2	19
6	Soil Profile 3 CJ-3	20
7	Soil Profile 4 CJ-4	21
8	Bulk density of the different soil profiles with increasing depth	22
9	Elemental composition of the individual sites with depth.	26
10	Content of crystalline Al and Fe forms of the different soil profile samples with depth. The amount is the difference of the amount of the dithionite-extractable element and the amount of the oxalate-extractable element forms.	27
11	²³⁹⁺²⁴⁰ Pu inventories [Bq m ⁻²] with depth [cm] for the control site (a) and all four sample sites (b, c, d, e). The value of each depth increment is the average of all individual samples of the same depth, with variation shown by the whiskers. . .	30
12	Boxplot of ²³⁹⁺²⁴⁰ Pu inventories of the individual sampling sites CJ-1, CJ-2, CJ-3, CJ-4 and the reference site CJ-C at four different depth increments a) 0 – 5 cm, b) 5 – 10 cm, c) 10 – 15 cm, d) 15 – 20 cm. The bold line indicates the median, the whiskers/error bars indicate the standard deviation. The dots represent outlier measurements.	32
13	Boxplot of all measured erosion rates calculated with different models (IM (P=1, 1.2, 1.5), PDM, MODERN) for each sample site. The horizontal line in the box is the median, the x in the box is the mean of the measurements. For Site CJ-2, one outlier with a value of 21.8 t ha ⁻¹ a ⁻¹ is not depicted.	34
14	Reference Depth Profiles and Plotted Integral Function with solution of each sample site depicted as a vertical red line, a) CJ-1, b) CJ-2, c) CJ-3, d) CJ-4.	35

15	Concentrations of meteoric ^{10}Be as a function of depth below surface. The vertical error bars indicate the individual depth increment, the horizontal error bars the standard deviation of the content of ^{10}Be in the corresponding depth increment.	39
16	Soil grain size distribution of the examined samples as percentage of the total soil weight. The individual soil profile number and the corresponding soil horizons are given in brackets after the sample name.	42
17	Proportions of the different grain size distribution with depth for the profiles a) CJ-1 (A1, A2, C), b) CJ-2 (A1, A3, C), c) CJ-3 (A1, A3, C), d) CJ-4 (Am, Btg, C) . . .	43
18	Correlation of the different erosion rates calculated using three different modelling approaches: PDM (Walling and He, 1999), IM (Lal et al., 2013) and MODERN (Arata et al., 2016b)	49

List of Tables

1	Location and use of the sample and reference sites around Cluj-Napoca	6
2	Measured and averaged $^{239+240}\text{Pu}$ inventories of the control site and the sample sites, including standard deviations. The average cumulative inventory shows the sum of all average values of each soil profile.	29
3	Results of the statistical comparison of $^{239+240}\text{Pu}$ inventories at the sample sites with the inventories at the reference site on different depth increments. Data pairs with a statistically significant difference ($p \leq 0.05$) are marked with an asterisk (*).	31
4	Overview of the calculated erosion rates and their standard deviation from different modelling approaches using fallout $^{239+240}\text{Pu}$. IM = Inventory Model (Lal et al., 2013); PDM = Profile Distribution Model (Walling and Quine, 1990; Zhang et al., 1990), MODERN = Modelling Deposition and Erosion rates with RadioNuclides (Arata et al., 2016b).	34
5	Measured in-situ ^{10}Be content of the three samples of sample site CJ-Be1. The error includes the AMS standard error.	36
6	Exposure ages of the three sample sites calculated using the cosmogenic nuclide online calculator v3.0 (see Balco et al., 2008 for v. 1.0). First results show exposure age without erosion, second results with an erosion rate of 1mm ka^{-1} . The internal error contains the measurements uncertainties of the nuclide concentration, the external error contains measurement uncertainties and nuclide production rate uncertainties.	37
7	Meteoric ^{10}Be concentrations of the individual soil horizons of each sampling site.	40
8	Estimated soil ages in ka calculated using formula 1 by Maejima et al. (2005) with two different values for the average annual precipitation rate of ^{10}Be (q).	41
9	Mid- and long-term soil erosion rates calculated with two different modelling approaches. For each approach, two different values for the average annual ^{10}Be precipitation rate q were used to calculate soil erosion.	42
10	input variables and the soil erosion rate calculated from the modelled theoretical soil depth. d_{50} is the median soil particle size calculated from the measurements of the respective soil profile.	44
11	Summary of all long-term erosion rates for the four soil sites calculated using different approaches, and the average long-term soil erosion rate of all methods.	56

12	Average elemental composition from dithionite and oxalate extraction method of the individual sample sites and for all soil horizons.	69
13	Elemental composition from dithionite and oxalate extraction method of the individual sample sites and for all soil horizons, with two duplicates for each sample.	70
14	Measured meteoric ^{10}Be Inventory and inventory corrected to sample preparation blank.	71
15	Measured in-situ ^{10}Be values and corrected to blank preparation sample.	72
16	Input data for the in-situ ^{10}Be exposure age calculation	72
17	Grain size distribution of a subset of soil samples.	73
18	Measured and corrected plutonium contents and activities, batch 1.	74
19	Measured and corrected plutonium contents and activities, batch 2.	75
20	Measured and corrected plutonium contents and activities, batch 3	76
21	Short-term soil erosion rate calculated with fallout $^{239+240}\text{Pu}$	77

Abbreviations

a	Latin: annum = year; ka = kilo years = 1000 years; Ma = mega years = 10 ⁶ years
AMS	Accelerator mass spectrometry
ANOVA	Analysis of variance
BP	Before Present (Present = year 1950)
CZ	Czech Republic
EDTA	Ethylenediaminetetraacetic acid
ETH	Eidgenössische Technische Hochschule Zürich
FRN	Fallout radionuclides
HCl	Hydrochloric acid
HF	Hydrofluoric acid
HNO ₃	Nitric acid
IM	Inventory Model
MODERN	Modelling Deposition and Erosion rates with RadioNuclides
NaOH	Sodium hydroxide
NH ₄ OH	ammonium hydroxide
NIST	National Institute of Standards and Technology
m a.s.l.	Meters above sea level
PDM	Profile Distribution Method
QQQ-ICP-MS	Triple Quadrupole - Inductively Coupled Plasma - Mass Spectrometry
SD	Standard deviation
VUKOZ	Výzkumný ústav Silva Taroucy pro krajinu a okrasné zahradnictví, veřejná výzkumná instituce
WRB	World Reference Base for Soil Resources

1 Introduction

1.1 General Introduction

Large parts of Eastern Europe are covered with very biodiversity rich European forest-steppe ecosystems. With growing evidence, these forest-steppes appear to exist on a millennium scale, despite strong influences by human activities over very long periods of time (Feurdean et al., 2018; Magyari et al., 2010). In addition to this, despite a climatic suitability for closed forest in many of these regions a Holocene continuity of forest-steppe vegetation has been assumed in recent studies, with disturbances as driver for this continuity (Feurdean et al., 2015, 2018). This Holocene continuity would have effects on different aspects of modern biodiversity discussions such as the impact of human behaviour on ecosystems. Furthermore, this would influence different theories in global change biology (Pecl et al., 2017) and modern strategies of nature conservation with the aim of preserving the current biodiversity of an ecosystem (Dawson et al., 2011).

The area around the city of Cluj-Napoca in Romanian Transylvania is one of the areas where the high biodiversity of species in grassland ecosystems would argue for a covering of the area with a forest-steppe landscape over longer periods during soil genesis (Hájek et al., 2020).

Soil erosion as a source of disturbances is a driving force in shaping entire ecosystems (Ionita et al., 2007). Reciprocally, different vegetation covers influence the amplitude of erosion (IAEA, 2014). Differences in erosion rates over different time periods can therefore be an indication of changes in individual ecosystems, the climate to which the area is subject, and human activity and influence.

1.2 Holocene Continuity of Forest-steppe Ecosystems

The European Forest Steppe lies between two ecosystem types, and it is characterised by a transition of one ecosystem into the other. As a transition between temperate forests and temperate grasslands, this ecosystem is characterised by a different composition between alternating forest and grasslands (Feurdean et al., 2015). The current climatic conditions in these regions would actually support the formation of closed forests, because unlike in a steppe landscape, there is no summer drought as it is typical of these steppe ecosystems (Magyari et al., 2010). One opinion that is held is that this open canopy forest-steppe zone is purely a product of human deforestation activities and thus only a secondary habitat (Feurdean et al., 2018). Pollen analyses indicate a high proportion of grassland plants for large parts of the entire Holocene, with varying proportions of total vegetation in each case (Feurdean et al., 2015, 2018; Magyari

et al., 2010). A maximum expansion of grass vegetation was found at the beginning of the Holocene, with an increase in forest cover between 9000 cal a BP and 4500 cal a BP. Specifically, an existence of grasslands prior to the Neolithic and therefore prior to human influence was also detected (Feurdean et al., 2018). In addition, a phylogeographic analysis of grasslands indicates a continuous existence of grass vegetation, with very little genetic difference between populations over a geographically large space (Feurdean et al., 2018), as well as an extremely large biodiversity of grass vegetation plants that can only evolve over a long period of time and in a continuous ecosystem (Dengler et al., 2012; Willner et al., 2019; Hájek et al., 2020). From a pedological point of view, the distribution of very old strongly developed Chernozem soils, e.g. in Transylvania (Pendea et al., 2009), speaks for the continuity of open forest-steppe ecosystems (Feurdean et al., 2018).

The conditions that enabled this continuity of open forest-grasslands were, among others, climatic conditions, especially drier conditions with hot summers at the beginning of the Holocene favoured the formation of grasslands over closed forest vegetation (Feurdean et al., 2018). In addition, there is evidence of frequent fires, from which grass vegetation can recover many times faster than tree vegetation, leading to a site advantage in the longer term (Magyari et al., 2010; Feurdean et al., 2015). The appearance of the first humans in these areas may have had an influence on the increased forestation that took place at the same time. By colonising the still open areas, the first Neolithic humans stopped a further spread of the forests into the remaining open areas (Feurdean et al., 2018).

Feurdean et al. (2018) identified three different types of grasslands that make up the open grasslands in forest-steppe ecosystems in eastern Europe in different proportions. The first type (primary grasslands I) are primary grasslands on poorly developed soils, such as skeletal soils. The second type (primary grasslands II) are very old grasslands on potentially wooded areas that have been kept open by disturbances such as fire, erosion or grazing by large herbivorous mammals. The third type (semi-natural grasslands) are those converted from forest to grassland by early (mainly Neolithic) anthropogenic influence. The first two types are natural grasslands that show a Holocene continuity and are not only stable due to human influence.

1.3 Objectives and Hypotheses

This thesis is embedded in a project of the Czech Academy of Sciences and the scientific institution VUKOZ in Brno, Czech Republic. The main objective of the project is to reconstruct the Holocene environmental history of very species-rich forest-steppe ecosystems in the Czech Republic, Ukraine and Romania. The focus is based on the continuity of this vegetation type,

which hypothetically existed during the Holocene despite the suitability of the environment for closed forest vegetation and the strong human impact over several millennia. The issue of continuity will be addressed in an interdisciplinary approach. A palaeoecological team will study charcoal from forest fire remains and phytoliths from different soil horizons to reconstruct the vegetation of the past. A second part of the work will focus on the existing vegetation today within the studied grasslands and interpret these results in a broader biogeographical context. A third team will focus on soil formation and soil memory. The aim here is to reconstruct the different processes during soil genesis in order to get an impression of earlier environmental conditions. This thesis is part of the sub-project *soil memory*, which aims to test the continuity of vegetation based on soil properties and characteristics. For this purpose, the age of the individual soils will be determined using a meteoric ^{10}Be analysis, which may help to draw conclusions about the timing of different processes of soil formation. As disturbances could be a possible reason for a Holocene continuity of the forest-steppe ecosystem, a long-term soil erosion rate could help to indicate these disturbances. For this, the meteoric ^{10}Be will be used to calculate a long-term soil erosion rate over the time of soil formation. Another method to determine the long-term soil erosion rate is the in-situ ^{10}Be exposure dating on different heights of an outcrop (Raab et al., 2018). Furthermore, soil erosion rates will be assessed using a percolation theory approach based on soil formation by Egli et al. (2018). In addition, the maximum potential age of the soils will be calculated using the in-situ ^{10}Be method (Egli et al., 2010; Raab et al., 2018). Continuity of the same vegetation type would mean that the erosion rate would remain relatively constant under assumed constant environmental conditions. With the methods using ^{10}Be already mentioned, a combination with analysis of the rather short-lived fallout isotopes ^{239}Pu and ^{240}Pu in the soil can result in information about the age of the different soil sites as well as soil transport (erosion and accumulation) and – to a certain degree – soil disturbances (Šamonil et al., 2013).

The main aim of the project, of which this thesis is part of, is testing the idea of Holocene continuity of forest-steppe ecosystems of Central Europe under different influences of changing human land-use intensity and changes in local climate. The aim of this thesis is to test these hypotheses in terms of soil erosion rates and the age of the soils, which may provide information on the timing of different processes of soil formation.

Based on previous evidence the main hypotheses are the following:

1. *The forest-steppe grasslands in Romanian Transylvania occur with Holocene continuity despite suitability of the current climate for closed forest growth (main project hypothesis).*
2. *The estimated age of the soils is quite high, as the region has not been glaciated during the last glacial maximum.*
3. *The short-term erosion rates of the different sites are larger than their long-term erosion rates, indicating that man-made disturbances as seen today are not visible over a longer period.*

Based on this aim, the following research questions can be formulated:

1. *How old are the sampled soils around the city of Cluj-Napoca in Romanian Transylvania?*
2. *Can differences in erosion rates on different time scales be detected?*
3. *Can these differences contradict the hypothesis of Holocene continuity of forest-steppe vegetation, and if so, what might have caused these differences?*

In addition, a possible Holocene continuity is also being investigated by other factors, which should help to provide a better overall picture of findings in favour of a Holocene continuity and others which would contradict such a continuity.

1.4 Study Area

This study has been conducted around the area of Cluj-Napoca, Cluj County in Romania (see map in Figure 2). This region is part of the Transylvanian Plain in North-Central Romania. The region is bordered by the Carpathian Mountains to the east, the Târnavei Tableland to the south and the Apuseni Mountains to the west (Weindorf et al., 2009), a location that affects the climate of the region (Tahas et al., 2011). Generally, the climate can be described as continental, characterised by warm summers and mostly cold winters. However, during autumn and winter, West-Atlantic influences are also present to a smaller degree (Tahas et al., 2011). The average annual precipitation for the meteorological station Cluj-Napoca (46°47' N/23°34'E, 414 m a.s.l.) is 583.4 ± 125.9 mm (Tahas et al., 2011) with a mean annual temperature of 9.0 °C (Iurian et al., 2012). Despite the name, the Transylvanian Plain is mainly characterised by chains of rolling hills with altitudes between 300 - 600 m a.s.l. with higher altitudes in the North. The soils of the region are mainly classified as Luvisols, Chernozems and Phaeozems (Weindorf et al., 2009) with different underlying Eocene and Oligocene bedrocks types such as clays, marls, sand and sandstone (Dengler et al., 2012). The landscape is characterised by a mix of land cover: fields

used for agriculture, many of these abandoned; dry, steppe-like grasslands with a likely very old age; secondary grasslands, some of these can be several hundreds of years old; and patches of mainly deciduous forest scattered over the landscape (Dengler et al., 2012). The main tree species are different oak species (*Quercus robur*, *Quercus petrae*), maple (*Acer tataricum*), beech (*Fagus sylvatica*) and hornbeam (*Carpinus betulus*), which occur in different proportions (Dengler et al., 2012). The grassland shows an incredibly large diversity of different plant species (Hájek et al., 2020), on a scale of 0.1 m² and 10 m² even the world's highest density of different plant species was discovered at a site North of the city of Cluj-Napoca (Wilson et al., 2012), a diversity that even surpasses that of a tropical rainforest (see Figures 1a and 1b).



Figure 1: Dry Grasslands North of the city of Cluj-Napoca with a very high plant diversity, with the highest known number of individual species on a scale of 0.1 m² and 10m².

1.4.1 Sampling Sites

The sampling sites were all located around the city of Cluj-Napoca. All sites were selected on the basis of their vegetation cover and initially sampled with a core sampler to obtain a relatively uniform picture of the soil types with uniform parent material. The sample sites were all located on different slopes dominated by erosion processes. The reference site was located on a flat area without visible erosion. The outcrops were selected based on the granitic bedrock needed for the in-situ ¹⁰Be analysis, as this analysis needs a sufficient amount of quartz which is mainly found in granitic rock. The individual locations are visible in Table 1 and on the map in Figure 2.

Table 1: Location and use of the sample and reference sites around Cluj-Napoca

Site	Use	Latitude	Longitude
CJ-1	Soil profile 1; meteoric ^{10}Be , $^{239+240}\text{Pu}$	46°50' 22.56" N	23°39' 22.68" E
CJ-2	Soil profile 2; meteoric ^{10}Be , $^{239+240}\text{Pu}$	46°49' 33.89" N	23°39' 37.06" E
CJ-3	Soil profile 3; meteoric ^{10}Be , $^{239+240}\text{Pu}$	46°39' 38.70" N	23°50' 28.10" E
CJ-4	Soil profile 4; meteoric ^{10}Be , $^{239+240}\text{Pu}$	46°38' 51.00" N	23°27' 47.09" E
CJ-C	$^{239+240}\text{Pu}$ Reference Site	46°33' 52.81" N	23°32' 50.89" E
CJ-Be1	Outcrop in-situ ^{10}Be	46°31' 59.48" N	23°34' 27.01" E
CJ-Be2	Outcrop in-situ ^{10}Be	46°32' 0.10" N	23°34' 26.40" E

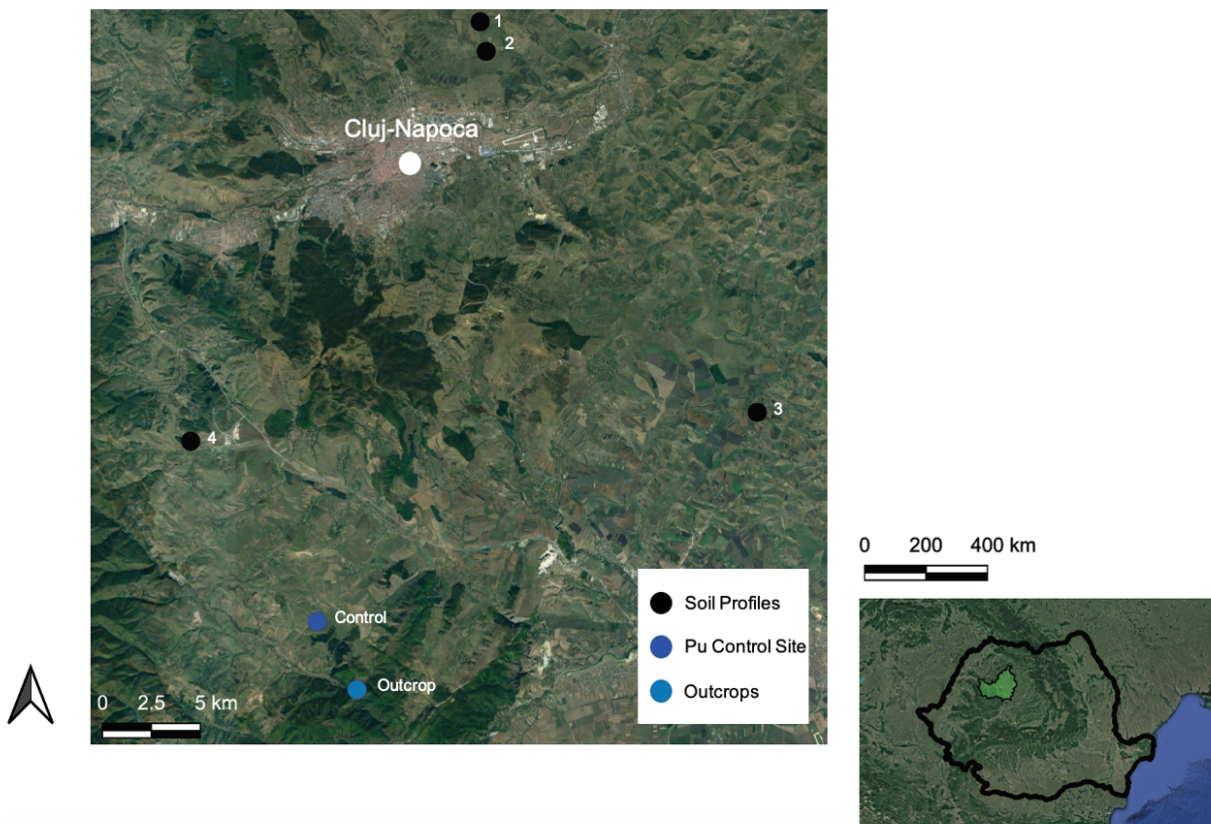


Figure 2: Location of the four soil profiles 1 - 4, the outcrop sites and the control/reference site around the city of Cluj-Napoca, Romania. The inset-map shows the location of Cluj County within Romania.

2 Methods

2.1 Terrestrial Cosmogenic Nuclides

Earth is constantly bombarded by a flux of cosmic rays, which are charged particles with high energy content, mostly atomic nuclei, but also electrons, positrons and other particles (Dunai,

2010; Dunai and Lifton, 2014). These cosmic particles sourcing from outside the solar system are mostly created by supernova explosions. These so-called primary cosmic rays interact with the atoms in the air (mainly nitrogen, oxygen and others) when they collide with the Earth's atmosphere. These collisions produce cascades of secondary particles, mostly neutrons and to a smaller degree muons, positrons, pions and electrons, which hit the Earth's surface with a high energy density. These high-energy particles can collide with atomic nuclei and thus induce spallation reactions, in which parts of the neutrons and protons of the nucleus are knocked off, resulting in lighter residual nuclei (Gosse and Phillips, 2001). This nuclide production within the atmospheric gases results in so called "atmospheric" nuclides. Additionally to this, cosmogenic particles reaching the Earth's surface can also induce the production of nuclides ("in-situ") within the lithosphere (Dunai and Lifton, 2014). The rate of in-situ production is generally lower than the meteoric production rate, as the different interactions within the atmosphere lead to an attenuation of the intensity with increasing atmospheric depth (Dunai, 2010). Furthermore, the charged particles are influenced by Earth's magnetic field. The intensity of this effect varies with latitude. At low latitudes, the parallel to the surface lying electromagnetic field lines repel a larger amount of the incoming cosmic rays, whereas at higher latitudes, more of these particles can reach the surface aligning with field lines perpendicular to the surface (i.e. in polar regions) (Dunai, 2010). The flux of the cosmic rays reaching the Earth's atmosphere are considered to be constant over the last 10 Ma (Dunai, 2010). However, the intensity of solar activity and also the strength of Earth's magnetic field vary, which leads to potential influences on the production rate of the cosmogenic nuclides. Especially at lower latitudes this effect has to be taken into consideration when calculating past nuclide production (Dunai and Lifton, 2014). Atmospheric pressure and composition did also change over this time-span, additionally influencing the production rate of the nuclides.

2.2 Surface Exposure Dating

Cosmogenic nuclides produced in-situ can accumulate over the time of being exposed to cosmic rays within the exposed surface rocks. (Dunai, 2010). A timing of land-forming processes is thus possible measuring the amount of cosmogenic nuclides in rocks and in comparison with an estimated production rate over time for the individual cosmogenic nuclide. The cosmogenic nuclides most widely used are ^3He , ^{10}Be , ^{14}C , ^{21}Ne , ^{26}Al and ^{36}Cl (Gosse and Phillips, 2001). The different half-times of the individual nuclides enables dating on different time-spans and in almost all lithologies. As all these nuclides are produced in quartz, a mineral which is highly weathering resistant and occurs in strong abundance, it accumulates over time. The measure-

ment of the concentration enables a direct dating of rock surfaces (Ivy-Ochs and Kober, 2008). Of the before mentioned, beryllium is mainly used for surface exposure dating due to its long half-life of 1.387 Ma (Chmeleff et al., 2010) which allows a dating range of 4 – 5 Ma of exposition under ideal conditions (Raab, 2019).

2.3 Exposure Dating and Long-time erosion rate: Tor exhumation process and in-situ ^{10}Be

Tors are described as residual rocks that are still rooted in the bedrock (Raab et al., 2019). Often these granitic rock formations are less susceptible to erosion processes than the surrounding soil or saprolite material. If the surrounding material is eroded, larger and larger parts of this formation have direct contact with the atmosphere, which starts an accumulation of cosmogenic in-situ nuclides. The uppermost parts of a formation are in principle the oldest, and thus have the highest content of nuclides. By measuring the content of e.g. ^{10}Be at different heights of the tors, a rate of soil erosion since the beginning of the exposure of the tors can thus be calculated (Raab, 2019). This approach works not only for tors, but also for boulders and scarps, which are gradually exposed by the same processes (Raab et al., 2018).

2.3.1 Sample Preparation for in-situ ^{10}Be Analysis

With two sites and three samples each, a total of six samples were prepared for analysis and in-situ ^{10}Be measurement. In addition, the same preparation steps were carried out with a blank sample as a control. The chemical quartz isolation was conducted using the method by Kohl and Nishiizumi (1992). After initial air-drying, the samples were further dried in an oven at 70°C for 72 hours. The rock sample material was crushed and sieved to a target fraction 0.25 – 0.6 mm. The material was leached overnight with aqua regia (65% HNO_3 : 32% HCl = 1:3, p.a.) to remove organic material and possible carbonates. After washing the leached samples, it was dried again in a drying oven. Each sample was slightly leached with 0.4% HF for 1 hour and feldspar was removed by flotation with dodecylamin. To obtain pure quartz, the samples were leached with a 4% HF solution for 1 week. This leaching was repeated 2-3 times to obtain pure quartz. To the dried leached samples, 0.35ml of a ^9Be carrier ($\text{Be}(\text{NO}_3)_2$) was added, followed by leaching with 40% HF at 100°C until the samples were completely dry to decompose the quartz. After addition of H_2O and a gentle heating of 1 hour to 80°C, the aliquot was centrifuged and the supernate was mixed with 32% HCl and homogenized for 1 hour. Fe was removed with an anion exchange column (with Biorad 1-X8 100-200 mesh) using 6 M HCl . To then separate Al and Be within the supernatant of the previous step, cation exchange columns

(with Biorad AG50W-X8 200-400 mesh) were used. The samples in the columns were firstly treated with 0.4 M oxalic acid to remove Al, Be was then eluted using 1 M HNO₃. Be(OH)₂ was precipitated with supra pure NH₄OH, the centrifuged precipitate placed in quartz crucibles and dried at 70°C over night. The crucibles were then heated for 4 - 5 hours at 120°C and then calcinated at 850°C for 2 hours. The BeO was mixed with Nb and pressed into an AMS sample holder for measurement.

The samples were measured at the ETH Zurich Laboratory of Ion Beam Physics AMS facility using the in-house ¹⁰Be standard S2007N with ¹⁰Be/⁹Be = 28.1 × 10⁻¹² as a nominal value (Christl et al., 2013). The measured ratios of ¹⁰Be/⁹Be have been corrected for ¹⁰Be by using the added Be carrier in the blank sample.

2.3.2 Age modelling using exposure in-situ ¹⁰Be

In order to calculate the exposure age of the sampled sites, the cosmogenic nuclide online calculator v3.0, the newest version of the calculator described in Balco et al. (2008), was used. In the program, a ¹⁰Be half-life of 1.387 ± 0.0012 Ma (Chmeleff et al., 2010) is used in combination with a ¹⁰Be production rate of 4.01 [¹⁰Be-atoms g SiO₂⁻¹ a⁻¹ (Borchers et al., 2016; Raab et al., 2021). Furthermore, correction factors for latitude and altitude are applied and the result is corrected for sample thickness using an effective radiation attenuation length of 160 g cm⁻² (Gosse and Phillips, 2001). Two different rock surface erosion rates were applied, assuming no erosion (0 mm ka⁻¹) or a small erosion (1 mm ka⁻¹). The actual exposure is corrected using the exposition and a shielding factor which is influenced by the surrounding topography of the sample site.

2.4 Meteoric ¹⁰Be

¹⁰Be is not only produced directly in-situ by cosmic rays, but can also be produced by nuclear interactions in the atmosphere (Lal, 2001). These nuclides are washed out of the atmosphere and fall on the Earth's surface in precipitation. Together with the water, they infiltrate into the soil, where they are enriched over time or displaced within the soil by different displacement processes (Lal, 2001). Beryllium is a particle active element, which means it gets absorbed on the surfaces and binds to soil particles (Lal, 2001; Willenbring and von Blanckenburg, 2009), especially to clay particles, the adhesion is particularly strong (Gu et al., 1997). Older soils that have been influenced by precipitation for a longer time therefore tend to have higher ¹⁰Be values. Typically, high values can be measured in the uppermost soil layers with decreasing concentration at increasing depth. A concentration maximum of ¹⁰Be can often also be found

in deeper layers, mostly in deeper clay accumulation horizons where eluviated (^{10}Be rich) clay particles are deposited (Lal, 2001). In addition, old soils generally have a higher concentration of ^{10}Be in deeper soil layers compared to younger soils because infiltration has occurred over a longer period of time (Lal, 2001). Based on these properties, an approximate age of soils can be calculated (Lal, 2001; Maejima et al., 2005).

Comparing the measured total amount of ^{10}Be in a soil with the expected amount of deposited ^{10}Be , mean erosion values over a long period of time can be calculated from the difference (Lal, 2001; Zollinger et al., 2017).

2.4.1 Sample Preparation for meteoric ^{10}Be Analysis

The sample preparation for the meteoric ^{10}Be analysis was conducted using the separation scheme by von Blanckenburg et al. (1996) as described in von Blanckenburg (2004). The sample preparation took place in the Geochronology Lab at Department of Geography, University of Zurich. 26 samples were analysed in two batches with two additional standard samples (FLUKA 41856) for control. After air-drying, the samples were further dried for 72 hours at 70°C in a drying oven. The material was milled $<2\text{mm}$ and milled and homogenized for 5 min using a horizontal mixer mill (Retsch MM400, Germany). Around 2 g of the sample material was dry-ashed in a muffle oven at 550°C for 3 hours. The amount of loss on ignition was measured. After addition of 1.0 ml of $^9\text{Be}(\text{NO}_3)_2$ standard solution (carrier), beryllium and other metals were extracted from the samples by two times overnight leaching with 16% HCl. The aliquot was adjusted to $\text{pH} = 2$ by adding 16% NaOH solution. EDTA solution was added to create metal complexes for a selective removal of the target metals. After centrifugation, the hydroxide gel was washed with NaOH to re-dissolve the metal hydroxides. The process was repeated to further remove all metals besides Be and Al and these metal were precipitated using 15% NH_4OH . After dissolving the gel in 0.4 M oxalic acid, the solution was filtered through columns with AG50-X8 200-400 mesh, and Be and Al and other metals were separated with different elution processes. For this, the column was rinsed with HNO_3 with increasing molarities (0.5 M, 1 M, 1.2 M). The solution was precipitated by adjusting pH to 5-8.7 by adding 25% NH_4OH . The samples were put into quartz crucibles then dried at 120°C . In a last step, the $\text{Be}(\text{OH})_2$ was calcinated at 200°C for 2 hours and subsequently at 850°C for 1 hour, resulting in pure BeO, which was mixed with Nb powder and transferred to targets for measurement.

The samples were measured at the ETH Zurich Laboratory of Ion Beam Physics AMS facility using the in-house ^{10}Be standard S2007N with $^{10}\text{Be}/^9\text{Be} = 28.1 \times 10^{-12}$ as a nominal value (Christl et al., 2013).

2.4.2 Soil Age Modelling using Meteoric ^{10}Be

Since the total inventory of ^{10}Be in a soil increases with age, a minimum age can be calculated with a known annual deposition rate of ^{10}Be . Maejima et al. (2005) calculate the age using the following equation:

$$t = -\frac{1}{\lambda} \ln\left(1 - \lambda \frac{N}{q}\right) \quad (1)$$

with $t =$ age, $\lambda =$ decay constant of ^{10}Be which is $4.62 \times 10^{-7} \text{ year}^{-1}$, $N =$ measured total ^{10}Be (atoms cm^{-2}) and $q =$ average annual deposition rate of ^{10}Be (atoms $\text{cm}^{-2} \text{ year}^{-1}$). The inventory of ^{10}Be N was calculated using the following equation by Egli et al. (2010):

$$N = \sum_{a=1}^n (z_w \rho_w C_w f_w) \quad (2)$$

where z_w is the thickness of an individual soil horizon, ρ_w is the bulk density of the corresponding horizon, C_w is the concentration (fine earth) in the soil horizon and f_w the relative fraction of the fine earth (in %) by weight (Egli et al., 2010).

This age calculation only results in a minimum age, as a proportion of the ^{10}Be has been removed by erosion. This leads to an underestimation of the soil age.

To determine the age of the soils, the annual average deposition rate q must be determined. For large parts, the deposition rate of ^{10}Be is not known (Egli et al., 2010), therefore an estimation has to be made to calculate soil ages. There are different approaches for this estimation. Maejima et al. (2005) use precipitation as a main proxy for ^{10}Be deposition. Willenbring and von Blanckenburg (2009) show a dependence of the distribution of ^{10}Be with the geometry of the Earth's magnetic field, which allows a determination of the latitudinal variation. The flux of ^{10}Be increases towards the poles, which in combination with the increasing thickness of the atmosphere at low latitudes and low pressures at the poles results in a maximum at mid-latitudes (Willenbring and von Blanckenburg, 2009; Egli et al., 2010).

Graly et al. (2011) have an approach that combines both methods to some extent. For low and middle latitude they have developed a formula that includes the amount of precipitation, the geographical position (latitude) and a correction for different solar activity. In addition, so-called recycled ^{10}Be , which mainly comes to the surface as dust, is included here. The resulting formula is the following (Graly et al., 2011):

$$^{10}\text{Be}_{flux} = P \times (1.44 / (1 + \text{EXP}((30.7 - L) / 4.36)) + 0.63) \quad (3)$$

with P = precipitation and L = latitude of the area of interest. This formula was also used in this study to calculate minimum ages of the soils. Additionally, the ages were also calculated using a value for q of 1×10^6 according to Willenbring and von Blanckenburg (2009) for comparison.

2.4.3 Long- and Mid-term Soil Erosion Rates using Meteoric ^{10}Be

Meteoric ^{10}Be can also be used to estimate long-term soil erosion rates. To be able to make a quantification of the soil erosion rates, Lal (2001) has developed a two-layer model. This model considers the distribution of ^{10}Be in different soil depths by comparing topsoil (O, A and E horizons) ^{10}Be content with subsoil (B and C horizons) ^{10}Be content. From this model, it is possible to conduct soil erosion rate calculations using the following equation:

$$K_E = \frac{N_D}{N_S} \left[\frac{q + q_a}{N_D} - \lambda \right] - \lambda \quad (4)$$

where N_D is the ^{10}Be inventory in the D layer, N_S the ^{10}Be inventory in the S layer, q the ^{10}Be flux from the atmosphere, q_a the flux of aeolian ^{10}Be (in this case ≈ 0) and λ the decay constant of ^{10}Be (Lal, 2001). The second model for calculating erosion rates is that of Zollinger et al. (2017) The method calculates the erosion rate by comparing the expected amount of ^{10}Be of a soil with a known surface age with the actual measured amount of ^{10}Be within the profile. The difference is then considered as erosion. The soil erosion E_{soil} is calculated based on the following formula:

$$E_{soil} = \frac{1}{\rho f C_{10Be}} \left(\frac{\lambda N}{e^{-\lambda t} - 1} + q \right) \quad (5)$$

with C_{10Be} as the average content of ^{10}Be atoms in the top eroding soil horizon, f as the fine earth fraction of the soil and ρ as the soil bulk density. The flux of aeolian ^{10}Be is also considered ≈ 0 and is thus not incorporated in the formula.

2.5 Fallout Radionuclides

Large numbers of thermonuclear weapon tests in the 1950s and 1960s, accidents in nuclear power plants (e.g. Chernobyl, Fukushima) and other releases of radioactive material in the environment resulted in the distribution of anthropogenic fallout radionuclides (i.e. $^{239+240}\text{Pu}$ and ^{137}Cs) on a global scale (Alewell et al., 2014, 2017). Due to diffusion of this material through

the atmosphere and the deposition on the surface, these fallout radionuclides (FRN) can be found anywhere. This ubiquity of distribution facilitates the use of FRN as a tracer in a large number of environmental studies of different kinds (Alewell et al., 2017). After deposition on the ground, the FRN bind strongly to the soil particles of surface soil and are thus transported through the landscape by soil redistribution processes. Thus, these FRN are an effective tracer for different soil redistribution processes (Arata et al., 2016b)

2.5.1 Sample Preparation for $^{239+240}\text{Pu}$ Analysis

The sample preparation for the $^{239+240}\text{Pu}$ measurements were conducted in the Geochronology Lab at Department of Geography, University of Zurich using an adapted laboratory protocol by Ketterer (2015). 93 different samples were analysed in three batches. In addition, the analysis was equally conducted for 12 duplicates, eight standard samples (IAEA-447), eight negative controls (rock material, NIST) and eight blank samples. The samples were initially air-dried and then further dried for 72 hours at 70°C in a drying oven. Sample material was sieved <2mm and then milled and homogenized for 5 min using a horizontal mixer mill (Retsch MM400, Germany). The samples were dry-ashed in a muffle oven for 6 hours at 450°C to remove organic matter. The aliquot was leached with 65% HNO_3 and a spike of 30pg (ca. 0.0044 Bq) of ^{242}Pu tracer solution (NIST 4334) was added. After heating the aliquot for 16 hours at 80 °C, the Pu was adjusted to a Pu^{4+} oxidation state by firstly using an acidified $\text{FeSO}_4 \cdot 7\text{H}_2\text{O}$ and afterwards an aqueous solution of sodium nitrite (NaNO_2). The aliquot was heated again to a temperature of 75°C and after cooling down, 50 mg of TEVA resin was added to the solution. The resin was rinsed using HCl (to remove thorium) and HNO_3 (to remove unretained matrix elements, e.g. uranium) and the Pu was then eluted using 0.05 M aqueous ammonium oxalate ($(\text{NH}_4)_2\text{C}_2\text{O}_4$). The Pu isotope measurement was conducted using a Triple QQQ-ICP-MS at the Chemistry Department at University of Zurich.

2.5.2 Models for $^{239+240}\text{Pu}$ Inventories and Soil Redistribution Rate Calculations

The measured $^{239+240}\text{Pu}$ activities (Pu_{act} , Bq kg^{-1}) were firstly converted into inventories (Inv , Bq m^{-2}) using the following equation (after Arata et al. (2016a)):

$$Inv = Pu_{act} \times BD \times d \quad (6)$$

where Pu_{act} is the measured activity of $^{239+240}\text{Pu}$ (Bq kg^{-1}), BD the bulk density of the soil fine fraction <2mm and d the depth of the individual soil samples. To determine whether the different sample sites were affected by erosion or accumulation processes, the inventory

differences were calculated with:

$$\Delta I = \frac{I - I_{ref}}{I_{ref}} \times 100 \quad (7)$$

where ΔI is the inventory difference, I the average total inventory (Bq m^{-2}) of the sample site and I_{ref} the average total inventory (Bq m^{-2}) of the reference site (Meusburger et al., 2016). Negative values indicate a decrease of activity and thus an erosion process, whereas positive values indicate accumulation processes.

To calculate soil distribution and soil erosion rates, different modelling approaches have been used. These models compare FRN inventories from a sample site that has been influenced by erosion or accumulation processes with the inventories of a reference site, that has been stable during the time period of interest. The first method used in this thesis was the Profile Distribution Model (PDM) by Walling and Quine (1990) and Zhang et al. (1990):

$$A'(x) = A_{ref}(1 - e^{-x/h_0}) \quad (8)$$

where x represents the depth from the soil surface as mass between the surface and the depth (kg m^{-2}), $A'(x)$ the amount of $^{239+240}\text{Pu}$ /cumulative inventory above depth x (Bq m^{-2}) and A_{ref} the total inventory at the reference site. h_0 is a coefficient describing the shape of the profile. The greater h_0 , the deeper the FRNs are able to penetrate into the soil (Walling and He, 1999). The resulting expression describing the soil erosion rate Y ($\text{t ha}^{-1} \text{a}^{-1}$) for an eroding point with an inventory of $^{239+240}\text{Pu}$ smaller than the reference inventory A_{ref} is the following (Walling and Quine, 1990; Zhang et al., 1990):

$$Y = \frac{10}{t - t_0} \ln\left(1 - \frac{X}{100}\right) h_0 \quad (9)$$

where t represents the sampling year, t_0 the year when the FRNs were deposited (in this thesis 1963, the peak of thermonuclear weapon testing (Walling and He, 1999)) and X the percentage reduction of the total $^{239+240}\text{Pu}$ inventory (calculated as $\frac{I_{ref} - I}{I_{ref}}$).

The second model that was used to analyse soil erosion rates is the Inventory Method (IM) as specifically proposed for the use of fallout $^{239+240}\text{Pu}$ by Lal et al. (2013). The inventory of fallout Pu isotopes I in a soil column is the following:

$$I = \int_0^{z_{max}} N(z) dz \quad (10)$$

with z_{max} = depth from the surface to the bottom of the soil column and $N(z)$ (mBq cm^{-3}) = concentration of fallout Pu at depth z (cm). The loss of plutonium at the sample site, Inv_{loss}

(Bq m⁻²), is the calculated average difference of Pu inventory between the reference site and the inventory at the sample site, or expressed as following:

$$Inv_{loss} = Inv_{ref} - Inv_{sample} \quad (11)$$

The model by Lal et al. (2013) assumes an exponential function expressing the shape of the Pu depth function, described by an exponent α . According to this, soil loss can be calculated by solving the following equation:

$$Inv_{loss} = \int_0^L N(z) dz = \int_0^L LN(0)e^{-\alpha z} dz \quad (12)$$

Which, with $Inv_{ref} = N(0)/\alpha$, results in:

$$L = -\frac{1}{\alpha} \ln \left(1 - \frac{I_{loss}}{I_{ref}} \right) \quad (13)$$

The fitting of α in this study was conducted as described in Alewell et al. (2014) using a least squares exponential fit of the profile depth to activity. To cope with the fact, that erosion tends to preferably remove finer-grained material, which due to its higher surface to volume ratio tends to have a higher Pu concentration than the total, a particle size correction factor P , where $P \geq 1$, is implemented in the equation (Lal et al., 2013).

$$L = -\frac{1}{\alpha P} \left(1 - \frac{I_{loss}}{I_{ref}} \right) \quad (14)$$

Here, the P factors used were 1, 1.2 (Walling and He, 1999) and 1.5 (Lal et al., 2013).

A third method that was used in this study is Modelling Deposition and Erosion rates with RadioNuclides (MODERN) by Arata et al. (2016b). One of the main advantages of this model is the ability to accurately describe the depth distribution of FRN in the soil, independent of the soils' shape function. Furthermore, the model can be applied under different land-use conditions, e.g. for ploughed and unploughed soils. The model compares the depth profile of a reference site with the total FRN inventory of the study site. The model results in a thickness of soil loss/gain by aligning the total inventory of the study site to the depth profile of a reference site with an assumed similar evolution of the depth distribution of FRN. The FRN depth profile of the reference site is modelled as step function $g(x)$, returning the value $Inv(inc)$ (Bq m⁻²) for each increment of the soil. The total inventory of Pu, Inv , is measured for the whole depth d (cm). The model targets soil level x^* (cm) from x^* to $x^* + d$ (cm), with $Inv =$ cumulated value of the Pu inventory at the reference site (Arata et al., 2016a). x^* is therefore described by (Arata et al., 2016a):

$$\int_{x^*}^{x^*+d} g(x) dx = Inv \quad (15)$$

Additionally, layers can be added by MODERN above and below the measured layers in order to estimate erosion and deposition. The newly modelled depth profile can be described by the following equation (Arata et al., 2016b):

$$S(x) = \int_x^{x+d} g(x') dx' \quad (16)$$

MODERN solves the function S by applying the primitive function G of the distribution $g(x)$ in the following way (Arata et al., 2016b):

$$S(x) = G(x + d) - G(x) \quad (17)$$

The resulting modelled soil losses or gains are returned in cm by MODERN. For reasons of comparison, they are converted in yearly soil losses or gains Y ($\text{t ha}^{-1} \text{ a}^{-1}$) by (Arata et al., 2016b):

$$Y = 10 \times \left(\frac{x^* \cdot xm}{d \cdot (t_1 - t_0)} \right) \quad (18)$$

with xm being the mass depth (kg m^{-2}), d the total depth increment of the sample site, t_1 the sampling year (a), in this study 2020, t_0 the reference time, in this study 1963.

2.6 Long-term Soil Erosion Determination using Soil Formation Modelling

The rate of soil formation is very often limited by chemical weathering, a factor which is mainly limited by advective solute transport (Egli et al., 2018). The soil formation can therefore be seen as strongly influenced by water fluxes in the soil, an understanding deriving from the so-called percolation theory (Egli et al., 2018; 2021). The soil depth is the result of soil production, which generally increases the soil depth, and denudation (consisting of erosion and chemical leaching), which results in a decrease of soil depth (Egli and Mirabella, 2021). The water flow in the soil is mainly based on the size of pores, the pore volume and the connectivity of the flow paths, a mass fractional dimensionality which equals 1.87 under most conditions (Egli et al., 2018). The pore size is best described using the median particle size d_{50} of the soil. Over time, the soil depth x can be described using the following formula (Egli et al., 2018):

$$\frac{dx}{dt} = R - E(t) = \frac{1}{1.87} \frac{I(t)}{\phi} \left(\frac{x}{x_0} \right)^{-0.87} - E(t) \quad (19)$$

with $\frac{I(t)}{\phi}$ being the net infiltration rate over time, ϕ the pore volume, $E(t)$ the erosion rate over time and x_0 the median particle size d_{50} .

If all factors are identified and only soil erosion is unknown, the theoretical soil depth modelled using the input values can be compared with the actually measured soil depth. The corresponding difference can then be used as an approximation of the eroded soil over the period of soil

formation. By approximating the erosion rate and comparing the modelled rate with the actual measured rate, an erosion rate can be evaluated.

2.6.1 Determination of Grain Size Distribution

In order to calculate the long-time erosion, the median particle size d_{50} had to be determined. The dry samples (fine material <2mm) were first sieved to a size < 32 μm . This fraction was then further analysed using a sedigraph (SediGraph III Plus V1.02, Micromeritics, USA). The finest material that was distinguishable had a size < 0.009 μm . The sedigraph measures the particle size distribution using the sedimentation method by directly measuring particle mass with X-ray absorption.

2.7 Elemental Composition

To measure the content of several elements in the soil, two different methods were applied. The samples were treated with NH_4 -oxalate ($(\text{NH}_4)_2\text{C}_2\text{O}_4$) to determine the content of non-crystalline and weakly crystalline forms of aluminium, iron, silicon and manganese (McKeague et al., 1971). To determine the amount of and crystalline forms of iron and aluminium, an extraction with dithionite ($[\text{S}_2\text{O}_4]^{2-}$) was carried out additionally (Borggaard, 1988). Using atomic absorption spectroscopy, the content of the individual elements was determined.

For each sample, two duplicates were extracted and measured according to their elemental composition. The average of the two values was used to show a depth distribution of the individual element. The amount of crystalline Al and Fe oxyhydroxides was determined by subtracting the amount of non-crystalline forms of each element (oxalate extraction) from the total amount of crystalline and non-crystalline forms (dithionite extraction). This calculation was conducted for each duplicate. A negative value indicates the absence of crystalline forms, in this case, the amount was set to 0. If only one duplicate had a negative value, the average was built with the measured positive value divided by 2.

2.8 Field Sampling Strategies

2.8.1 In-situ ^{10}Be

At two outcrops, granitic material was sampled to measure cosmogenic in-situ ^{10}Be . The boulder/outcrop should have been stable during the entire exposition time. Strike and dip of each surface was measured and the shielding of all directions was measured using a Suunto Tandem clinometer. Each rock outcrop was cleaned from moss and lichen before the sampling. To calculate a denudation process from the surface, three different heights were sampled for each

outcrop (see Figure 3a). A chessboard pattern was cut into the center of the rock surface with an angle grinder (see Figure 3b). The individual stone fragments were then cut out with hammer and chisel and collected. For each sample, around 1 – 2 kg of rock material was collected for analysis.



(a) Sampling of rock material at three different heights to calculate a soil denudation rate



(b) Chessboard pattern on a rock surface cut with an angle grinder before sampling

Figure 3: Rock sampling strategy for *in situ* ^{10}Be analysis

2.8.2 Meteoric ^{10}Be

At all four sampling sites, soil material was sampled at each individually distinguishable soil horizon within the profile. To minimize random errors, material was sampled from the entire range of the profile, which allows the calculation of an average value of the individual soil horizon.

2.8.3 $^{239+240}\text{Pu}$

The soil material for the $^{239+240}\text{Pu}$ Analysis was sampled at all four profile sites, where erosion processes were visible, and at a control site on a flat surface without any visible soil transport processes visible. At each erosion/accumulation site, four to five replicate samplings were taken, and five replicates at the reference site. With a soil core sampler with a volume of 100 cm^3 , samples were taken at 5 cm depth increments from 0-5 cm, 5-10 cm, 10-15 cm and 15-20 cm. For each first replicate, an additional sample was taken at a depth of 40 cm to determine eventual soil disturbances (e.g. bioturbation) that would influence the results of the calculations. The different replicates were distributed around each soil pit to cope with small scale variabilities. In total, 93 samples have been extracted for the analysis.

3 Results

3.1 Soil Profiles

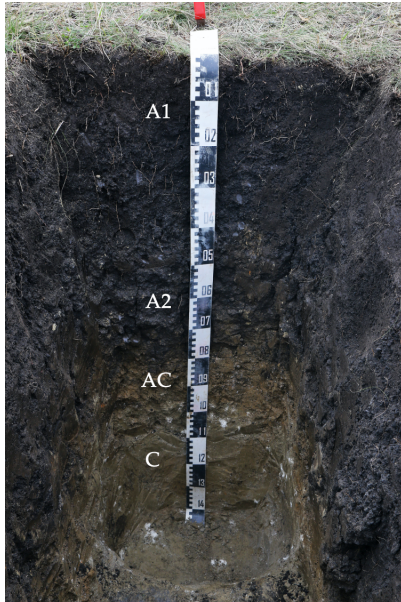


Figure 4: Soil Profile 1 CJ-1

Profile CJ-1 was located North of the City of Cluj-Napoca in an agricultural area. The altitude was 550 m a.s.l., in the midslope of a hill chain. The profile was on a North facing slope (aspect: 5 °; slope: 4°), covered with grassland. The area around the profile showed signs of erosion due to heavy livestock grassing. In addition to this, organic material was distributed into deeper depth, which also contributes to the signs of a strong soil movement. The distinguishable horizons (see Figure 4) were A1 (0 – 48 cm), A2 (48 – 80 cm), AC (80 – 98 cm) and C (98 – 140 cm). In the first 80 cm, no reaction with HCl was detectable, which is a sign for decalcification. In soil horizon AC, small fragments of secondary carbonates were found, which are very likely a precipitate of the solute carbonate material in the upper soil (Zech et al., 2014). The A horizons are mollic horizons with a rather high base saturation and a high organic content, visible by the dark colour. The dark A2 horizon showed a small amount of coatings of the organic material, which is a clear sign of clay transport within the soil. The soil was described as a Chernic Luvic Phaeozem, according to the WRB (FAO, 2014).

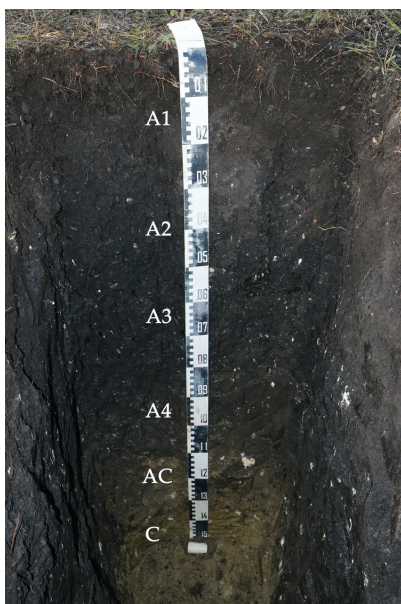


Figure 5: Soil Profile 2 CJ-2

The profile CJ-2 was also located North of Cluj-Napoca, on the opposite of the hill chain where profile 1 can also be found. The soil pit was installed on a flatter part of a South facing slope (aspect: 295°; slope: 5°) with freshly cut grassland as surface cover. The altitude of the profile was 430 m a.s.l., a bit lower than the site of profile 1. The discernible soil horizons were the following (see Figure 5): A1 (0 – 30 cm), A2 (30 – 53 cm), A3 (53 – 89 cm), A4 (89 – 114 cm), AC (114 – 140 cm) and C (140 – 150 cm). A1 showed clear signs of ploughing. A2 had a higher density compared to A1, it showed a few redox processes (coating) and few small rock particles were found within the horizon, likely from collu-

vial processes. Horizon A3 had the highest density of the A horizons. An accumulation of clay and organic matter was visible in this horizon, the structure was strongly prismatic, with no detectable carbonates. The soil horizon A4 also showed a clay accumulation and additionally some secondary carbonates in pores and channels, a first reaction with HCl was visible at a depth of 112 cm below surface. The particles in AC had no organic matter coating, however the horizon was very rich in secondary carbonates. Due to all these factors, the soil was described as a Chernic Luvic Phaeozem according to the WRB (FAO, 2014). The parent material of the soil was likely a Neogen sediment.

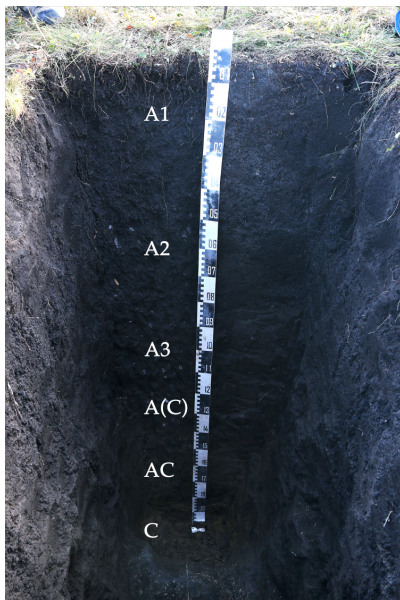


Figure 6: Soil Profile 3 CJ-3

Profile site CJ-3 was located South of Cluj-Napoca near to the village of Valea-Florilor. The site was at an altitude of 449 m a.s.l. on the flatter part of a North-East facing slope (aspect: 27°; slope: 7°). The area was covered with grassland and showed signs of very slow soil movement. The soil profile was very deep with a very deeply pronounced organic horizon, the deepest of all three Phaeozem-type soil profiles that were examined. The distinguishable soil horizons were the following (see Figure 6): A1 (0 – 39 cm), A2 (39 – 84 cm), A3 (84 – 120 cm), A(C) (120 – 145 cm), AC (145 – 184 cm) and C (184 – 195 cm). No carbonates were found for the entire depth of the soil profile of almost 2 m (no reaction with HCl), only at a depth of 222 cm, a first reaction of HCL was detectable. Some larger rock and gravel fragments in deeper soil layers are signs of colluvial processes at the site. In horizon AC, signs of large root channels were visible. The soil is a Chernic Luvic Phaeozem according to the WRB (FAO, 2014).

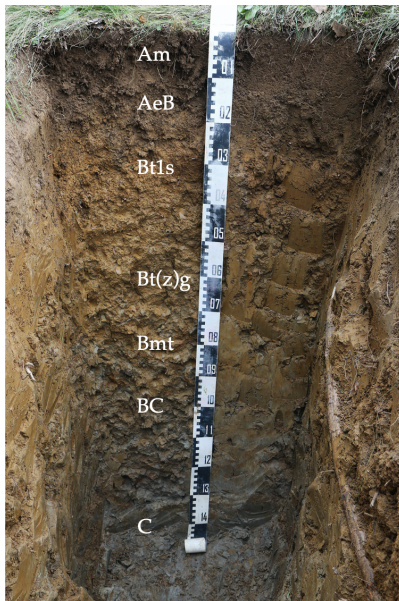


Figure 7: Soil Profile 4 CJ-4

The profile CJ-4 was located to the South-West of Cluj-Napoca near the village of Lita. The site was located at an altitude of 604 m a.s.l. just outside a small deciduous forest (mainly consisting of *Fagus sylvatica* and *Quercus robur*). The profile lied on a West facing slope (aspect: 265°; slope: 13°) on a flatter part after a rather steep slope uphill. The profile was very different in comparison to the three others, it was specified as a Stagnic Luvisol according to the WRB (FAO, 2014). The different distinguishable soil horizons were the following: Am (0 – 10 cm); AeB (10 – 23 cm) with a cylindrical structure and visible loss of clay; Bth (23 – 43 cm) with visible evidence of redox processes and an illuvial accumulation of clay and accumulation of some organic matter; Btg

(43 – 71 cm) with an increased visibility of evidence of redox processes and a stronger illuvial accumulation of clay, and visible stagnic conditions; Bmt (71 – 99 cm) with a strong cementation through the clay particles, a so called marble structure with reddish sections within peds and greyish sections along cracks and soil peds; BC (99 – 127 cm) with an increasingly grey colour; and C (127 – 147 cm) with a grey colour.

3.2 Bulk Density

For all sampled soil horizons, the dry bulk density was determined. The individual depth distributions can be found in Figure 8. In general, a trend of increasing bulk density with increasing depth is visible.

At site CJ-1, the bulk density of 1.2 g cm^{-3} decreases slightly at the surface and then increases with depth. The C horizon has the highest density of the profile with a value of slightly over 1.5 g cm^{-3} .

With 0.9 g cm^{-3} the bulk density of the horizon A1 of site CJ-2 is the lowest of all measured samples. The density also increases here with increasing depth, for both horizons A2 and A3 it is practically identical. The A4 horizon, however, has a higher density than the previous A horizons with 1.4 g cm^{-3} . The highest value is found in the AC horizon, but this is only very slightly larger than that measured in the C horizon ($1.52 \text{ g cm}^{-3} - 1.45 \text{ g cm}^{-3}$).

At site CJ-3, bulk density increases from slightly less than 1 g cm^{-3} in horizon A1 to 1.6 g cm^{-3} in the A(C) and AC horizons. The density of the C horizon is again slightly lower at 1.53 g cm^{-3} ,

as already observed at site CJ-2.

Site CJ-4 has the highest density of the surface samples at 1.2 g cm^{-3} , slightly higher than that of CJ-1. The density increases to a depth of about 80 cm, in the Bmt horizon the highest density of all samples investigated was measured at 1.69 g cm^{-3} . The density of the BC horizon is somewhat lower with only 1.32 g cm^{-3} . The density in the C horizon increases again to 1.54 g cm^{-3} . This site differs most from the other three by a large decrease in density at depth (BC horizon), which was not observed at the other three sites.

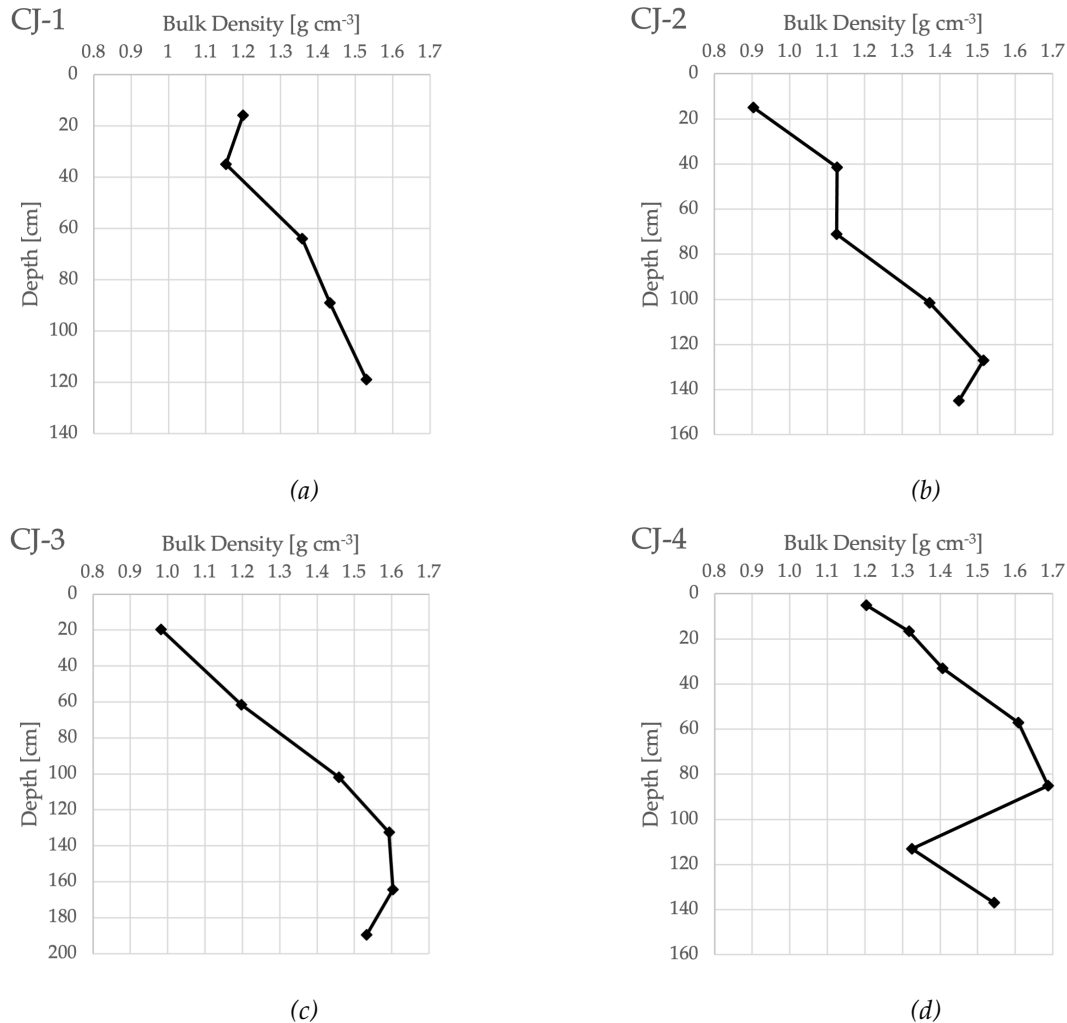


Figure 8: Bulk density of the different soil profiles with increasing depth

3.3 Elemental Composition

The distribution of the different elements can be seen in Figure 9 for the dithionite and oxalate extraction results. A depth distribution for the individual crystalline forms of Al and Fe can be found in Figure 10. The complete list of measured values can be found in the appendix in Table 12.

The total amount of Fe was larger for all samples compared to the amount of Al. For most sites, a decrease of the elemental content is visible with depth with a few exceptions.

CJ-1: At this site, the total concentration of Al decreases after horizon A2, the amount is almost identical in the uppermost horizons. With slightly more than 2.4 g kg^{-1} , the aluminium content in the uppermost layers is rather high compared to the other sites. In horizon A3 the amount decreases only slightly, only in horizon AC a decrease of almost 30% is visible compared to the horizon above. The content in the C horizon is still just over 1 g Al kg^{-1} . The situation is somewhat different for iron. Here the amount increases from initially about 15 g kg^{-1} to 21.9 g kg^{-1} in the AC horizon, which corresponds to the highest measured total content of iron in all samples investigated. The non-crystalline and weakly crystalline forms from the oxalate extractions show a slightly different distribution. The aluminium content is smaller than that from the dithionite extractions for all measurements. Only the C horizon has a slightly higher aluminium content, which means that crystalline Al oxyhydroxides are probably not present here. The aluminium content in horizon A2 is the highest measured value from the oxalate extractions with 2436 mg kg^{-1} . After an increase from the uppermost A1 horizon to the A2 horizon, the content decreases again with depth, in the C horizon it is only about half as large as in the lowest A horizon (A3). The content of amorphous Fe increases in the A horizons with increasing depth, and then abruptly amounts to barely 35% of the content in the AC and C horizons compared to horizon A3. The same pattern can be seen for manganese, the content increases within the A horizons to almost 1 g kg^{-1} (A3 horizon, highest measured manganese content), in the AC horizon the content is then only 330 mg kg^{-1} . The same applies to silicon, the amounts here are somewhat lower than for manganese. The content of crystalline aluminium oxyhydroxides decreases in the A horizons from the highest measured value of 629 mg kg^{-1} in A1 to only a good 50 mg kg^{-1} in the A3 horizon. In the AC horizon, the value rises sharply again to over 400 mg kg^{-1} , and in the C horizon almost no Al content can be measured. The content of crystalline iron oxyhydroxides increases with depth and reaches the maximum in the AC horizon, with 21.2 g kg^{-1} the highest measured value. In the C horizon the content decreases to 13.6 g kg^{-1} , the lowest value in this soil profile.

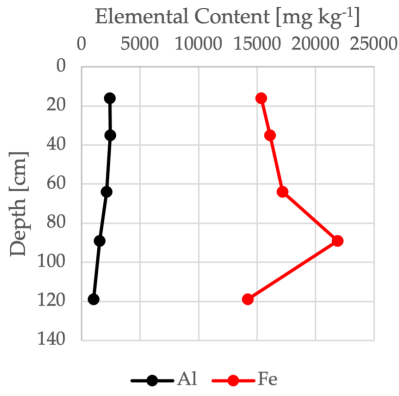
CJ-2: The total aluminium content at this site is much lower in the A horizons than at site CJ-1. From a content of just under 1 g kg^{-1} in A1, the content increases uniformly with depth to 1.4 g kg^{-1} in horizon A4. The underlying horizons AC and C show somewhat lower values of 1.2 g kg^{-1} . The total iron content is about the same in the uppermost two A horizons with slightly less than 10 g kg^{-1} , then increases with depth to almost 16 g kg^{-1} in the C horizon. The content of non-crystalline and weakly crystalline Al forms, after a small increase in the A2 horizon

compared to the A1 horizon, decreases further with depth, in the C horizon the content is only 694 mg kg⁻¹, the lowest measured content of all samples. The content of amorphous iron forms is with 5 g kg⁻¹ in the uppermost A1 horizon the highest measured of all samples. With increasing depth the content decreases and with 1.2 g kg⁻¹ in the C horizon it is only a quarter of the amount at the surface. The manganese content is slightly lower than at site CJ-1, increasing from just over 440 mg kg⁻¹ in the uppermost two horizons to 700 mg kg⁻¹. The silicon content increases to 790 mg kg⁻¹ up to horizon A3, the highest measured content, and then decreases by more than half up to the C horizon. Horizons A1 – A4 show no measurable content of crystalline Al oxyhydroxides, only at a depth of about 120 cm a relatively high content is visible, rising to the highest measured value of 513 mg kg⁻¹ in the C horizon. The crystalline Fe oxyhydroxides increase from a low value of about 7.2 g kg⁻¹ compared to site CJ-1 with increasing depth to 15.4 g kg⁻¹, the highest value of one of the measured C horizons.

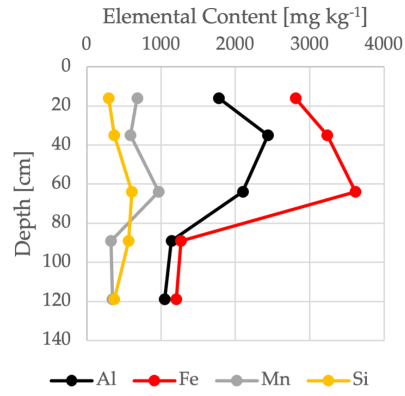
CJ-3: Site CJ-3 has the most uniform depth distribution of the measured elements. The total aluminium content in the uppermost two horizons is comparatively low at 1.2 - 1.3 g kg⁻¹ and decreases with increasing depth to the lowest measured value of 363.4 mg kg⁻¹ in the C horizon. The iron content increases from a rather deep 7.9 g kg⁻¹ in the A1 horizon to 9.5 g kg⁻¹ in the A2 horizon and then remains between 8 – 9 g kg⁻¹ in the underlying horizons. The content of non-crystalline and weakly crystalline Al forms from the oxalate extraction decreases with depth from a content of 1.8 g kg⁻¹ in the uppermost horizon to a value of 735 mg kg⁻¹ in the C horizon. The iron content from the oxalate extraction decreases from A1 to A2, the value in horizon A3 is then with 2.1 g kg⁻¹ again at the same level as the uppermost horizon. In the horizons below, the content continues to decrease. The manganese content remains at approximately the same level with depth, the silicon content continues to increase with depth from 336 mg kg⁻¹ in the A1 horizon to 453 mg kg⁻¹ in the C horizon. No crystalline Al oxyhydroxides could be measured for the entire depth of the soil profile. The crystalline Fe oxyhydroxides are on average the deepest measured with relatively small variations within the soil profile compared to the other profiles. The contents range from 6.8 g kg⁻¹ to 8.6 g kg⁻¹.

CJ-4: The total aluminium content increases from 1.7 g kg⁻¹ in the two A horizons to 2.7 g kg⁻¹ in the Bt1s horizon, which corresponds to the highest measured value. The underlying horizons have lower values of aluminium with increasing depth. The total iron contents increase from about 10 g kg⁻¹ in the Am and AeB horizons to 13.3 g kg⁻¹ in the Bt1s horizon. The two underlying B horizons show somewhat lower values around 12.5 g kg⁻¹, in the underlying BC horizon the content is only 5 g kg⁻¹, in the C horizon the lowest content was measured with 2 g kg⁻¹. The same depth profile is also visible for the amorphous iron forms, with a value of 411

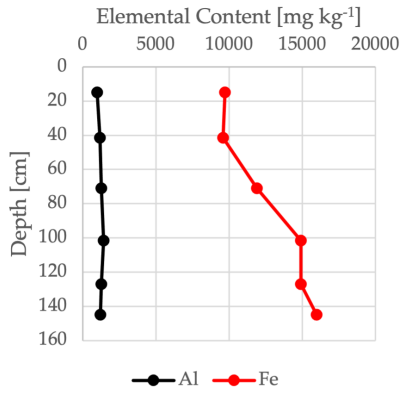
mg kg⁻¹ in the C horizon, which corresponds to the lowest measured content. The amorphous aluminium content increases from 1.7 g kg⁻¹ in the A horizons to 2.3 g kg⁻¹ in the Bt1s horizon, followed by a decrease to 1.6 g kg⁻¹ in the Btzg horizon. The manganese content drops sharply from about 480 mg kg⁻¹ in the uppermost two horizons to the lowest measured values. In the Btzg horizon only 1 mg kg⁻¹ was measured, in the deeper layers the content increases again. The silicon content increases with depth, from the lowest measured value of 204 mg kg⁻¹ in the uppermost horizons to 461 mg kg⁻¹ in the C horizon. The content of crystalline aluminium oxyhydroxides increases strongly in the B horizons compared to the A horizons to 418 mg kg⁻¹. From the Bmt horizon onwards, as well as in the horizons below, no more content can be measured. The distribution of crystalline iron oxyhydroxides is very similar, with an increase within the B horizons and low values in the underlying horizons.



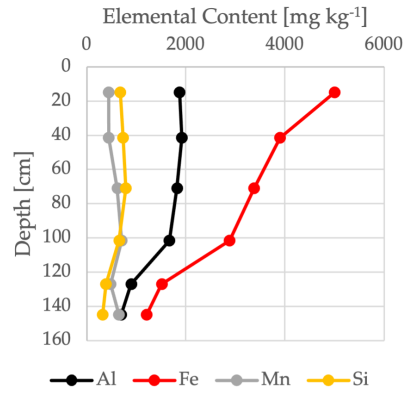
(a) CJ-1 dithionite extraction



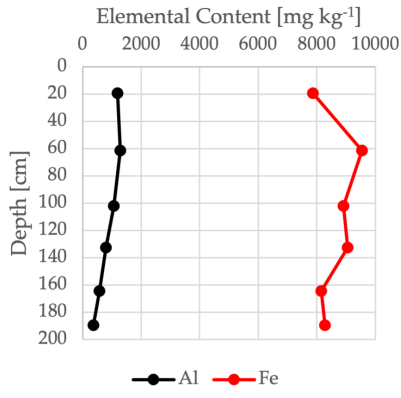
(b) CJ-1 oxalate extraction



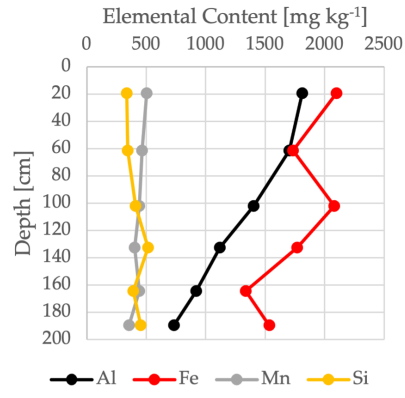
(c) CJ-2 dithionite extraction



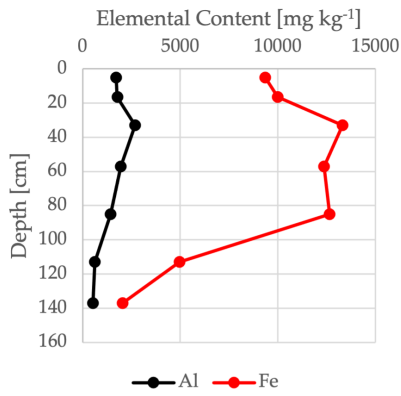
(d) CJ-2 oxalate extraction



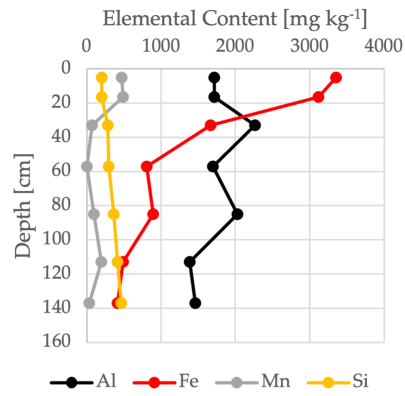
(e) CJ-3 dithionite extraction



(f) CJ-3 oxalate extraction

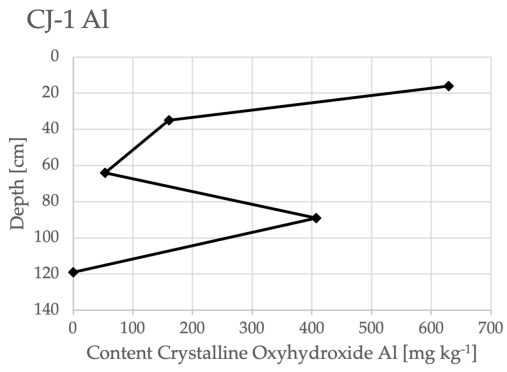


(g) CJ-4 dithionite extraction

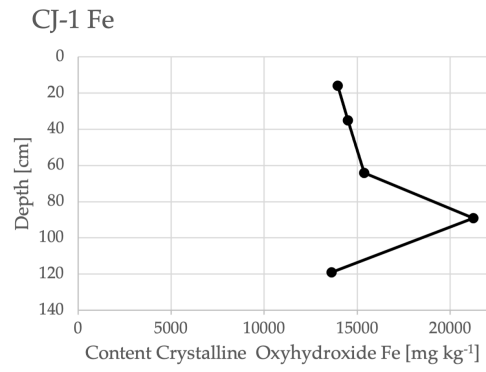


(h) CJ-4 oxalate extraction

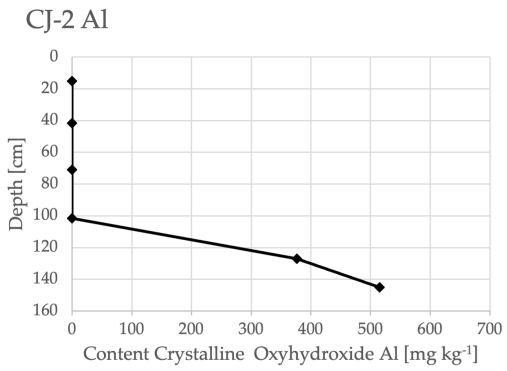
Figure 9: Elemental composition of the individual sites with depth.



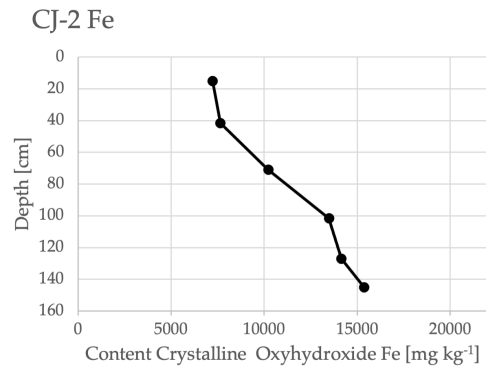
(a)



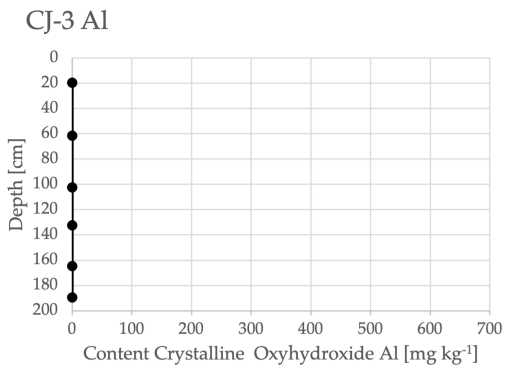
(b)



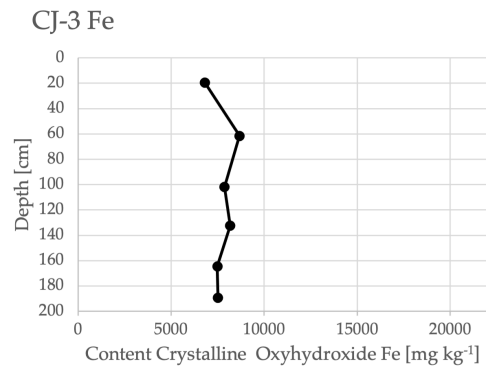
(c)



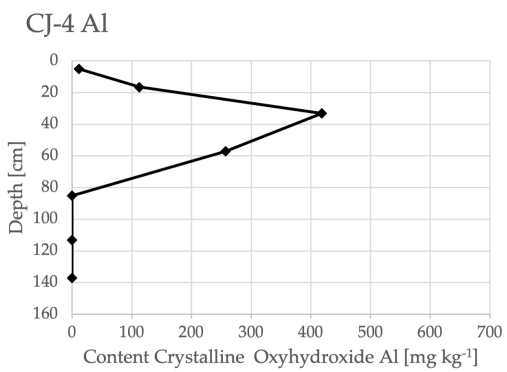
(d)



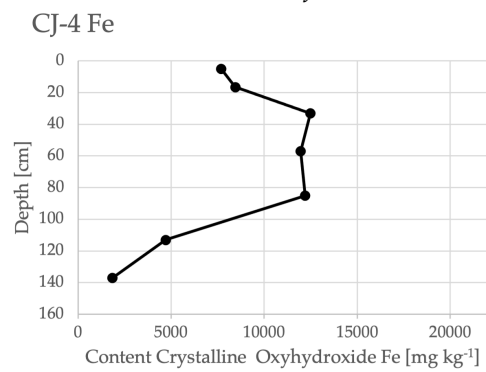
(e)



(f)



(g)



(h)

Figure 10: Content of crystalline Al and Fe forms of the different soil profile samples with depth. The amount is the difference of the amount of the dithionite-extractable element and the amount of the oxalate-extractable element forms.

3.4 ²³⁹⁺²⁴⁰Pu Activities

The measured ²³⁹⁺²⁴⁰Pu activities ranged from the detection limit up to 0.614 Bq kg⁻¹. The average over all sites was 0.240 ± 0.129 Bq kg⁻¹ (SD). The three measurements below the detection limit were all part of the control samples at a depth of 40 cm, and are therefore a good sign of no input of FRN into deeper soil horizons. For calculations, these values were not needed and thus not used. There is a decreasing trend of ²³⁹⁺²⁴⁰Pu activity for all sample sites, only in site 4, there is a slight increasing in depths of 5 – 15 cm compared to the uppermost sample, however this lies still within the standard deviation of the individual samples. Nevertheless, this result might be due to mixing by ploughing, as the soil profile showed clear signs of ploughing in the uppermost soil horizons.

All the values of the sample sites showed lower ²³⁹⁺²⁴⁰Pu activities in the upper two layers in comparison with the control layer of the corresponding depth at the control site. In layers 3 and 4, the sample layers all showed higher activities compared to the reference site, but with a higher degree of uncertainty (higher standard deviation).

The range of ²⁴⁰Pu/²³⁹Pu ratios can be used to analyse the source of the radioactive material (natural vs. FRN) (Kelley et al., 1999). The measured range of ²⁴⁰Pu/²³⁹Pu ratios reaches from 0.137 to 0.236, the average lies at 0.196 ± 0.016 (SD). These values are comparable to the ratios measured in FRN by Kelley et al. (1999) with an average ratio of 0.180 ± 0.014 and are thus very likely also sourced from nuclear weapon tests and other non-natural sources of radionuclides.

3.5 ²³⁹⁺²⁴⁰Pu Inventories

The measured ²³⁹⁺²⁴⁰Pu inventories of all samples vary between 0.634 Bq m⁻² and 36.26 Bq m⁻². The highest values were found at the reference site CJ-C (see Table 2 and Figure 11) in the uppermost layer with an average of 24.151 Bq m⁻² ± 7.14 (SD). The reference site CJ-C and sample sites CJ-3 and CJ-4 show a trend of lower layer inventories with increasing depth (see 11). This is not visible for sites CJ-1 and CJ-2, where the distribution is more or less equal throughout the entire depth of 20 cm.

For each site, the average cumulative inventory was calculated over the entire depth (see 2). The highest cumulative inventory was found at the reference site CJ-C with 61.29 Bq m⁻² ± 4.23 (SD). The sample sites all showed lower inventory values with the lowest for sample sites CJ-1 (41.83 Bq m⁻² ± 3.31 (SD)) and CJ-2 39.90 Bq m⁻² ± 5.05 (SD)). The highest value of a sample site was found at site CJ-4 with a total inventory of 55.93 Bq m⁻² ± 3.15 (SD).

The measured inventory samples were almost all normally distributed (Shapiro-Wilk-Test, confidence level 95%), only the measurements at depth interval 10 – 15 cm at site CJ-2 and at

Table 2: Measured and averaged $^{239+240}\text{Pu}$ inventories of the control site and the sample sites, including standard deviations. The average cumulative inventory shows the sum of all average values of each soil profile.

Sampling Site	Sample	Inventory $^{239+240}\text{Pu}$ [Bq m ⁻²]	Standard Deviation [Bq m ⁻²]	Average Cumulative $^{239+240}\text{Pu}$ Inventory [Bq m ⁻²]
CJ-C	C-1 (0 – 5 cm)	24.151	7.14	61.29 ±4.23
	C-2 (5 – 10 cm)	21.087	3.78	
	C-3 (10 – 15 cm)	10.190	1.81	
	C-4 (15 – 20 cm)	5.864	1.69	
	C-5 (40 cm)	0		
CJ-1	1-1 (0 – 5 cm)	10.353	1.93	41.83 ±3.31
	1-2 (5 – 10 cm)	10.725	2.69	
	1-3 (10 – 15 cm)	10.105	3.19	
	1-4 (15 – 20 cm)	10.643	4.77	
	1-5 (40 cm)	0		
CJ-2	2-1 (0 – 5 cm)	10.184	3.62	39.90 ± 5.05
	2-2 (5 – 10 cm)	10.599	4.51	
	2-3 (10 – 15 cm)	10.491	5.02	
	2-4 (15 – 20 cm)	8.627	6.57	
	2-5 (40 cm)	0.63	0.52	
CJ-3	3-1 (0 – 5 cm)	15.757	2.54	47.66 ±1.48
	3-2 (5 – 10 cm)	14.200	5.80	
	3-3 (10 – 15 cm)	11.123	7.01	
	3-4 (15 – 20 cm)	6.585	5.12	
	3-5 (40 cm)	0.75	0.51	
CJ-4	4-1 (0 – 5 cm)	20.169	5.97	55.93 ± 3.15
	4-2 (5 – 10 cm)	15.916	2.20	
	4-3 (10 – 15 cm)	13.623	2.71	
	4-4 (15 – 20 cm)	6.225	2.96	
	4-5 (40 cm)	0		

depth increment 0 – 5 cm at site CJ-4 could not be confirmed as being normally distributed. To test the significance of differences between the different groups and depths, an unpaired t-test was used for the normally distributed samples, in the two cases of not normally distributed data, a Mann-Whitney-U-test was used. The results of the comparison of sample sites and reference site can be found in Table 3 and graphically as boxplots in Figure 12.

In the uppermost depth increment (0 – 5 cm), the $^{239+240}\text{Pu}$ inventory was significantly smaller at sites CJ-1 ($p = 0.0102$) and CJ-2 ($p = 0.0085$). At sites CJ-3 and CJ-4, the difference (smaller values at sample sites) was also visible, but with a lower significance (CJ-3: $p = 0.057$ and CJ-4: $p = 0.151$).

At the second uppermost layer (5 – 10 cm), a significantly lower $^{239+240}\text{Pu}$ inventory was measured for all sample sites compared to the reference site.

In the two deepest layers (10 – 15 cm, 15 – 20 cm), there was often no strong difference of $^{239+240}\text{Pu}$ inventory visible between the reference site and the sample sites. Additionally, the

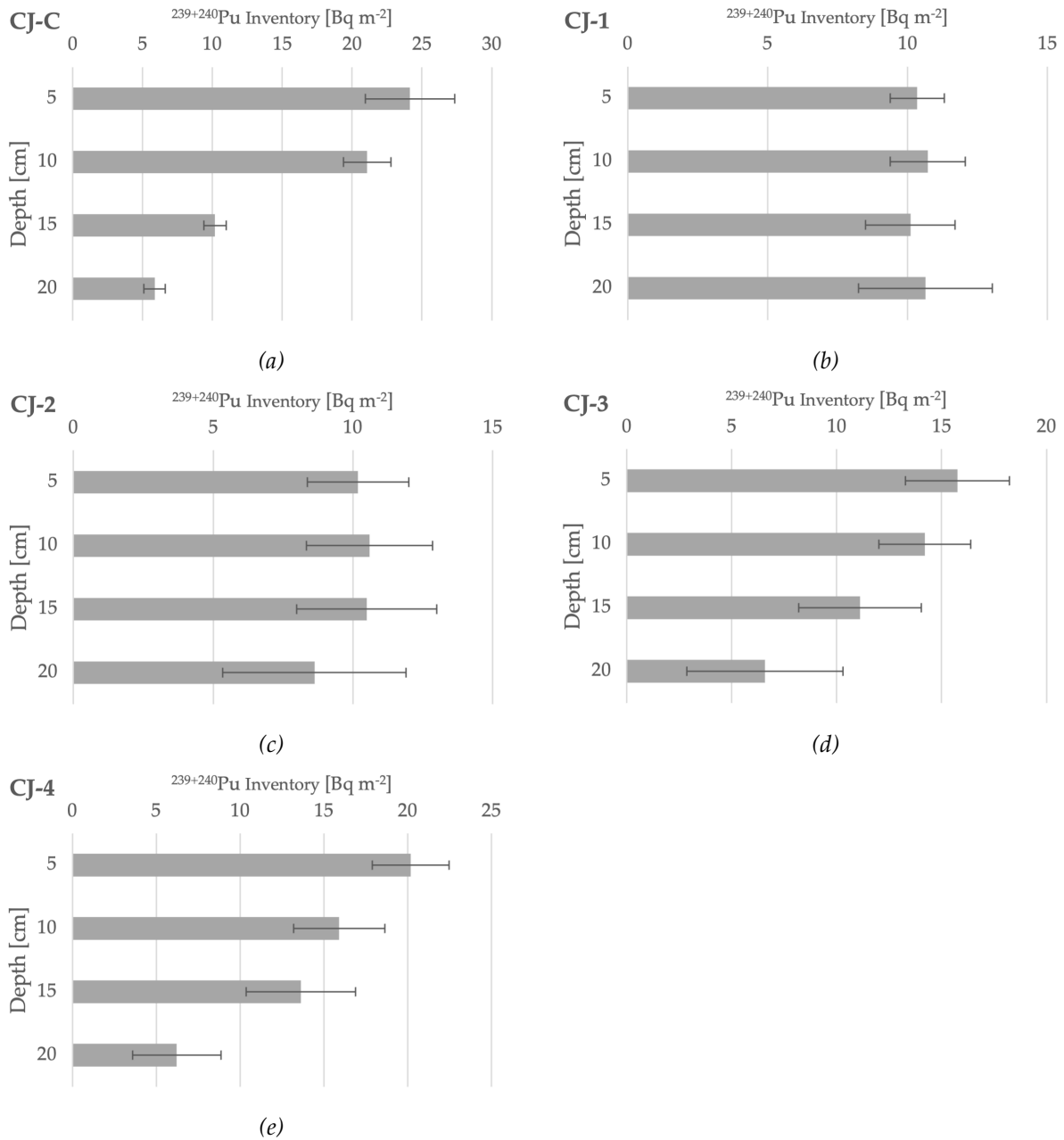


Figure 11: $^{239+240}\text{Pu}$ inventories [Bq m^{-2}] with depth [cm] for the control site (a) and all four sample sites (b, c, d, e). The value of each depth increment is the average of all individual samples of the same depth, with variation shown by the whiskers.

variability within each sample site was comparably large. As a result of this, all the differences found were not statistically significant (for individual results of each sample site - reference site comparison, see 3).

Additionally, each sub-sample of the individual sample sites and the reference site resulted in a total cumulative $^{239+240}\text{Pu}$ inventory. The different cumulative inventories of the sample sites were also compared with these from the reference site to gain an overview over the differ-

Table 3: Results of the statistical comparison of $^{239+240}\text{Pu}$ inventories at the sample sites with the inventories at the reference site on different depth increments. Data pairs with a statistically significant difference ($p \leq 0.05$) are marked with an asterisk (*).

	CJ-1	CJ-2	CJ-3	CJ-4
0 – 5 cm				
CJ-C	$p = 0.0102 *$	$p = 0.00854 *$	$p = 0.0569$	$p = 0.151$
5 – 10 cm				
CJ-C	$p = 0.00951 *$	$p = 0.0101 *$	$p = 0.0117 *$	$p = 0.0434 *$
10 – 15 cm				
CJ-C	$p = 0.964$	$p = 0.286$	$p = 0.351$	$p = 0.106$
15 – 20 cm				
CJ-C	$p = 0.137$	$p = 0.467$	$p = 0.533$	$p = 0.733$

ences. The average of all cumulative inventories was smaller for all sample sites in comparison with the reference site. However, these differences were only statistically significant ($p \leq 0.05$) for sites CJ-1 ($p = 0.043$) and CJ-2 ($p = 0.498$). For site CJ-3, the significance was slightly less strong ($p = 0.054$), but it is very likely that the smaller cumulative inventory is not entirely random. The lower cumulative $^{239+240}\text{Pu}$ inventory at site CJ-4 is statistically insignificant ($p = 0.32$).

3.6 Short-term Erosion Rates using $^{239+240}\text{Pu}$

Short-term erosion rates were calculated from the measured $^{239+240}\text{Pu}$ inventories at the different sites in comparison with the $^{239+240}\text{Pu}$ inventory of the reference site. The three different methods used to assess soil erosion (IM by Lal et al. (2013), PDM by Walling and He (1999) and MODERN by Arata et al. (2016b)) resulted in different rates over the last six decades. A summary of the resulting erosion rates can be found in Table 4 and graphically in Figure 13.

All the modelled soil erosion rates are normally distributed (Shapiro-Wilk-Test, confidence level 95 %). As all sample sites had lower $^{239+240}\text{Pu}$ inventories when compared to the inventory of the reference site, soil erosion can be assumed for all sites. This is especially important when using the MODERN model, as the application of the model varies between erosion and accumulation processes, whereas the other models use the same calculation for all soil redistribution processes.

Generally seen, the sample sites showed high erosion rates, especially sites CJ-1 and CJ-2. The highest values for erosion rates were generally calculated using the MODERN approach, only

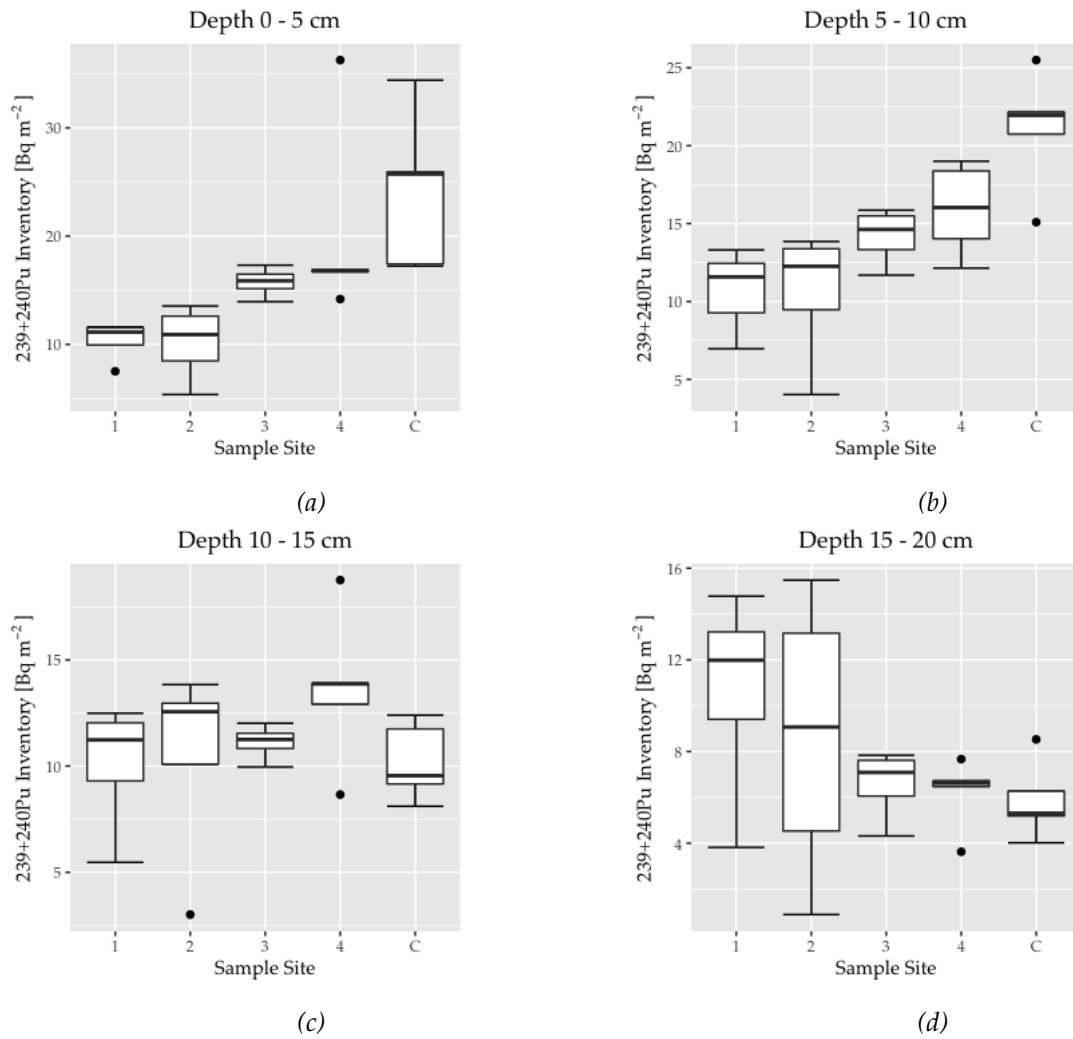


Figure 12: Boxplot of $^{239+240}\text{Pu}$ inventories of the individual sampling sites CJ-1, CJ-2, CJ-3, CJ-4 and the reference site CJ-C at four different depth increments a) 0 – 5 cm, b) 5 – 10 cm, c) 10 – 15 cm, d) 15 – 20 cm. The bold line indicates the median, the whiskers/error bars indicate the standard deviation. The dots represent outlier measurements.

at CJ-2, the PDM method resulted in a higher value. The lowest values were reached when using IM with $P = 1.5$ for all samples.

CJ-1: At site CJ-1, the average erosion rate of all modelling approaches lies at $4.4 \text{ t ha}^{-1} \text{ a}^{-1}$. The lowest value was calculated with IM ($P=1.5$) as $2.34 \pm 2.02 \text{ t ha}^{-1} \text{ a}^{-1}$, the highest value of $7.2 \text{ t ha}^{-1} \text{ a}^{-1}$ was derived from MODERN. The very high average results of CJ-1 were strongly influenced by replicate 1D, with erosion rates three to almost four times higher than the other three replicates. If the average erosion rates were calculated without this replicate, the average rate would only be around $2.7 \text{ t ha}^{-1} \text{ a}^{-1}$, with a maximum of $4.97 \text{ t ha}^{-1} \text{ a}^{-1}$ for the MODERN approach.

CJ-2: The average erosion rate at site CJ-2 is even higher than at site CJ-2 with almost 5.4 t ha^{-1}

a⁻¹ as an average of all models. The highest modelled erosion rate is as high as 7.89 t ha⁻¹ a⁻¹, however with a very high variance of ±9.27 t ha⁻¹ a⁻¹ (SD). The lowest value, calculated using IM with P= 1.5 was 3.03 t ha⁻¹ a⁻¹ ±3.74 (SD). The very high variability is again as in CJ-1 the result of one replicate, which is very different to the the other ones. Here again, it is replicate 2D with erosion rate values more than five times higher than in the other replicates. If the average erosion rates are calculated without this replicate, the resulting average lies at only 2.4 t ha⁻¹ a⁻¹, less than half than with replicate 2D.

CJ-3: The third sampling site has lower calculated erosion rates compared to the previous two. The average of all methods lies at 2.8 t ha⁻¹ a⁻¹, with the highest value of 5.19 t ha⁻¹ a⁻¹ using MODERN and the lowest rate of 1.42 ±0.33 t ha⁻¹ a⁻¹ using the PM approach with P=1.5 as a factor. The variability at this site was the smallest of all the sites studied.

CJ-4: At this sampling site, the lowest calculated erosion rates have been observed. An average erosion rate of 1.35 t ha⁻¹ a⁻¹ is only a fraction of what was calculated in the other sites. MODERN modelling resulted in the highest rates with 2.78 t ha⁻¹ a⁻¹, whereas the IM method with P=1.5 calculated an erosion rate of 0.70 ±0.55 t ha⁻¹ a⁻¹. The lowest erosion rates at this site were found in the two replicates located in the forest (4C, 4D), they were lower compared to the replicates that were located outside the forest on the grass of the cut area.

To compare the different modelling approaches, the different results of each sample were tested using a pairwise-t-test. For CJ-1, a significant difference between the modelled values were only found when comparing the IM with P = 1.2 and P = 1.5 to the results from MODERN ($p = 0.0426$; $p = 0.0170$). For CJ-2, the differences were not statistically significant, mainly due to the fact that the variance of the individual ²³⁹⁺²⁴⁰Pu inventories was very high. In the results of CJ-3, every comparing of result showed significant differences. At this site, the variance was the smallest compared to the other sample sites. CJ-4 showed significant differences when comparing IM (P = 1; 1.2; 1.5) with MODERN ($p = 0.00917$; 0.00337 ; 0.00105) and PDM with MODERN ($p = 0.0415$).

Table 4: Overview of the calculated erosion rates and their standard deviation from different modelling approaches using fallout $^{239+240}\text{Pu}$. IM = Inventory Model (Lal et al., 2013); PDM = Profile Distribution Model (Walling and Quine, 1990; Zhang et al., 1990), MODERN = Modelling Deposition and Erosion rates with RadioNuclides (Arata et al., 2016b).

	IM (Lal et al., 2013) P=1	SD	IM (Lal et al., 2013) P=1.2	SD	IM (Lal et al., 2013) P=1.5	SD	PDM (Walling and He, 1999)	SD	MODERN (Arata et al., 2016b)
Site	$\text{t ha}^{-1} \text{a}^{-1}$		$\text{t ha}^{-1} \text{a}^{-1}$		$\text{t ha}^{-1} \text{a}^{-1}$		$\text{t ha}^{-1} \text{a}^{-1}$		$\text{t ha}^{-1} \text{a}^{-1}$
CJ-1	3.5	± 3.02	2.92	± 2.52	2.34	± 2.02	6.02	± 5	7.2
CJ-2	4.55	± 5.62	3.79	± 4.68	3.03	± 3.74	7.89	± 9.27	7.53
CJ-3	2.13	± 0.49	1.77	± 0.41	0.42	± 0.33	3.59	± 0.74	5.19
CJ-4	1.05	± 0.82	0.88	± 0.68	0.70	± 0.55	0.34	± 1.09	2.78

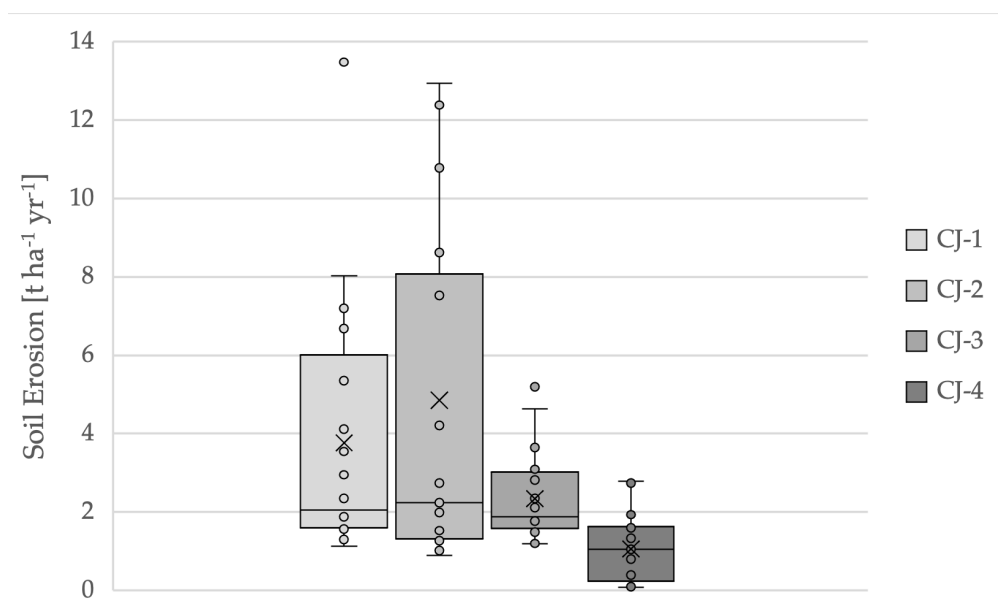
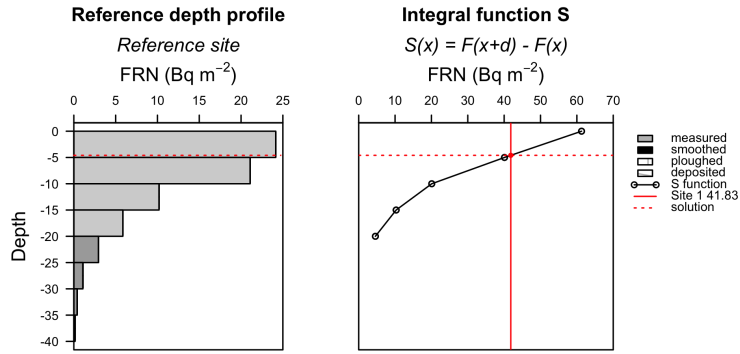
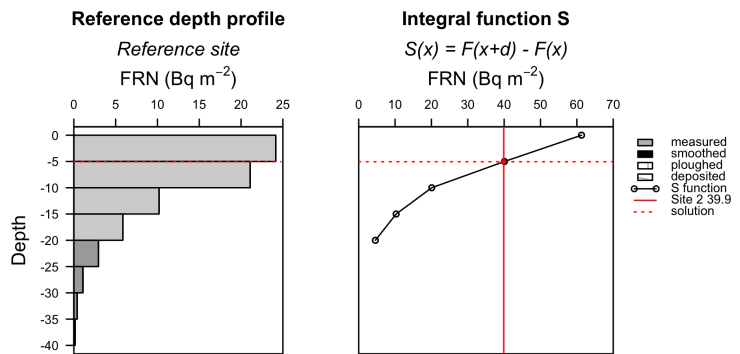


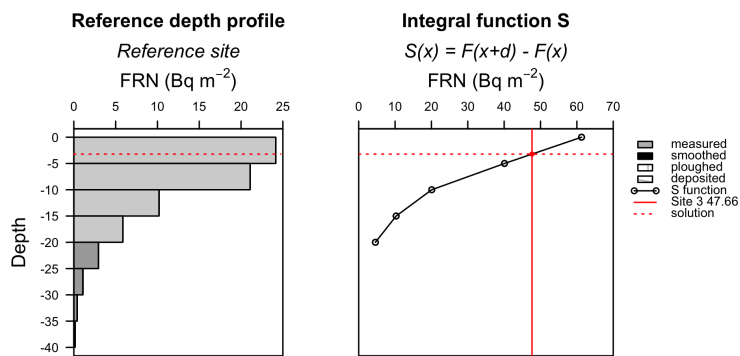
Figure 13: Boxplot of all measured erosion rates calculated with different models (IM (P=1, 1.2, 1.5), PDM, MODERN) for each sample site. The horizontal line in the box is the median, the x in the box is the mean of the measurements. For Site CJ-2, one outlier with a value of $21.8 \text{ t ha}^{-1} \text{a}^{-1}$ is not depicted.



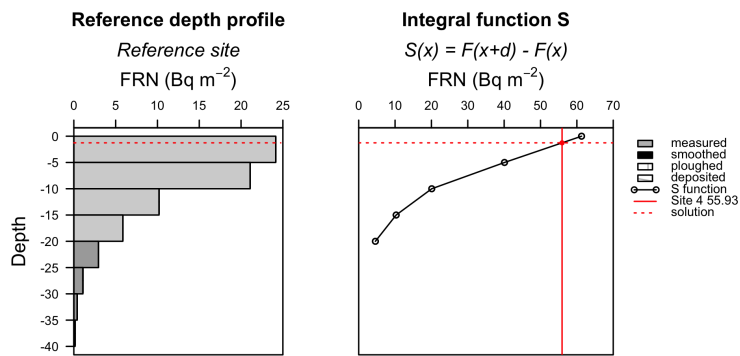
(a)



(b)



(c)



(d)

Figure 14: Reference Depth Profiles and Plotted Integral Function with solution of each sample site depicted as a vertical red line, a) CJ-1, b) CJ-2, c) CJ-3, d) CJ-4.

3.7 In-Situ ^{10}Be Inventory

Of the six rock samples tested at sites CJ-Be1 and CJ-Be2, only samples CJ-Be11, CJ-Be12 and CJ-Be13 at site CJ-Be1 yielded sufficient pure quartz from the extraction process for analysis of the amount of ^{10}Be . For the other samples, the amount of quartz was not large enough for a measurement of in-situ ^{10}Be . The amounts of ^{10}Be measured in the AMS were corrected with a long-term sample preparation blank. CJ-Be11 has the lowest amount of ^{10}Be per gram with 3.11×10^4 atoms g^{-1} . The other two samples CJ-Be12 and CJ-Be13 have very similar values of 4.17×10^4 atoms g^{-1} and 4.22×10^4 atoms g^{-1} (see Table 5. The difference between the three samples, however, is statistically not significant (ANOVA, confidence level 95%).

Table 5: Measured in-situ ^{10}Be content of the three samples of sample site CJ-Be1. The error includes the AMS standard error.

Sample	Amount of ^{10}Be ($\times 10^4$) [atoms g^{-1}]	Absolute Error ^{10}Be ($\times 10^4$) [atoms g^{-1}]	Error ^{10}Be [%]
CJ-Be11	3.11	0.18	0.06
CJ-Be12	4.17	0.31	0.07
CJ-Be13	4.22	0.27	0.06

3.8 Surface Exposure Age using In-Situ ^{10}Be

The difference between the scenario with no erosion and the one with an erosion of 1 mm ka^{-1} is not very large (see Table 6).

CJ-11, the lowermost sample at a height of 15 cm above surface has the youngest age calculated age with around 6500 years of exposure. The middle sample CJ-12 is the oldest of the samples with an age of about 7800 years. The uppermost sample CJ-13 is younger again, with an exposure time of approximately 6800 years. There is no age trend visible at this site, the differences between the ages are not statistically significant (ANOVA, confidence level 95%).

Table 6: Exposure ages of the three sample sites calculated using the cosmogenic nuclide online calculator v3.0 (see Balco et al., 2008 for v. 1.0). First results show exposure age without erosion, second results with an erosion rate of 1 mm ka^{-1} . The internal error contains the measurements uncertainties of the nuclide concentration, the external error contains measurement uncertainties and nuclide production rate uncertainties.

<i>Erosion rate = 0 mm ka⁻¹</i>			
Sample	Age [a]	Internal Error [a]	External Error [a]
CJ-11	6529	386	624
CJ-12	7772	583	825
CJ-13	6809	439	674
<i>Erosion rate = 1 mm ka⁻¹</i>			
Sample	Age [a]	Internal Error [a]	External Error [a]
CJ-11	6564	391	631
CJ-12	7821	590	836
CJ-13	6850	445	682

3.9 Long-term Erosion Rate using In-Situ ¹⁰Be

Although no real age trend could be identified for the three samples, a simple approach was used to estimate the long-term erosion rate. Since the maximum calculated exposure age is 7.8 ka, this age was used with the assumption that this age is approximately suitable for all three points. Based on this assumption, the 15 cm height of the lowest point would correspond to the height of the eroded soil material. A long-term erosion rate estimated with these two values is 19.2 mm ka^{-1} . With the average bulk density of the uppermost horizons of the four soil profiles of 1.06 g cm^{-3} , this gives an approximate erosion rate of $0.20\text{ t ha}^{-1}\text{ a}^{-1}$. If the calculated age of the lowest sample of 6.5 ka is used, the erosion rate is slightly higher with $0.24\text{ t ha}^{-1}\text{ a}^{-1}$.

3.10 Meteoric ¹⁰Be Inventory

All four soil pits show a very distinguished depth pattern concerning their meteoric ¹⁰Be content.

CJ-1 (Figure 15a): The content of ¹⁰Be decreases from around $2.78 \times 10^8\text{ atoms g}^{-1}$ in the top layer steadily to a content of $0.14 \times 10^8\text{ atoms g}^{-1}$ in the AC layer at a depth of 80–98 cm. In the

C horizon below (98–140 cm), the ^{10}Be content increases again a little to 0.26×10^8 atoms g^{-1} .

CJ-2 (Figure 15b): The content of ^{10}Be in the uppermost two soil horizons (A1: 0–30 cm; A2: 30–53 cm) is equal at about 2.4×10^8 atoms g^{-1} and then decreases relatively evenly with increasing depth. In the C horizon (140–150 cm), the ^{10}Be content is almost non-existent with 0.03×10^8 atoms g^{-1} .

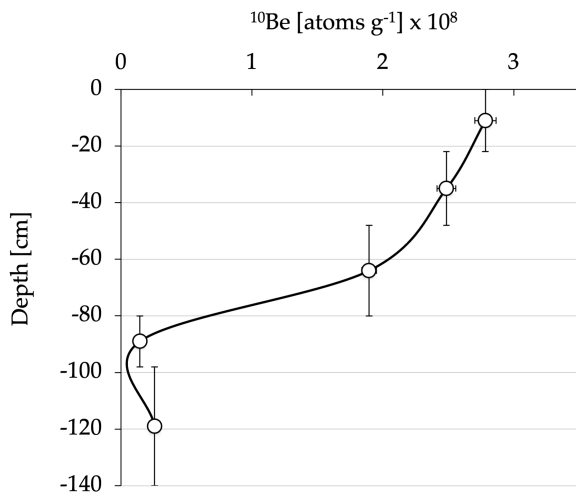
CJ-3 (Figure 15c): The ^{10}Be content of site CJ-3 decreases only very slightly in the uppermost soil horizons A1 (0–39 cm), A2 (39–84 cm) and A3 (84–120 cm) (from 2.95×10^8 atoms g^{-1} to 2.83×10^8 atoms g^{-1}). In the deeper horizons the content decreases slightly, but only moderately, so that even in the C horizon (184–195 cm) the ^{10}Be content is still 0.81×10^8 atoms g^{-1} .

CJ-4 (Figure 15d): Site CJ-4 has slightly different characteristics than the other three sites studied. The ^{10}Be content is much higher here. The content at the surface (Am horizon 0–10 cm) is 5.05×10^8 atoms g^{-1} and remains relatively constant over the two next lower horizons (AeB 10–23 cm; Bt1s 23–43 cm). In the horizon below, Btzg (43–71 cm), the content drops slightly, then rises one horizon below (Bmt 71–99 cm) above the content of the surface. In the underlying BC horizon (99–127 cm), the highest measured ^{10}Be content of the entire profile is found with 7.15×10^8 atoms g^{-1} . In the C horizon, the content drops slightly, but remains at a high 6.49×10^8 atoms g^{-1} .

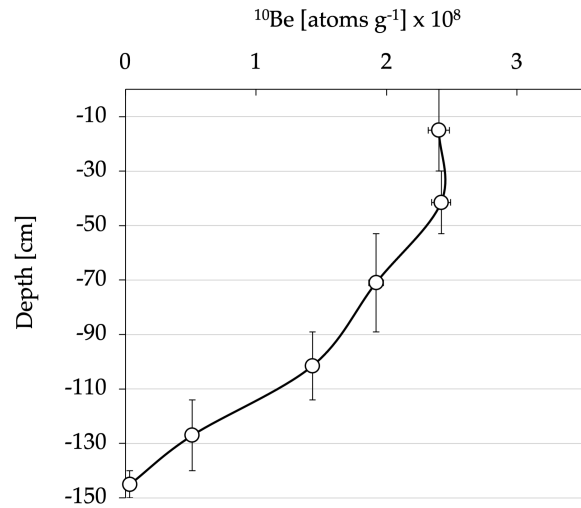
3.11 Soil Age Estimation using Meteoric ^{10}Be

The soil age estimation of the four soil profiles has been made using the formula by Maejima et al. (2005). As the results are strongly influenced by the value of the average annual precipitation rate of ^{10}Be , two different methods were used, leading to two different minimum age estimations. Willenbring and von Blanckenburg (2009) use 1×10^6 as input value for q . Graly et al. (2011) use a formula to calculate the average annual precipitation rate of ^{10}Be , the resulting value for the area of interest in this study is 1'219'040, which was used to calculate the minimum age of the soils.

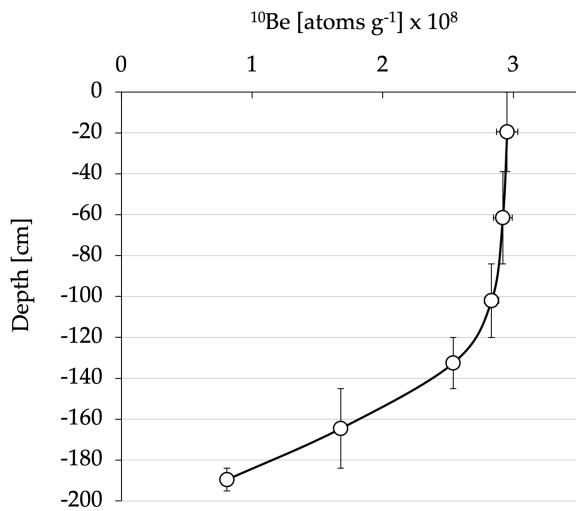
The different amounts of annually precipitated ^{10}Be lead to two different soil age estimations, an overview can be seen in Table 8. The higher input rate of ^{10}Be using Graly et al. (2011) leads to generally lower minimum ages of the soils studied. The soils at sites CJ-1 and CJ-2 were the youngest with ages around 20 - 25 ka. The soil at site CJ-3 has a calculated minimum age of around 53 - 65 ka, which is the oldest of the three Phaeozem soils studied. The oldest soils studied were found at site CJ-4 with ages over 100 ka, with an estimation of over 125 ka using the ^{10}Be precipitation rate by Willenbring and von Blanckenburg (2009).



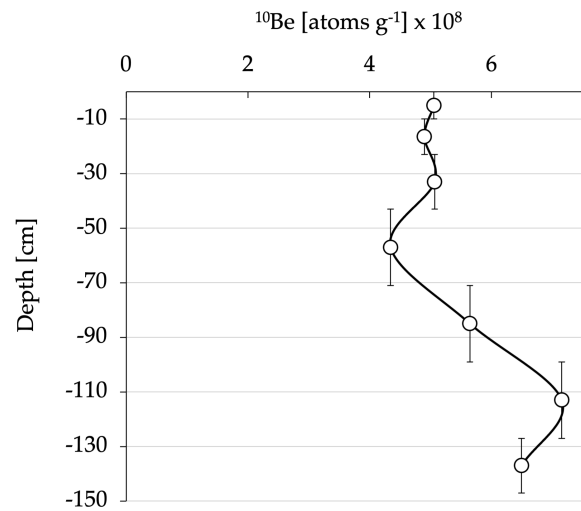
(a) CJ-1



(b) CJ-2



(c) CJ-3



(d) CJ-4

Figure 15: Concentrations of meteoric ^{10}Be as a function of depth below surface. The vertical error bars indicate the individual depth increment, the horizontal error bars the standard deviation of the content of ^{10}Be in the corresponding depth increment.

Table 7: Meteoric ^{10}Be concentrations of the individual soil horizons of each sampling site.

Site	Soil Horizon	Depth [cm]	^{10}Be atoms $\times 10^8$ [g $^{-1}$]	error [%]	Absolute error $\times 10^8$ [g $^{-1}$]
CJ-1	A1	0-22	2.78	2.9	0.08
	A2	22-48	2.49	2.92	0.07
	A3	48-80	1.90	2.92	0.06
	AC	80-98	0.14	4.24	0.01
	C	98-140	0.26	3.6	0.01
CJ-2	A1	0-30	2.40	2.92	0.07
	A2	30-53	2.42	3.33	0.08
	A3	53-89	1.92	3.06	0.06
	A4	89-114	1.43	2.98	0.04
	AC	114-140	0.51	3.73	0.02
	C	140-150	0.03	5.78	0.002
CJ-3	A1	0-39	2.95	2.93	0.09
	A2	39-84	2.92	2.97	0.09
	A3	84-120	2.83	2.92	0.08
	A(C)	120-145	2.54	2.92	0.07
	AC	145-184	1.68	3.03	0.05
	C	184-195	0.81	3.24	0.03
CJ-4	Am	0-10	5.05	2.92	0.15
	AeB	10-23	4.90	2.92	0.14
	Bt1s	23-43	5.07	2.92	0.15
	Btzc	43-71	4.34	2.92	0.13
	Bmt	71-99	5.65	2.92	0.16
	BC	99-127	7.15	2.92	0.21
	C	127-147	6.49	2.92	0.19

3.12 Long-term Soil Erosion Rates using Meteoric ^{10}Be

The meteoric ^{10}Be inventories were also used to calculate a mid- and long-term soil erosion rate. Two different models were used, a first as described by Lal (2001), the other one an approach by Zollinger et al. (2017). Both approaches use the average annual ^{10}Be precipitation rate q , and therefore the two values for q as described in the section concerning soil age estimation using meteoric ^{10}Be were used, resulting in a total of four possible erosion rates per soil site (see Table

Table 8: Estimated soil ages in ka calculated using formula 1 by Maejima et al. (2005) with two different values for the average annual precipitation rate of ^{10}Be (q).

Site	Estimated Soil Age [ka] using q by Graly et al. (2011)	Estimated Soil Age [ka] using q by Willenbring and von Blanckenburg (2009)
CJ-1	20.40	24.90
CJ-2	22.74	27.76
CJ-3	53.08	64.89
CJ-4	102.22	125.33

9).

Erosion rates calculated using q by Willenbring and von Blanckenburg (2009) were smaller for both approaches. For sites CJ-1, CJ-2 and CJ-3, the approach by Lal (2001) resulted in smaller erosion rates compared to those by Zollinger et al. (2017), in CJ-4, the rates by Zollinger et al. (2017) were slightly smaller than the ones by Lal (2001). The rates at the first three sites calculated using the method by Zollinger et al. (2017) are approximately two to three times higher than the corresponding rate calculated with the approach by Lal (2001). At site CJ-4, the difference is a lot smaller between the two methods.

The method by Zollinger et al. (2017) fetched rather high soil erosion rates over a long period of time.

Table 9: Mid- and long-term soil erosion rates calculated with two different modelling approaches. For each approach, two different values for the average annual ¹⁰Be precipitation rate *q* were used to calculate soil erosion.

Site	Lal (2001) using <i>q</i> by Graly et al. (2011)	Lal (2001) using <i>q</i> by Willenbring and von Blanckenburg (2009)	Zollinger et al. (2017) using <i>q</i> by Graly et al. (2011); Estimated Age 130 ka	Zollinger et al. (2017) using <i>q</i> by Willenbring and von Blanckenburg (2009); Estimated Age 130 ka
	Erosion rate [t ha ⁻¹ a ⁻¹]	Erosion rate [t ha ⁻¹ a ⁻¹]	Erosion rate [t ha ⁻¹ a ⁻¹]	Erosion rate [t ha ⁻¹ a ⁻¹]
CJ-1	0.29	0.24	0.79	0.62
CJ-2	0.47	0.38	1.28	1.00
CJ-3	0.17	0.14	0.74	0.53
CJ-4	0.31	0.25	0.13	0.04

3.13 Grain Size Distribution

In total, the particle size distribution of 12 samples was measured. The exact distribution can be found in Table 17 in the Appendix. The subdivision into the three subclasses sand, silt and clay was carried out according to the size classification by FAO (2014): Clay < 0.002 mm, Silt 0.002 – 0.063 mm, Sand > 0.063 mm. A list of the percentage components of the individual samples examined can be found in Figure 16 and for the individual sites as a function of depth in Figure 17.

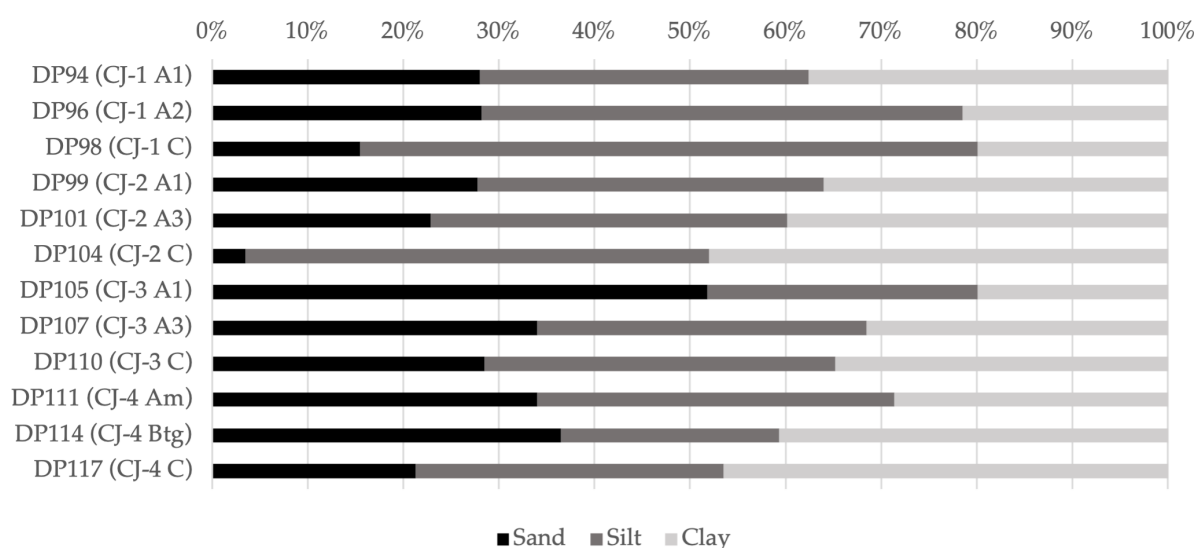


Figure 16: Soil grain size distribution of the examined samples as percentage of the total soil weight. The individual soil profile number and the corresponding soil horizons are given in brackets after the sample name.

CJ-1: The A horizons have the same proportion of sand (28%), A1 has a lower proportion of silt compared to A2 (34.4%/50.3% and correspondingly a higher proportion of clay (37.6%/21.5%). The C horizon is approximately two-thirds silt and slightly more clay than sand.

CJ-2: The two measured A horizons of this soil profile show a similar proportion distribution, the sand proportion in A1 is slightly larger than in A2 (27.8%/22.9%). The silt and clay fractions are similar, but slightly higher in A3. The C horizon has a completely different composition with almost no sand (only 3.5%). The proportion of silt is 48.5%, that of clay 48%.

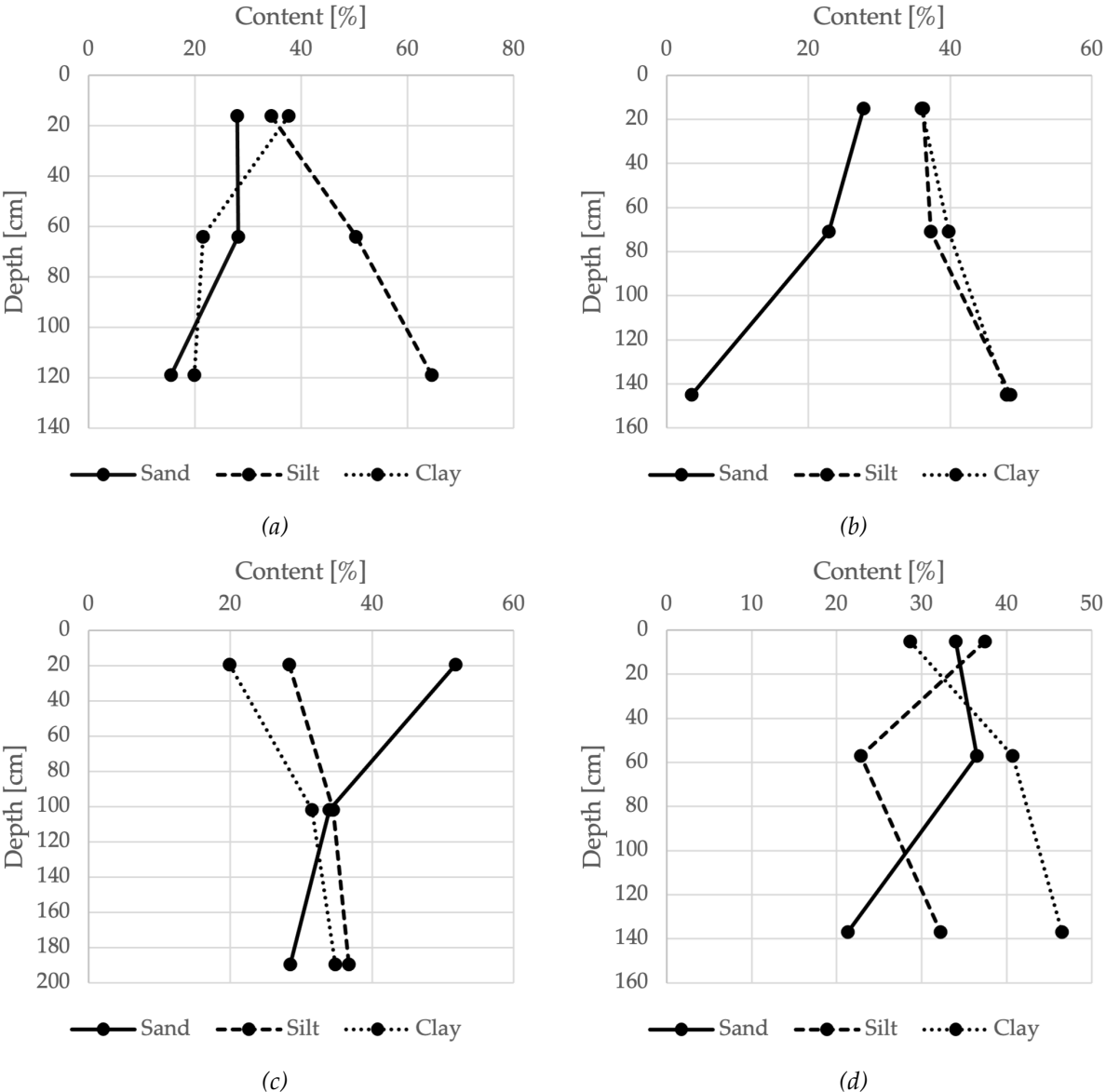


Figure 17: Proportions of the different grain size distribution with depth for the profiles a) CJ-1 (A1, A2, C), b) CJ-2 (A1, A3, C), c) CJ-3 (A1, A3, C), d) CJ-4 (Am, Btg, C)

CJ-3: The sample from horizon A1 of profile CJ-3 has the highest proportion of sand of all samples (51.8 %) and the lowest clay content of all samples (19.9 %). The sample from horizon A3 has a relatively balanced distribution with 34 % sand, 34.5 % silt and 31.5 % of clay. In horizon C, the proportion of sand is lowest at 28.3 %, and the proportion of silt is slightly higher than that of clay (36.7 %/ 34.8 %).

CJ-4: The increase in clay content with increasing depth is striking. This increases from 28.6 % in horizon Am to 40.7 in horizon Btg to 46.5 % in horizon C. In the C horizon, the proportion of sand is lowest at 21.3 %, the remaining third is silt. The proportion of sand in the uppermost horizon Am is somewhat lower than in the lower horizon Btg (34 %/ 36.5 %), but the proportion of silt is much higher (37.4) than in the Btg horizon, which has the lowest proportion of silt of all samples at 22.8 %.

3.14 Long-term Soil Erosion Determination using Soil Formation Modelling

The potential soil depth was modelled using the formula by Egli et al. (2018) and then compared with the actual measured soil depth in the field. A initial soil age of 100000 years was assumed with an infiltration rate into the soil of 200 mm a⁻¹. The resulting soil erosion rates can be found in Table 10. The largest calculated erosion rate was found for site CJ-1 with a rate of 0.30 t ha⁻¹ a⁻¹. For sites CJ-3 and CJ-4, the erosion rate is only about half the rate of CJ-1 with 0.16 ha⁻¹ a⁻¹ and 0.13 ha⁻¹ a⁻¹. The modelled soil depth for CJ-2 was smaller than the actual measured soil depth, therefore the erosion rate could not be calculated.

Table 10: input variables and the soil erosion rate calculated from the modelled theoretical soil depth. d50 is the median soil particle size calculated from the measurements of the respective soil profile.

Site	d50 [µm]	Assumed Soil Age [a]	Precipitation [mm a ⁻¹]	Evapotranspiration [mm a ⁻¹]	Infiltration Rate [mm a ⁻¹]	Porosity [-]	Erosion [t ha ⁻¹ a ⁻¹]
CJ-1	32.26	100000	600	400	200	0.5	0.30
CJ-2	7.09	100000	600	400	200	0.5	-
CJ-3	40.76	100000	600	400	200	0.5	0.16
CJ-4	24.95	100000	600	400	200	0.5	0.13

4 Discussion

4.1 Soil Profiles

The investigated soil types correspond well to the vegetation cover of the individual sites. The first three sites CJ-1, CJ-2 and CJ-3 have Chernic Luvic Phaeozemes, which are mainly found in transitional areas between wooded, wetter area and semi-arid long grass steppes (Zech et al., 2014). They occur mainly under grass vegetation with occasional sparse forest patches on loess or loess-like substrates or other fine unconsolidated sediments (Zech et al., 2014). Similar soils were also found by Paltineanu et al. (2020) for areas south of the study area. Gabor et al. (2010), Pendea et al. (2002) and Weindorf et al. (2009) examined soils distributed over the whole Transylvanian Plain, and Iurian et al. (2012) found similar soils in the Cluj-Napoca area. The deep Chernic A horizons of sites CJ-1, CJ-2 and CJ-3 are indicative of relatively stable environmental conditions over long periods of time combined with high biomass production by forest steppe, as well as high humus accumulation by burrowing soil animals (bioturbation) (Zech et al., 2014).

All three sites were identified as Luvic Phaeozems, meaning they all have an increase in clay content in deeper layers compared to the uppermost soil horizons (Zech et al., 2014). This enrichment is also visible in the enrichment of iron in the deeper A horizons, especially at sites CJ-1 and CJ-2. In addition, prismatic structures were found in the *mollic* horizons, which are more typically found in B horizons and not in A horizons (FAO, 2014). These findings may be evidence of soil polygenesis. The *argic* properties of the soils indicate an initial pedogenesis towards Luvisols, which tend to develop more under forest cover (Rusakov et al., 2019). Through subsequent cover with grass vegetation, the soil then developed into the present soil type, towards Phaeozem/Chernozem. The fact that no real B horizons were recognisable is possibly due to overprinting by deepening of the A horizon beyond the B horizon, for example by bioturbation, penetration of deep soil by grass roots and their subsequent decomposition (Kels et al., 2014). At site CJ-3, large root channels with diameters of 5 – 10 cm were found in the soil profile at relatively large depths (A(C) and AC horizon; 160 – 225 cm) that were too large to be from grass vegetation. This is another sign that a vegetation change has taken place in the course of the soil genesis.

The distribution of oxyhydroxides in soils under grassland is also interesting. The amount of crystalline oxyhydroxides of iron has a maximum in the lower horizons at all three sites, which can also be explained by relocation processes that occur together with clay relocation (Graly et al., 2010; Wyshnytzky et al., 2015). While at site CJ-4 the highest content is found in the Bt

horizons, in the other soils the maximum is found in the transition horizons between A and C horizons, i.e. where a B horizon would be found in a Luvisol.

The soil at site CJ-4 was identified as Stagnic Luvisol. This soil type is very common in the Transylvanian Basin, as shown by Gabor et al. (2010), Jakab (2007) and Pendea et al. (2002), among others. Luvisols are typically formed under forest, especially deciduous forest, and are characterised by clay displacement processes, with a *argic* horizon as a diagnostic feature (Zech et al., 2014). Horizon Bmt shows the typical features of a *stagnic* horizon, which suggests a possible transition to Stagnosols. The Am horizon already shows a somewhat increased accumulation of organic material, which can be attributed to the vegetation change from forest to grassland. This process is described by Pendea et al. (2002) for other soils, especially for present-day grass soils that have evolved from Luvisols through the formation of a mollic topsoil. The soil at this site probably shows the condition of the other three soil profiles shortly after a possible vegetation change to grassland and could develop into a similar soil over a long period of time.

4.2 Fallout Nuclides

4.2.1 $^{239+240}\text{Pu}$ Inventory

The $^{239+240}\text{Pu}$ inventory at the reference site was 61 Bq m^{-2} , which lies in the expected range of $50 - 100 \text{ Bq m}^{-2}$ for the Northern hemisphere (Masarik, 2009). The typical distribution of fallout $^{239+240}\text{Pu}$ is a maximum within the uppermost centimetres of the soil surface with an exponential decrease with depth, usually not deeper than 20 – 30 cm in an undisturbed soil (Meusburger et al., 2016). This typical distribution can be seen in the reference site and in sites CJ-3 and CJ-4. The highest inventories of $^{239+240}\text{Pu}$ are found within the top 5 cm, followed by a decrease with depth, and no measurable content of $^{239+240}\text{Pu}$ at a depth of 40 cm, as described by several other studies using $^{239+240}\text{Pu}$ (e.g. Lal et al. (2013); Alewell et al. (2014); Zollinger et al. (2015); Meusburger et al. (2016); Raab (2019)).

Sites CJ-1 and CJ-2 did not show the typical depth distribution. For CJ-1, almost no difference is visible for the inventories of the uppermost 20 cm. Site CJ-2 also shows an almost uniform $^{239+240}\text{Pu}$ inventory for the uppermost 15 cm, only at a depth of 15 – 20 cm the amount of $^{239+240}\text{Pu}$ decreases somewhat. This uniform distribution is most likely due to ploughing (Calitri et al., 2019). Ploughing mixes the $^{239+240}\text{Pu}$ in the soil evenly, which disturbs the natural depth trend. This fact complicates the calculation of erosion rates, as these are largely calculated by the different depth distributions. The erosion rates calculated with PDM and IM should therefore be taken with caution for the two sites CJ-1 and CJ-2, as these are less suitable

for ploughed sites. MODERN, on the other hand, is suitable for sites that have been ploughed. Ploughing as a cause is the logical conclusion especially for site CJ-2, as clear signs of ploughing were found in the soil profile in horizon A1.

Another possibility that could explain the mixing is strong downward movement of the soil. This possibility is especially true for site CJ-1, where large amounts of organic material have been found in deeper layers, as well as the geomorphological shapes in the field, which suggest a movement of the whole soil. In addition, bioturbation by soil-dwelling micro- and macro-organisms may also be mixing the topsoil and homogenising the distribution of $^{239+240}\text{Pu}$ (Alewell et al., 2017).

For site CJ-2, a small amount of $^{239+240}\text{Pu}$ was still measured at a depth of 40 cm. This can also be caused by bioturbation, especially considering the high mixing at this site. In addition, $^{239+240}\text{Pu}$ can be displaced to greater depths by transport of organic material to which the plutonium is attached (Meusburger et al., 2016).

The relatively high $^{239+240}\text{Pu}$ inventory values at site CJ-4 are very likely due to the different vegetation cover compared to the other sites. The measured samples were collected in a meadow outside a forest as well as at the forest edge and in the forest. The meadow still showed characteristics of a forest site, which suggests that this piece of land has not been cleared for too a long time. Forest soils tend to have higher levels of fallout $^{239+240}\text{Pu}$, because at these sites the trees have a filtering effect on aerosols and therefore capture larger parts of the airborne $^{239+240}\text{Pu}$ (Eikenberg et al., 2001; Alewell et al., 2017). By interception, the trapped parts are washed out or brought into the soil by leaf fall.

4.2.2 Erosion Rate

The erosion rate for the period from 1963 until today was assessed using fallout $^{239+240}\text{Pu}$. The different modelling approaches calculated different erosion rates for the individual sample sites. The calculated erosion rates range from $0.70 \text{ t ha}^{-1} \text{ a}^{-1}$ up to $7.89 \text{ t ha}^{-1} \text{ a}^{-1}$. The Romanian Research Institute for Soil Science and Agrochemistry classification classifies these values as low erosion processes (Darja et al., 2002). The values are comparable to the erosion rates recorded by Iurian et al. (2012) for a plot only 8 km from sample site CJ-1. The erosion rates were calculated with the PDM method using fallout ^{137}Cs . The average erosion rate in eroding areas of $9.5 \text{ t ha}^{-1} \text{ a}^{-1}$ from Iurian et al. (2012) is slightly higher than the $6.02 \text{ t ha}^{-1} \text{ a}^{-1}$ (CJ-1) or $7.89 \text{ t ha}^{-1} \text{ a}^{-1}$ (CJ-2). This higher value can be explained, among other things, by the fact that Iurian et al. (2012) measured erosion rates on steeper slopes than is the case for CJ-1 and CJ-2. This is also supported by the higher maximum erosion rates of up to $18 \text{ t ha}^{-1} \text{ a}^{-1}$ of

Iurian et al. (2012).

In a plot close to this one, Iurian et al. (2014) calculated gross erosion rates of $12.2 \text{ t ha}^{-1} \text{ a}^{-1}$.

In a plot around 20 km East of site CJ-3, Iurian et al. (2013) also calculated erosion rates using fallout ^{137}Cs , but modelling the erosion rate using another model (MBM2 by Zapata (2002)). For eroding sites, the calculated erosion rates ranged from $0.1 \text{ t ha}^{-1} \text{ a}^{-1}$ on a very flat surface (3°) up to $7.2 \text{ t ha}^{-1} \text{ a}^{-1}$ and $8.2 \text{ t ha}^{-1} \text{ a}^{-1}$ on steeper surfaces (9.2° , 11.1°).

In a GIS based modelling approach, Patriche (2019) calculates an average soil erosion rate for agricultural lands and slopes $> 5^\circ$ within the entire Transylvanian Depression of $10.83 \pm 11.79 \text{ t ha}^{-1} \text{ a}^{-1}$, and a rate of $6.36 \pm 10.23 \text{ t ha}^{-1} \text{ a}^{-1}$ averaged over all types of terrains.

Ionita et al. (2007)

For a grassland site in North-Eastern Serbia close to the Romanian border, Kalkan et al. (2020) also calculated soil erosion rates using the PDM method. The vegetation cover is similar to the sites in this study and can therefore be compared to a certain degree. Over a slope, Kalkan et al. (2020) measured sole erosion rates from $1.58 \text{ t ha}^{-1} \text{ a}^{-1}$ to $10.60 \text{ t ha}^{-1} \text{ a}^{-1}$, which is similar to the range found in this study.

The slope is often a determining factor of the severity of erosion (Šamonil et al., 2020). For the sites here, this trend of higher erosion rates on steeper slopes was not found. It is possible that the slope differences were not pronounced enough at the first three sites, which would be most comparable, and at site CJ-4 the other formative factors were stronger and reduced the effect of the steeper slope.

Additionally, the position on the slope of the different samples were different, with CJ-1 close to the summit of the hillslope on the one side and CJ-3 in a rather colluvial part of the slope. This can have a possible influence on the erosion rate, the colluvial influence could partly explain the rather low erosion rates at site CJ-3.

At sites CJ-1 and CJ-2, there was one duplicate set each that showed greatly increased erosion values. This can be seen well in Figure 13 by the outliers. The duplicates were both located in the steepest area around the soil profile, which could to some extent explain the increased values. However, the average value of the two duplicates is many times higher and cannot be explained only by the minimal differences in topography. At site CJ-1, traces of grazing and of movements of heavy vehicles were visible, which could have had an influence on the differences in erosion rates. At site CJ-2, traces of agricultural cultivation were visible due to a plough horizon. Ploughing can account for large differences at a very local level. The distribution of erosion rates of the other duplicates was much more comparable, the average erosion rates of $2.7 \text{ t ha}^{-1} \text{ a}^{-1}$ for CJ-1 and $2.4 \text{ t ha}^{-1} \text{ a}^{-1}$ for CJ-2 calculated only with these replicates are

much closer to the erosion rate of $2.8 \text{ t ha}^{-1} \text{ a}^{-1}$ at site CJ-3. A higher number of replicate sets would show whether these high erosion rates were outliers or multiple, because since each of these duplicates accounted for a quarter of the average, the influence of a single one was very high.

The soil profile of site CJ-4 was outside a forest in a meadow that was probably also forested a few decades to centuries ago. In order to determine a possible difference in erosion rates between forest and meadow, the different replicates were divided: two replicates in the open field, two replicates at the edge of the forest and one replicate in the forest. The lowest average erosion rate was found for the replicate in the forest with a rate of only $0.11 \text{ t ha}^{-1} \text{ a}^{-1}$, followed by the sample standing under a large oak at the forest edge with $0.28 \text{ t ha}^{-1} \text{ a}^{-1}$. The values for the replicates in the open field were higher than for the forest replicates, with $1.53 \text{ t ha}^{-1} \text{ a}^{-1}$ and $1.94 \text{ t ha}^{-1} \text{ a}^{-1}$, and more similar to those of the other meadow sites. This finding is consistent with the low erosion rates for forest sites, as cited for example by Meusburger and Alewell (2014).

A comparison of the individual methods shows that there is a correlation with a high coef-

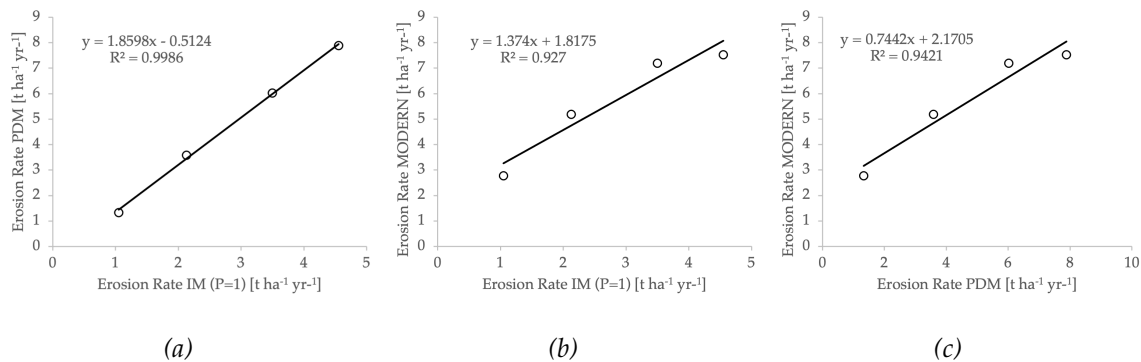


Figure 18: Correlation of the different erosion rates calculated using three different modelling approaches: PDM (Walling and He, 1999), IM (Lal et al., 2013) and MODERN (Arata et al., 2016b)

ficient of determination between all methods (see Figure 18; even though the regression with only four related data pairs tends to have a high coefficient of determination by itself). Meusburger et al. (2016) compared soil erosion rates calculated with MODERN with those calculated with IM. The comparison there was just as significant as here, and the ratio was also approximately the same. The erosion rates calculated using MODERN by Meusburger et al. (2016) were twice as high than those calculated using IM, an observation that is exactly opposite to those made here. At the sites studied here, the erosion rate calculated with MODERN was twice as high than that calculated with IM (P=1). This is probably due to the fact that a small inventory change in the uppermost layers in MODERN leads to stronger erosion rates than in

IM (Arata et al., 2016a). MODERN also has the potential to overestimate erosion rates because the model does not include time-dependent migration of FRN in the soil (Arata et al., 2016a). The comparison of PDM and IM ($P = 1$) shows a surprisingly constant ratio for the first three grass sites (CJ-1, CJ-2 and CJ-3). The erosion rates calculated with PDM are 1.7 times higher than those calculated with IM. For the site influenced by the forest, the ratio is somewhat lower with a factor of 1.3.

The tendency of higher erosion rates calculated with PDM is due to the higher reactivity of the model. Smaller inventory changes lead to larger changes in the calculated erosion rates in this model compared to other models (Calitri et al., 2019).

4.3 Meteoric ^{10}Be

4.3.1 Meteoric ^{10}Be Inventory

The measured inventories of meteoric ^{10}Be range from 0.03×10^8 atoms g^{-1} to 7.15×10^8 atoms g^{-1} , which lies in the broad range as described by Graly et al. (2010). The depth distribution of the ^{10}Be content of sites CJ-2 and CJ-3 shows the typical characteristics of a decline type as described by Graly et al. (2010). This type has the highest ^{10}Be content in the uppermost horizon at the surface, followed by progressively decreasing content with increasing depth, the lowest content being found in the C horizon. CJ-2 has a slightly higher ^{10}Be content in the second uppermost horizon, which Graly et al. (2010) calls bulge. This slightly higher content may be due to mixing of the uppermost parts of the soil (e.g. by ploughing, which may very well serve as an explanation for this site), as well as translocation by bioturbation or by washing of material from the surface into deeper layers. In addition, the lower content of ^{10}Be may be caused by greater erosion on the surface (Graly et al., 2010).

Site CJ-1 also has the typical characteristics of a decline type in the uppermost horizons, but deviates from this type in the AC and C horizons. The content of ^{10}Be is lower in the AC horizon than in the underlying C horizon. A possible explanation for this is a pre-exposure or inheritance of the parent material, i.e. an accumulation of ^{10}Be before the initiation of soil formation (Egli et al., 2010).

Site CJ-4 once again shows very different characteristics compared to the other three sites. First of all, the amount of ^{10}Be in the individual horizons is more than twice as high, with the highest measured value of 7.15×10^8 atoms g^{-1} . Moreover, this peak is not found in the uppermost horizons at the surface as at the other sites, but in the B horizon at a depth of more than one metre. The higher total amounts of ^{10}Be are an indication of a higher age of the investigated soil compared to the others, as the accumulation of ^{10}Be could happen over a longer period of

time (Graly et al., 2010). The shape of the depth distribution shows the typical characteristics of a bulge type as described by Graly et al. (2010). This type shows the highest ^{10}Be contents in the B horizon, followed by a decrease in the underlying horizons. This observation also supports the assumption of a high age, since only with increasing age and a progressive formation of clay and oxyhydroxides through erosion and illuviation processes a transport of ^{10}Be into deeper soil layers occurs. An accumulation of clay in the B horizon can therefore lead to an increase in ^{10}Be content (Graly et al., 2010).

The rather small decrease in the amount of ^{10}Be in the A horizons of site CJ-3 as well as the smooth decrease are a sign of rather high age as well as undisturbed state of the site (Graly et al., 2010). The relatively high accumulation of ^{10}Be in deeper layers can only have developed over a long period of time.

The meteoric ^{10}Be shows a weak correlation ($R^2 = 0.35$, $p < 0.05$) to the dithionite-extractable Fe (amorphous and crystalline forms), a trend which has also been observed by Wyshnytzky et al. (2015). Other studies found correlations for meteoric ^{10}Be with the oxalate-extractable Fe (Egli et al., 2010; Calitri et al., 2019). However, the data here did not show this correlation, despite a visually observed similar depth trend for the both factors. A high affinity of ^{10}Be for organic ligands was observed, leading to increased formation of metallo-organic complexes. Since these are mainly negatively charged, they bind preferentially to the positively charged Fe-oxyhydroxides and Al-oxyhydroxides (Willenbring and von Blanckenburg, 2009; Calitri et al., 2019). A somewhat weaker correlation was found for meteoric ^{10}Be and oxalate-extractable Al ($R^2 = 0.21$, $p < 0.05$), which could be explained by the previous remark. Another weak correlation was found for manganese ($R^2 = 0.30$, $p < 0.05$). Manganese also accumulates strongly in ligand complexes, which could explain the correlation with beryllium.

A correlation between ^{10}Be content and clay content was found by Maejima et al. (2005). Similar to Egli et al. (2010), this correlation could not be found here. However, a negative correlation was found for the silt content in the samples ($R^2 = 0.41$, $p < 0.05$), the lower the silt content, the higher the ^{10}Be content.

4.3.2 Soil Age Determination with Meteoric ^{10}Be

The calculated soil ages of the individual soils range from slightly over 20 ka to an age of over 125 ka for the oldest soil. The ages calculated with the slightly higher ^{10}Be deposition rate of Graly et al. (2011) are all lower than those using a deposition rate of 10^6 (Willenbring and von Blanckenburg, 2009). The high ages are possible because the area was not glaciated during the last ice age, the Carpathian glaciers did not reach this area (Popescu et al., 2017). Therefore, the

soils had a relatively long period in which they could develop and were not destroyed by the glaciers.

The calculated ages of the two sites CJ-1 and CJ-2 are relatively similar. This makes sense because they are on the same hill range, simply on the other side. The fact that soil formation starts relatively simultaneously can be explained by the almost identical environmental conditions.

With the highest soil age at site CJ-4 of up to 120 ka, the beginning of the soil formation would coincide with the end of the penultimate ice age (Riss/Saale glaciation) about 120,000 years ago, the Eemian interglacial. The large amounts of Loess material exposed by the retreating glaciers were transported from the Alpine region as well as from the northern Carpathians into the region of the Carpathian Basin as well as into the Transylvanian Basin (Novothy et al., 2011). This material then served as the basis for soil formation. Jakab (2007) has also found such deposits for terraces in the northern Transylvanian Basin, which would correspond in age to that determined here. Corcea et al. (2013) determined the age of sediments near Cluj-Napoca to be the same age period of about 125 ka. The onset of warming led to a melting of ice in the nearby Apuseni Mountains, which allowed an additional flushing of large amounts of sediment into the lower areas, this in a rather short period of time. These two depositional processes, on the one hand the loess deposits from the glacial area of the Alps, on the other hand the deposits from the nearby Apuseni Mountains, are presumably the parent material of the soil formation, which leads to a maximum age of the soils of the region of about 125 – 130 ka.

The calculated age of about 20 ka at sites CJ-1 and CJ-2 coincide with the onset of climate warming towards the end of the last glacial (Würm/Weichsel glaciation) about 19'000 years ago after the Last Glacial Maximum (Persoiu, 2017). A thawing of the permafrost, which possibly occurred locally in this region (Persoiu, 2017) allowed an incipient reinforced soil formation. Increasing warming in the later millennia allowed soil growth and some permanence.

With a calculated age between 53 and 65 ka, the onset of soil formation at site CJ-3 would fall in a period when climate (especially temperature) was relatively stable (Staubwasser et al., 2018), which would allow initial formation of the soils.

All these ages are minimum ages, possible erosion is not included in these calculations, which leads to an underestimation of the actual ages (Egli et al., 2010). Additionally, ^{10}Be in the soil can interact with acidic solutions percolating the soil and the absorbed ^{10}Be can get washed out, leading to a further age underestimation (Egli et al., 2010). In turn, soil material can be brought in, which can lead to an external supply of ^{10}Be . Similarly, pre-exposure of the parent material

can increase the amount of ^{10}Be , which can lead to an increased estimated age (Egli et al., 2010). This may be the case for the parent material of the profiles described here, especially for site CJ-4. Moore et al. (2021) have shown that deciduous trees have the potential to take up meteoric ^{10}Be from the soil through the roots. This is accumulated in the leaves and distributed on the soil surface with leaf shedding, which can lead to a mixing of the ^{10}Be content. If ^{10}Be from pre-exposed material reaches the surface the calculated soil age is likely overestimated.

The soil ages calculated with q from Graly et al. (2011) depend on the assumed annual rainfall. For the calculation, a value of 600 mm a^{-1} was assumed, which corresponds approximately to today's precipitation amount. Over the long period considered here, this value is not constant but varies considerably, especially between glacial stadials and interstadials, which influence the amount of precipitation (Persoiu, 2017). However, the average amount over the last millennia seems to be a relatively good mean of 600 mm (Persoiu, 2017), which is why this approximation is sufficient for a rough calculation of soil ages.

4.3.3 Long-term Soil Erosion Rate with Meteoric ^{10}Be

The long-term erosion rate based on the meteoric ^{10}Be content was calculated in two different ways. The first as described by Lal (2001), the second method the one according to Zollinger et al. (2017). Both methods use the average annual ^{10}Be deposition rate q as input value. As already described in the part on age determination with meteoric ^{10}Be , the two different values for q from Willenbring and von Blanckenburg (2009) and Graly et al. (2011) were also used. Using two different methods with two different ^{10}Be deposition rates each, four different erosion rates were thus calculated for each site (see Table 9).

The average long-term erosion rate for all calculation methods across all 4 sites is $0.5 \text{ t ha}^{-1} \text{ a}^{-1}$. This is within the range found by other studies in comparable landscape systems. Loba et al. (2021) calculated a long-term erosion rate for agriculturally used loess soils between $0.44 - 0.85 \text{ t ha}^{-1} \text{ a}^{-1}$. For likewise comparable loess soils in south-western Poland, Kołodyńska-Gawrysiak et al. (2018) found a long-term erosion rate of $0.24 - 0.74 \text{ t ha}^{-1} \text{ a}^{-1}$. Only the relatively high erosion rates of CJ-2 of $1.28 \text{ t ha}^{-1} \text{ a}^{-1}$ and $1.00 \text{ t ha}^{-1} \text{ a}^{-1}$ are slightly above these ranges. However, this is not unique, for example Raab et al. (2018) measured erosion rates of up to $3 \text{ t ha}^{-1} \text{ a}^{-1}$, as well as Calitri et al. (2021) for sites in Northern Germany.

The method of Lal (2001) calculates the deeper erosion rates for the grass sites CJ-1, CJ-2 and CJ-3 than the method of Zollinger et al. (2017). The values are two and a half to seven times greater. For the fourth site CJ-4, the method according to Lal (2001) produces higher values. For the first three sites, a correlation ($R^2 < 0.9$) is visible for all combinations, but not when site

CJ-4 is also considered. This is probably due to the differences between the grass sites and site CJ-4. The deep A horizons of CJ-1 – 3 are used for the Lal (2001) method compared to the C horizon, and without B horizon. The amount of inventory decline compared to the C horizon is lower here. The comparatively thin A horizon at site CJ-4 accounts for a larger proportion in comparison, so erosion here has a greater effect in Lal (2001).

The erosion rate calculation according to Zollinger et al. (2017) requires a maximum age of the investigated soils. As discussed in the last part, the assumed maximum age is about 125 ka (Corcea et al., 2013). To include a possible initiation phase of soil formation, a maximum age of 130 ka was used for the calculation. However, the influence of the maximum age factor is rather small, even a difference of several tens of thousands of years only changes the erosion rate by a few tens of $\text{kg ha}^{-1} \text{a}^{-1}$.

4.4 In-situ ^{10}Be

4.4.1 In-situ ^{10}Be Age Determination

The calculated ages of the one outcrop show no real age trend. The maximum age of about 7.8 ka was measured at mid-height, the higher, theoretically oldest measuring point was younger. A possible age trend can only be determined for the lower two measuring points CJ-11 and CJ-12, but this one single age difference is not sufficient to calculate a possible erosion rate. The uppermost measuring point CJ-13 was either exposed later or, more likely, a piece broke off and the collected material was therefore exposed later. If the second site had given enough quartz, a more accurate determination might have been possible.

The sample points may also have all been exposed at the same time, for example by a single erosion event (landslide, heavy rainfall event, etc.).

With a maximum age of about 7.8 ka, the outcrop was exposed at a time when soil formation in this area had already been going on for millennia (Corcea et al., 2013; Jakab, 2007). The site is located in the relatively narrow river valley of the Iara River. It is therefore possible that the outcrop was exposed in a relatively short period of time due to deepening of the riverbed.

4.4.2 In-situ ^{10}Be Erosion Rate Determination

The estimated soil erosion rate of $0.20 \text{ t ha}^{-1} \text{a}^{-1}$ is in similar ranges as the values calculated with other methods. However, this value is only calculated very inaccurately, because only the maximum age was calculated to calculate the lowest value. If the lower age of the lowest point CJ-Be11 were used, the erosion rate would be slightly higher.

4.5 Erosion Rate from Soil Formation Modelling

The calculated erosion rates are in a similar range as the long-term erosion rates calculated with other methods. For site CJ-2, no erosion rate could be calculated because the calculated soil depth was smaller than the actually measured one. This is due to the very low particle size d_{50} of only 7.09 μm . The calculated soil depth is thus estimated to be rather too deep, since smaller particles lead to larger surfaces, which influence percolation. The value for d_{50} of site CJ-2 is also the only one that deviates excessively from the average values calculated by Egli et al. (2018).

The method is based on a large number of estimated factors. As in other methods for calculating long-term erosion rates, the amount of precipitation has a major influence on the results. In addition, there are other factors that need to be estimated. The infiltration rate of precipitation into the soil as well as evapotranspiration can vary greatly over the entire study period. In addition, d_{50} was only calculated from three soil samples per site, a calculation with all discernible soil horizons would probably have yielded more accurate results, including a result for site CJ-2.

4.6 Comparison of Different Soil Erosion Rates

4.6.1 Comparison of the Long-term Erosion Rates

The long-term erosion rates of the different sites were determined in two different ways. The first is the determination with meteoric ^{10}Be from the different soil horizons, the second is an approach that calculates the soil depth using a percolation model, which can then be used to calculate a soil erosion rate. A third method to calculate long-term erosion, the in-situ ^{10}Be method could only be used to calculate a rough approximation of the erosion rate, as there was no distinct age trend between the different samples. A compilation of all calculated long-term erosion rates can be found in Table ???. The different erosion rates calculated using the meteoric ^{10}Be method have already been discussed in that related part. The erosion rates calculated with the method of Egli et al. (2018) correspond very well to the values for the first three grassland profiles calculated with the method of Lal (2001) with a q of Graly et al. (2011). For sites CJ-1 and CJ-3 the erosion rates are almost identical. For site CJ-4, a practically identical erosion rate was calculated for the method according to Egli et al. (2018) and Zollinger et al. (2017) with q of Willenbring and von Blanckenburg (2009). The approximation arrived at using the in-situ ^{10}Be method at a rate of 0.20, or 0.24 $\text{t ha}^{-1} \text{a}^{-1}$ tends to be in the lower range of calculated erosion rates, but reflects the approximate range of the other methods.

The average long-term erosion rates range from 0.17 t ha⁻¹ a⁻¹ and 0.78 t ha⁻¹ a⁻¹, the average rate across all sites is 0.44 t ha⁻¹ a⁻¹, a rather low value in a range also found by others, for example Kołodyńska-Gawrysiak et al. (2018) or Loba et al. (2021). The relatively good agreement between the erosion rates calculated with different methods is an indication of the quality of the calculations. Since similar results were obtained with two independent methods, the range of soil erosion rates seems to be correct.

Table 11: Summary of all long-term erosion rates for the four soil sites calculated using different approaches, and the average long-term soil erosion rate of all methods.

	Lal (2001) using q by Graly et al. (2011)	Lal (2001) using q by Willenbring and von Blanckenburg (2009)	Zollinger et al. (2017) using q by Graly et al. (2011)	Zollinger et al. (2017) using q by Willenbring and von Blanckenburg (2009)	Egli et al. (2018)	Average of all Methods
Site	t ha ⁻¹ a ⁻¹	t ha ⁻¹ a ⁻¹	t ha ⁻¹ a ⁻¹	t ha ⁻¹ a ⁻¹	t ha ⁻¹ a ⁻¹	t ha ⁻¹ a ⁻¹
CJ-1	0.29	0.24	0.79	0.62	0.3	0.45
CJ-2	0.47	0.38	1.28	1	-	0.78
CJ-3	0.17	0.14	0.74	0.53	0.16	0.35
CJ-4	0.31	0.25	0.13	0.04	0.13	0.17

4.6.2 Comparison Long-term Erosion Rates – Short-term Erosion Rates

The erosion rates for the different sites were determined over two different time periods. The first period covers the entire span since the onset of soil genesis of the soils considered here, i.e. a long-term erosion rate. These values were calculated using two different methods, the first using the distribution of meteoric ¹⁰Be in the soil, the second using an approach that calculates a theoretical soil depth based on a percolation theory. The second period covers the period since the nuclear bomb peak in 1963, i.e. a period of about 60 years, referred to here as the short-term erosion rate. Values for short-term erosion rates were calculated based on the content and distribution of fallout ²³⁹⁺²⁴⁰Pu in the studied sites compared to a reference site.

The erosion rates are very different for the two periods. The short-term erosion rates over the last 60 years are larger than the corresponding long-term erosion rates by a factor of 7 to almost 10. This finding is consistent with that of Kołodyńska-Gawrysiak et al. (2018) and Loba et al. (2021), who found similar relationships between short-term and long-term erosion rates. These large differences can have different causes, on the one hand natural fluctuations, mainly due to climate changes, which lead to an increase in erosion (Smithson et al., 2008) and on the other

hand anthropogenic causes. The extreme increase in short-term erosion rate compared to long-term erosion rate can only be attributed to natural processes to a limited extent. The human factor has a strong influence on the high erosion rates found here. Large areas of Romanian farmland are affected by severe soil erosion (Ionita et al., 2007; Mircea et al., 2010). The reasons for this are mainly poor farming techniques, which first led to soil degradation under communist leadership increasingly since the sixties, but even more so since soil erosion controls were not really enforced after the fall of the communist regime (Mircea et al., 2010). A major contributor to soil erosion is uphill and downhill ploughing, which has been increasingly used again since the 1990s instead of contour ploughing. In addition, increased fallowing, as well as non-compliance with alternate field cultivation are reasons for increased erosion values Ionita and Margineanu (2000); Mircea et al. (2010).

The long-term erosion rate is most comparable to the erosion rates of the samples in the forest at site CJ-4 in the short term. Forests lead to lower erosion rates because the canopy reduces the energy of precipitation through interception, and in addition the many roots of the trees stabilise the soil (IAEA, 2014). Deforestation and conversion to grassland or crop land can, in turn, lead to an increase in soil erosion. This change has taken place in many areas in Romania, which may contribute to the high erosion rates (Mircea et al., 2010). The similarity between the long-term erosion rate and the erosion rate in the forest could possibly be an indication that the areas were forested over some period of time and therefore have the same erosion rates as those found in the forest. This would speak for a vegetation change rather than a Holocene continuity of the grassland at the sites studied here.

According to Alewell et al. (2015), a tolerable soil erosion rate must not be greater than the rate of soil production, because this would lead to soil degradation. Young soils tend to have the highest production rates, with increasing age this decreases progressively. Since the soils studied here are all of a high age, it can be assumed that the production rate is rather low. Accordingly, the erosion rate must not be very high in order to prevent soil degradation. The average long-term erosion rates of the individual sites are near the tolerable soil erosion rates of 0.5 to 1 t ha⁻¹ a⁻¹ mentioned by Alewell et al. (2015). However, the short-term erosion rates of the last almost 60 years are strongly above this, which leads to a strong degradation of the soils over longer periods of time.

4.7 Holocene Continuity

The strongly developed soils at the grassland sites CJ-1, CJ-2 and CJ-3 indicate that the present vegetation condition tends to persist for a long time. Above all, the decarbonatisation at great

depth, especially at site CJ-3, speak for a relatively high age of the soils found here. This is also supported by the relatively high ages of the soils investigated here. However, the ages do not exclude a change in vegetation and associated changes in the soils.

The soils at sites CJ-1, CJ-2 and CJ-3 show evidence of polygenesis. This might be due to a change in vegetation from forest to grassland, which would argue against a continuity of grassland throughout the Holocene at these sites. Characteristics such as clay displacement as well as remains of large root channels at great depths speak rather for a forestation of the investigated sites. However, a vegetation change probably took place relatively long ago due to the strongly pronounced organic horizons. However, the profiles studied here are only point measurements, which need not be representative of the entire environment. The presence of features indicative of forest could also come only from individual trees that stood here at some time in the past, and which did not necessarily result in a closed forest cover.

The different erosion rates vary considerably. The high recent erosion rates are probably largely due to the strong anthropogenic influence of the last 60 years. The long-term erosion rates of all sites are most similar to those under forest cover at site CJ-4, possibly indicating such a vegetation type for a large part of the time periods studied.

5 Conclusions, Outlook and Perspectives

This Master's thesis investigated different soils in a forest-steppe landscape in the area around the city of Cluj-Napoca, Transylvania, Romania. With growing evidence, grasslands with patches of open forest in these ecosystems exist continuously through the Holocene despite climatic suitability for closed forest cover.

Four soil profiles were studied, their soil taxonomical units were determined and the content of different elements was investigated to determine possible factors influencing soil genesis. Three of the studied soils (CJ-1, CJ-2 and CJ-3) were determined to be Chernic Luvisols. The displacement of clay as well as iron and other elements, the existence of large root channels at great depths and the presence of prismatic soil structures are indications of a possible polygenesis of the soils. The fourth soil at site CJ-4 was classified as Stagnic Luvisol, indicating a relatively recent clearing of forest at this site or a transition from forest vegetation to grassland vegetation. Many of the characteristics of this soil unit are visible, albeit overprinted, at the other sites, suggesting possible past land cover at these sites.

Using different methods, soil erosion rates were determined over different periods of time. Long-term rates over the period since the beginning of the formation of the investigated soils

were calculated using meteoric ^{10}Be content in the individual soil horizons. A second method of calculating long-term erosion rates was an approach that created a theoretical soil depth based on infiltration of precipitation into the soil as well as grain size composition. Short-term erosion rates for the last 60 years or so were calculated using the distribution of fallout $^{239+240}\text{Pu}$.

As hypothesised, the short-term erosion rates are several times higher than the erosion rates over the entire soil formation with average erosion rates ranging from $1.35 \text{ t ha}^{-1} \text{ a}^{-1}$ to $5.4 \text{ t ha}^{-1} \text{ a}^{-1}$ over the last almost 60 years and long-term erosion rates between $0.18 \text{ t ha}^{-1} \text{ a}^{-1}$ and $0.78 \text{ t ha}^{-1} \text{ a}^{-1}$. The large differences are mainly due to human causes, largely incorrect agricultural management and conversion of forest areas into grasslands. To a lesser extent, however, changes in land cover can also explain the differences, because the short-term erosion rates of samples taken in the forest correspond fairly well to the long-term erosion rates. This suggests that some of the areas studied were previously forested.

The total content of meteoric ^{10}Be was used to determine the minimum age of the soils. As predicted, the ages are very high, with values between 20 ka and 125 ka, the times of onset of soil formation are before the Holocene in the Pleistocene. An age determination of the soils using an approach with in-situ ^{10}Be yielded only limited useful results. Accordingly, these data could only be used to determine a roughly approximated soil denudation rate. A second set of data in a first leaching run did not yield enough material for an analysis, a reprocessing of these data could possibly give a more accurate picture of the age distribution as well as the long-term erosion.

An age determination of the strongly pronounced A horizons at sites CJ-1, CJ-2 and CJ-3 (for example by using the ^{14}C method) could narrow down the time period at which a possible vegetation change took place. The project in which this work is embedded is also investigating other features of the same sites. These results in combination with those of this work will help to draw a more accurate picture of the situation during the Holocene. Thus, micro- and macro-traces of plants can provide further evidence of vegetation change and thus support the results found here.

References

- Alewell, C., Egli, M., and Meusburger, K. 2015. An attempt to estimate tolerable soil erosion rates by matching soil formation with denudation in Alpine grasslands. *Journal of Soils and Sediments*, 15(6):1383–1399.
- Alewell, C., Meusburger, K., Juretzko, G., Mabit, L., and Ketterer, M. E. 2014. Suitability of $^{239+240}\text{Pu}$ and ^{137}Cs as tracers for soil erosion assessment in mountain grasslands. *Chemosphere*, 103:274–280.
- Alewell, C., Pitois, A., Meusburger, K., Ketterer, M., and Mabit, L. 2017. $^{239} + ^{240}\text{Pu}$ from "contaminant" to soil erosion tracer: Where do we stand? *Earth-Science Reviews*, 172(July):107–123.
- Arata, L., Alewell, C., Frenkel, E., A'Campo-Neuen, A., Iurian, A. R., Ketterer, M. E., Mabit, L., and Meusburger, K. 2016a. Modelling Deposition and Erosion rates with RadioNuclides (MODERN) - Part 2: A comparison of different models to convert $^{239+240}\text{Pu}$ inventories into soil redistribution rates at unploughed sites. *Journal of Environmental Radioactivity*, 162-163:97–106.
- Arata, L., Meusburger, K., Frenkel, E., A'Campo-Neuen, A., Iurian, A. R., Ketterer, M. E., Mabit, L., and Alewell, C. 2016b. Modelling Deposition and Erosion rates with RadioNuclides (MODERN) - Part 1: A new conversion model to derive soil redistribution rates from inventories of fallout radionuclides. *Journal of Environmental Radioactivity*, 162-163:45–55.
- Balco, G., Stone, J. O., Lifton, N. A., and Dunai, T. J. 2008. A complete and easily accessible means of calculating surface exposure ages or erosion rates from ^{10}Be and ^{26}Al measurements. *Quaternary Geochronology*, 3(3):174–195.
- Borchers, B., Marrero, S., Balco, G., Caffee, M., Goehring, B., Lifton, N., Nishiizumi, K., Phillips, F., Schaefer, J., and Stone, J. 2016. Geological calibration of spallation production rates in the CRONUS-Earth project. *Quaternary Geochronology*, 31:188–198.
- Borggaard, O. K. 1988. Phase Identification by Selective Dissolution Techniques. *Iron in Soils and Clay Minerals*, pages 83–98.
- Calitri, F., Sommer, M., Norton, K., Temme, A., Brandová, D., Portes, R., Christl, M., Ketterer, M. E., and Egli, M. 2019. Tracing the temporal evolution of soil redistribution rates in an agricultural landscape using $^{239+240}\text{Pu}$ and ^{10}Be . *Earth Surface Processes and Landforms*, 44(9):1783–1798.

- Calitri, F., Sommer, M., van der Meij, W. M., Tikhomirov, D., Christl, M., and Egli, M. 2021. ^{10}Be and ^{14}C data provide insight on soil mass redistribution along gentle slopes and reveal ancient human impact. *Journal of Soils and Sediments*.
- Chmeleff, J., von Blanckenburg, F., Kossert, K., and Jakob, D. 2010. Determination of the ^{10}Be half-life by multicollector ICP-MS and liquid scintillation counting. *Nuclear Instruments and Methods in Physics Research, Section B: Beam Interactions with Materials and Atoms*, 268(2):192–199.
- Christl, M., Vockenhuber, C., Kubik, P. W., Wacker, L., Lachner, J., Alfimov, V., and Synal, H. A. 2013. The ETH Zurich AMS facilities: Performance parameters and reference materials. *Nuclear Instruments and Methods in Physics Research, Section B: Beam Interactions with Materials and Atoms*, 294:29–38.
- Corcea, C. A., Constantin, D., Anechitei, V., Timar-Gabor, A., and Filipescu, S. 2013. SAR OSL dating of 63-90 μm quartz extracted from an Eemian (presumably lacustrine) sedimentary section at Floresti on the Somesul Mic Valley. *Carpathian Journal of Earth and Environmental Sciences*, 8(1):139–145.
- Darja, M., Budiu, V., Tripon, D., and Pacurar, I. 2002. *Eroziunea hidrica si impactul asupra mediului*. Risoprint, Cluj-Napoca.
- Dawson, T. P., Jackson, S. T., House, J. I., Prentice, I. C., and Mace, G. M. 2011. Beyond Predictions : Biodiversity Conservation in a Changing Climate. *Science*, 332(6025):53–58.
- Dengler, J., Becker, T., Ruprecht, E., Szabó, A., Becker, U., Beldean, M., Bită-Nicolae, C., Dolnik, C., Goia, I., Peyrat, J., Sutcliffe, L. M., Turtureanu, P. D., and Ugurlu, E. 2012. Festuco-Brometea communities of the Transylvanian Plateau (Romania) - A preliminary overview on syntaxonomy, ecology, and biodiversity. *Tuexenia*, 32(1):319–359.
- Dunai, T. J. 2010. *Cosmogenic Nuclides: Principles, Concepts and Applications in the Earth Surface Sciences*. Cambridge University Press, Cambridge.
- Dunai, T. J. and Lifton, N. A. 2014. The nuts and bolts of cosmogenic nuclide production. *Elements*, 10(5):347–350.
- Egli, M., Brandová, D., Böhlert, R., Favilli, F., and Kubik, P. W. 2010. ^{10}Be inventories in Alpine soils and their potential for dating land surfaces. *Geomorphology*, 119(1-2):62–73.

- Egli, M., Hunt, A. G., Dahms, D., Raab, G., Derungs, C., Raimondi, S., and Yu, F. 2018. Prediction of soil formation as a function of age using the percolation theory approach. *Frontiers in Environmental Science*, 6(September):1–21.
- Egli, M. and Mirabella, A. 2021. The Origin and Formation of Clay Minerals in Alpine Soils. In Hunt, A. G., Egli, M., and Faybishenko, B., editors, *Hydrogeology, Chemical Weathering and Soil Formation*, chapter 6, pages 121–137. Wiley.
- Eikenberg, J., Bajo, S., Hitz, J., and Wyer, L. 2001. Environmental radionuclide analyses around nuclear installations in Northern Switzerland. *Proceedings of the 47th Annual Radiochemical Measurement Conference Honolulu*, pages 1–6.
- FAO 2014. World Reference Base for Soil Resources. *World Soil Resources Reports No. 106*, pages 1–191.
- Feurdean, A., Marinova, E., Nielsen, A. B., Liakka, J., Veres, D., Hutchinson, S. M., Braun, M., Timar-Gabor, A., Astalos, C., Mosbrugger, V., and Hickler, T. 2015. Origin of the forest steppe and exceptional grassland diversity in Transylvania (central-eastern Europe). *Journal of Biogeography*, 42(5):951–963.
- Feurdean, A., Ruprecht, E., Molnár, Z., Hutchinson, S. M., and Hickler, T. 2018. Biodiversity-rich European grasslands: Ancient, forgotten ecosystems. *Biological Conservation*, 228(May):224–232.
- Gabor, A. T., Vasiliniuc, S., Badarau, A. S., Begy, R., and Cosma, C. 2010. Testing the potential of optically stimulated luminescence dating methods for dating soil covers from the forest steppe zone in Transylvanian Basin. *Carpathian Journal of Earth and Environmental Sciences*, 5(2):137–144.
- Gosse, J. C. and Phillips, F. M. 2001. Terrestrial in situ cosmogenic nuclides: theory and application. *Quaternary Science Reviews*, 20:1475–1560.
- Graly, J. A., Bierman, P. R., Reusser, L. J., and Pavich, M. J. 2010. Meteoric ^{10}Be in soil profiles - A global meta-analysis. *Geochimica et Cosmochimica Acta*, 74(23):6814–6829.
- Graly, J. A., Reusser, L. J., and Bierman, P. R. 2011. Short and long-term delivery rates of meteoric ^{10}Be to terrestrial soils. *Earth and Planetary Science Letters*, 302(3–4):329–336.
- Gu, Z. Y., Lal, D., Liu, T. S., Guo, Z. T., Southon, J., and Caffee, M. W. 1997. Weathering histories of Chinese loess deposits based on uranium and thorium series nuclides and cosmogenic ^{10}Be . *Geochimica et Cosmochimica Acta*, 61(24):5221–5231.

- Hájek, M., Hájková, P., and Roleček, J. 2020. A novel dataset of permanent plots in extremely species-rich temperate grasslands. *Folia Geobotanica*, 55(3):257–268.
- IAEA 2014. Guidelines for Using Fallout Radionuclides to Assess Erosion and Effectiveness of Soil Conservation Strategies. Technical report.
- Ionita, I. and Margineanu, R. M. 2000. Application of ^{137}Cs for measuring soil erosion/deposition rates in Romania. *Acta Geologica Hispanica*, 35(3-4):311–319.
- Ionita, I., Radoane, M., and Mircea, S. 2007. Romania. In Boardman, J. and Poesen, J., editors, *Soil Erosion in Europe*, chapter 1.13, page 878. John Wiley & Sons, Chichester.
- Iurian, A.-R., Begy, R., Catinas, I., and Cosma, C. 2012. Results of Medium-Term Soil Redistribution Rates in Cluj County, Romania, using ^{137}Cs Measurements. *Procedia Environmental Sciences*, 14:22–31.
- Iurian, A. R., Mabit, L., Begy, R., and Cosma, C. 2013. Comparative assessment of erosion and deposition rates on cultivated land in the Transylvanian Plain of Romania using ^{137}Cs and ^{210}Pb ex. *Journal of Environmental Radioactivity*, 125:40–49.
- Iurian, A. R., Mabit, L., and Cosma, C. 2014. Uncertainty related to input parameters of ^{137}Cs soil redistribution model for undisturbed fields. *Journal of Environmental Radioactivity*, 136:112–120.
- Ivy-Ochs, S. and Kober, F. 2008. Surface exposure dating with cosmogenic nuclides. *Quaternary Science Journal*, 57(1/2):179–209.
- Jakab, S. 2007. Chrono-toposequences of soils on the river terraces in Transylvania (Romania). *Catena*, 71(3):406–410.
- Kalkan, K. S., Forkapić, S., Marković, S. B., Bikit, K., Gavrilov, M. B., Tošić, R., Mrcroscrossed D Signa, D., and Lakatoš, R. 2020. The application of ^{137}Cs and ^{210}Pb ex methods in soil erosion research of Titel loess plateau, Vojvodina, Northern Serbia. *Open Geosciences*, 12(1):11–24.
- Kelley, J. M., Bond, L. A., and Beasley, T. M. 1999. Global distribution of Pu isotopes and ^{237}Np . *Science of the Total Environment*, 237-238:483–500.
- Kels, H., Protze, J., Sitlivy, V., Hilgers, A., Zander, A., Anghelinu, M., Bertrams, M., and Lehmkuhl, F. 2014. Genesis of loess-like sediments and soils at the foothills of the Banat

- Mountains, Romania - Examples from the Paleolithic sites Romanesti and Cosava. *Quaternary International*, 351(C):213–230.
- Ketterer, M. E. 2015. Standard Operating Procedures for Preparation of Soils and Sediments for $^{239+240}\text{Pu}$ Activity and $^{240}\text{Pu}/^{239}\text{Pu}$ Atom Ratio Measurements - Acid Leaching and Quadrupole ICPMS.
- Kohl, C. P. and Nishiizumi, K. 1992. Chemical isolation of quartz for measurement of in-situ -produced cosmogenic nuclides. *Geochimica et Cosmochimica Acta*, 56(9):3583–3587.
- Kołodzyńska-Gawrysiak, R., Poesen, J., and Gawrysiak, L. 2018. Assessment of long-term Holocene soil erosion rates in Polish loess areas using sedimentary archives from closed depressions. *Earth Surface Processes and Landforms*, 43(5):978–1000.
- Lal, D. 2001. New Nuclear Methods for Studies of Soil Dynamics Utilizing Cosmic Ray Produced Radionuclides. In *Sustain the Global Farm: Selected papers from the 10th International Soil Conservation Organization Meeting held May 24-29 at Purdue University and the USDA-ARS National Soil Erosion Research Laboratory*, pages 1044–1052. Purdue University West Lafayette.
- Lal, R., Tims, S. G., Fifield, L. K., Wasson, R. J., and Howe, D. 2013. Applicability of ^{239}Pu as a tracer for soil erosion in the wet-dry tropics of northern Australia. *Nuclear Instruments and Methods in Physics Research, Section B: Beam Interactions with Materials and Atoms*, 294:577–583.
- Loba, A., Waroszewski, J., Tikhomirov, D., Calitri, F., Christl, M., Sykuła, M., and Egli, M. 2021. Tracing erosion rates in loess landscape of the Trzebnica Hills (Poland) over time using fallout and cosmogenic nuclides. *Journal of Soils and Sediments*, 21(8):2952–2968.
- Maejima, Y., Matsuzaki, H., and Higashi, T. 2005. Application of cosmogenic ^{10}Be to dating soils on the raised coral reef terraces of Kikai Island, southwest Japan. *Geoderma*, 126(3-4):389–399.
- Magyari, E. K., Chapman, J. C., Passmore, D. G., Allen, J. R., Huntley, J. P., and Huntley, B. 2010. Holocene persistence of wooded steppe in the Great Hungarian Plain. *Journal of Biogeography*, 37(5):915–935.
- Masarik, J. 2009. Origin and Distribution of Radionuclides in the Continental Environment. In Froehlich, K., editor, *Radioactivity in the Environment*, chapter 1, pages 1–25. Elsevier.
- McKeague, J., Brydon, J., and Miles, N. 1971. Differentiation of Forms of Extractable Iron and Aluminum in Soils. 35(1):33–38.

- Meusburger, K. and Alewell, C. 2014. *Soil Erosion in the Alps. Experience gained from case studies (2006 – 2013)*. Federal Office for the Environment, Bern.
- Meusburger, K., Mabit, L., Ketterer, M., Park, J. H., Sandor, T., Porto, P., and Alewell, C. 2016. A multi-radionuclide approach to evaluate the suitability of $^{239} + ^{240}\text{Pu}$ as soil erosion tracer. *Science of the Total Environment*, 566-567:1489–1499.
- Mircea, S., Petrescu, N., Musat, M., Radu, A., and Sarbu, N. 2010. Soil Erosion and Conservation in Romania - Some Figures, Facts and its Impact on Environment. *Annals of Food Science and Technology*, 11(1):105 – 110.
- Moore, A. K., Granger, D. E., and Conyers, G. 2021. Beryllium cycling through deciduous trees and implications for meteoric ^{10}Be systematics. *Chemical Geology*, 571(October 2020):120174.
- Novothny, Á., Frechen, M., Horváth, E., Wacha, L., and Rolf, C. 2011. Investigating the penultimate and last glacial cycles of the Sütto{double acute} loess section (Hungary) using luminescence dating, high-resolution grain size, and magnetic susceptibility data. *Quaternary International*, 234(1-2):75–85.
- Paltineanu, C., Lacatusu, R., Vranceanu, A., Vizitiu, O., and Lacatusu, A. R. 2020. Comparing soil physical properties in forest soils and arable soils within heavy-clay Phaeozems: an environmental case study in Romania. *Agroforestry Systems*, 94(1):113–123.
- Patriche, C. V. 2019. Quantitative assessment of rill and interrill soil erosion in Romania. *Soil Use and Management*, 35(2):257–272.
- Pecl, G. T., Araújo, M. B., Bell, J. D., Blanchard, J., Bonebrake, T. C., Chen, I.-c., Clark, T. D., Colwell, R. K., Danielsen, F., Evengård, B., Falconi, L., Ferrier, S., Frusher, S., Garcia, R. A., Griffis, R. B., Hobday, A. J., Janion-scheepers, C., Jarzyna, M. A., Jennings, S., Lenoir, J., Linnetved, H. I., Martin, V. Y., McCormack, P. C., McDonald, J., Mitchell, N. J., Mustonen, T., Pandolfi, J. M., Pettorelli, N., Popova, E., Robinson, S. A., Scheffers, B. R., Shaw, J. D., Sorte, C. J. B., Strugnell, J. M., Sunday, J. M., and Tuanmu, M.-n. 2017. Biodiversity redistribution under climate change: Impacts on ecosystems and human well-being. *Science*, 355(6332).
- Pendea, F., Szántó, Z., Badarau, A., and Dezsi, S. 2002. Age and Pedogenic Reconstruction of a Paleo-Relict Chernozem Soil from Central Transylvanian Basin. *Geologica Carpatica*, 53:37.
- Pendea, I. F., Gray, J. T., Ghaleb, B., Tantau, I., Badarau, A. S., and Nicorici, C. 2009. Episodic build-up of alluvial fan deposits during the Weichselian Pleniglacial in the western Transyl-

- vania Basin, Romania and their paleoenvironmental significance. *Quaternary International*, 198(1-2):98–112.
- Persoiu, A. 2017. Climate evolution during the late glacial and the holocene. In *Landform Dynamics and Evolution in Romania*, chapter 3, pages 57–66.
- Popescu, R., Urdea, P., and Vespremeanu-Stroe, A. 2017. Deglaciation history of high massifs from the Romanian carpathians: Towards an integrated view. In Radoane, M. and Vespremeanu-Stroe, A., editors, *Landform Dynamics and Evolution in Romania*, chapter 5, pages 87–116. Springer, Cham.
- Raab, G. 2019. *The Tor Exhumation Approach - A New Technique to Derive Continuous In-Situ Soil Erosion and Surface Denudation Models*. Phd thesis, University of Zurich.
- Raab, G., Egli, M., Norton, K., Dahms, D., Brandová, D., Christl, M., and Scarciglia, F. 2019. Climate and relief-induced controls on the temporal variability of denudation rates in a granitic upland. *Earth Surface Processes and Landforms*, 44(13):2570–2586.
- Raab, G., Martin, A. P., Norton, K. P., Christl, M., Scarciglia, F., and Egli, M. 2021. Complex patterns of schist tor exposure and surface uplift, Otago (New Zealand). *Geomorphology*, 389:107849.
- Raab, G., Scarciglia, F., Norton, K., Dahms, D., Brandová, D., de Castro Portes, R., Christl, M., Ketterer, M. E., Ruppli, A., and Egli, M. 2018. Denudation variability of the Sila Massif upland (Italy) from decades to millennia using ^{10}Be and $^{239+240}\text{Pu}$. *Land Degradation and Development*, 29(10):3736–3752.
- Rusakov, A., Makeev, A., Kurbanova, F., Denisova, E., Popov, A., Fedorova, M., and Timofeev, V. 2019. Late Holocene Landscape Dynamic in the Forest-Steppe Area of the Russian Plain Based on the Study of Soil Chronosequence (The Borisovka Scythian Settlement). In *The Third Plenary Meeting and Field Trip of INQUA IFG 1709F POCAS, Tehran and Guilan Province, I.R. Iran*, pages 127–131.
- Šamonil, P., Egli, M., Steinert, T., Norton, K., Abiven, S., Daněk, P., Hort, L., Brandová, D., Christl, M., and Tikhomirov, D. 2020. Soil denudation rates in an old-growth mountain temperate forest driven by tree uprooting dynamics, Central Europe. *Land Degradation and Development*, 31(2):222–239.
- Šamonil, P., Schatzl, R. J., Valtera, M., Goliáš, V., Baldrian, P., Vašíčková, I., Adam, D., Janík,

- D., and Hort, L. 2013. Crossdating of disturbances by tree uprooting: Can treethrow microtopography persist for 6000years? *Forest Ecology and Management*, 307:123–135.
- Smithson, P., Addison, K., and Atkinson, K. 2008. *Fundamentals of the Physical Environment*. Routledge, London, 4th edition.
- Staubwasser, M., Dragusin, V., Onac, B. P., Assonov, S., Ersek, V., Hoffmann, D. L., and Veres, D. 2018. Impact of climate change on the transition of Neanderthals to modern humans in Europe. *Proceedings of the National Academy of Sciences of the United States of America*, 115(37):9116–9121.
- Tahas, S.-V., Ristoiu, D., and Cosma, C. 2011. Analysis of Global Solar Radiation and Precipitation Trends in Cluj-Napoca, Romania, over the Period 1921-2009. 6(2):289–302.
- von Blanckenburg, F. 2004. Cosmogenic nuclide evidence for low weathering and denudation in the wet, tropical highlands of Sri Lanka. *Journal of Geophysical Research*, 109(F3).
- von Blanckenburg, F., Belshaw, N. S., and O’Nions, R. K. 1996. Separation of ⁹Be and cosmogenic ¹⁰Be from environmental materials and SIMS isotope dilution analysis. *Chemical Geology*, 129(1-2):93–99.
- Walling, D. E. and He, Q. 1999. Improved Models for Estimating Soil Erosion Rates from Cesium-137 Measurements. *Journal of Environmental Quality*, 28(2):611–622.
- Walling, D. E. and Quine, T. A. 1990. Calibration of caesium-137 measurements to provide quantitative erosion rate data. *Land Degradation & Rehabilitation*, 2(3):161–175.
- Weindorf, D., Haggard, B., and Rusu, T. 2009. Soil Temperatures of the Transylvanian Plain, Romania. *Bulletin of University of Agricultural Sciences and Veterinary Medicine Cluj-Napoca - Agriculture*, 66(1):237–242.
- Willenbring, J. K. and von Blanckenburg, F. 2009. Meteoric cosmogenic Beryllium-10 adsorbed to river sediment and soil: Applications for Earth-surface dynamics. *Earth-Science Reviews*, 98(1-2):105–122.
- Willner, W., Roleček, J., Korolyuk, A., Dengler, J., Chytrý, M., Janišová, M., Lengyel, A., Acic, S., Becker, T., Cuk, M., Demina, O., Jandt, U., Kacki, Z., Kuzemko, A., Kropf, M., Lebedeva, M., Semenishchenkov, Y., Šilc, U., Stancic, Z., Staudinger, M., Vassilev, K., and Yamalov, S. 2019. Formalized classification of semi-dry grasslands in central and eastern Europe. *Preslia*, 91(1):25–49.

- Wilson, J. B., Peet, R. K., Dengler, J., and Pärtel, M. 2012. Plant species richness: The world records. *Journal of Vegetation Science*, 23(4):796–802.
- Wyshnytzky, C. E., Ouimet, W. B., McCarthy, J., Dethier, D. P., Shroba, R. R., Bierman, P. R., and Rood, D. H. 2015. Meteoric ^{10}Be , clay, and extractable iron depth profiles in the Colorado Front Range: Implications for understanding soil mixing and erosion. *Catena*, 127:32–45.
- Zapata, F. 2002. *Handbook for the Assessment of Soil Erosion and Sedimentation Using Environmental Radionuclides*. Kluwer Academic, The Netherlands.
- Zech, W., Schad, P., and Hintermaier-Erhard, G. 2014. *Böden der Welt: Ein Bildatlas*. Springer, 2nd edition.
- Zhang, X., Higgitt, D. L., and Walling, D. E. 1990. A preliminary assessment of the potential for using caesium-137 to estimate rates of soil erosion in the Loess Plateau of China. *Hydrological Sciences Journal*, 35(3):243–252.
- Zollinger, B., Alewell, C., Kneisel, C., Brandová, D., Petrillo, M., Plötze, M., Christl, M., and Egli, M. 2017. Soil formation and weathering in a permafrost environment of the Swiss Alps: a multi-parameter and non-steady-state approach. *Earth Surface Processes and Landforms*, 42(5):814–835.
- Zollinger, B., Alewell, C., Kneisel, C., Meusburger, K., Brandová, D., Kubik, P., Schaller, M., Ketterer, M., and Egli, M. 2015. The effect of permafrost on time-split soil erosion using radionuclides (^{137}Cs , $^{239} + ^{240}\text{Pu}$, meteoric ^{10}Be) and stable isotopes ($\delta^{13}\text{C}$) in the eastern Swiss Alps. *Journal of Soils and Sediments*, 15(6):1400–1419.

A Appendix

Table 12: Average elemental composition from dithionite and oxalate extraction method of the individual sample sites and for all soil horizons.

Site	Soil Horizon	Depth [cm]	Dithionite Extraction		Oxalate Extraction			
			Al [mg kg ⁻¹]	Fe [mg kg ⁻¹]	Al [mg kg ⁻¹]	Fe [mg kg ⁻¹]	Mn [mg kg ⁻¹]	Si [mg kg ⁻¹]
CJ-1	A1	10 - 22	2408.5	15360	1779.5	2810	678.9	295.5
	A2	22 - 48	2437.25	16115	2436	3238.5	586.6	367.95
	A3	48 - 80	2123	17185	2099	3614.5	971.25	605.95
	AC	80 - 98	1547	21875	1139.95	1266	328.8	561.8
	C	98 - 140	1033.5	14215	1047.9	1207.5	347.85	372.25
CJ-2	A1	0 - 30	976.1	9725.5	1872	5006	443.6	678.95
	A2	30 - 53	1164	9603	1915.5	3902	446.8	730.55
	A3	53 - 89	1273.5	11905	1822	3375	616	788.4
	A4	89 - 114	1417.5	14925	1667	2883	700.8	654.05
	AC	114 - 140	1273	14905	896.55	1513.5	483.05	384.25
	C	140 - 150	1209	15985	693.65	1210.5	650.85	317.85
CJ-3	A1	0 - 39	1195.5	7867	1814	2099	502.4	336.4
	A2	39 - 84	1285.5	9541.5	1702.5	1735	465.65	346.05
	A3	84 - 120	1059.5	8910.5	1403	2080	442.2	410.35
	A(C)	120 - 145	789.2	9054	1119	1771	401.6	517.1
	AC	145 - 184	569.8	8150.5	921.85	1339	441.3	390.55
	C	184 - 195	363.4	8288	734.8	1534	354.5	452.8
CJ-4	Am	0 - 10	1713	9360.5	1714	3355.5	472.75	204.5
	AeB	10 - 23	1771	10006	1717	3117	488.4	204.45
	Bt1s	23 - 43	2681.5	13315	2263.5	1664.5	72.425	285.6
	Btzc	43 - 71	1953	12365	1695.5	807.5	1.0447	297.3
	Bmt	71 - 99	1419	12650	2025.5	891.55	98.145	363.5
	BC	99 - 127	613.35	4960.5	1384.5	490.3	198.45	415.95
	Cg	127 - 147	519.15	2036.5	1459.5	411.3	35.795	461.3

Table 13: Elemental composition from dithionite and oxalate extraction method of the individual sample sites and for all soil horizons, with two duplicates for each sample.

Sample-Nr.	Sample	Site	Horizon	Depth [cm]	Dithionite Al [mg kg ⁻¹]	Dithionite Fe [mg kg ⁻¹]	Oxalate Al [mg kg ⁻¹]	Oxalate Fe [mg kg ⁻¹]	Oxalate Mn [mg kg ⁻¹]	Oxalate Si [mg kg ⁻¹]
242C20DP-94-1	CJ1-Be1	CJ1	A1	10 - 22	2486	15320	1497	2960	685.7	304.2
242C20DP-94-2					2331	15400	2062	2660	672.1	286.8
242C20DP-95-1	CJ1-Be2	CJ1	A2	22 - 48	2518	15820	2197	3237	620.7	368.7
242C20DP-95-2					2356.5	16410	2675	3240	552.5	367.2
242C20DP-96-1	CJ1-Be3	CJ1	A3	48 - 80	2020	17520	2079	3531	907.5	575.5
242C20DP-96-2					2226	16850	2119	3698	1035	636.4
242C20DP-97-1	CJ1-Be4	CJ1	AC	80 - 98	1566.5	21670	856.9	1267	341.9	416.1
242C20DP-97-2					1527.5	22080	1423	1265	315.7	707.5
242C20DP-98-1	CJ1-Be5	CJ1	C	98 - 140	968	14050	997.8	1220	328.6	371.8
242C20DP-98-2					1099	14380	1098	1195	367.1	372.7
242C20DP-99-1	CJ2-Be1	CJ2	A1	0 - 30	972.8	9641	1837	5041	427.4	682.6
242C20DP-99-2					979.4	9810	1907	4971	459.8	675.3
242C20DP-100-1	CJ2-Be2	CJ2	A2	30 - 53	1171	9632	1977	4009	442.2	712.7
242C20DP-100-2					1157	9574	1854	3795	451.4	748.4
242C20DP-101-1	CJ2-Be3	CJ2	A3	53 - 89	1395	12000	1785	3508	622.7	773.3
242C20DP-101-2					1152	11810	1859	3242	609.3	803.5
242C20DP-102-1	CJ2-Be4	CJ2	A4	89 - 114	1430	14960	1629	2604	677.8	670
242C20DP-102-2					1405	14890	1705	3162	723.8	638.1
242C20DP-103-1	CJ2-Be5	CJ2	AC	114 - 140	1289	14930	902.3	1543	498.1	367.8
242C20DP-103-2					1257	14880	890.8	1484	468	400.7
242C20DP-104-1	CJ2-Be6	CJ2	C	140 - 150	1257	17130	686.9	1164	640	315.5
242C20DP-104-2					1161	14840	700.4	1257	661.7	320.2
242C20DP-105-1	CJ3-Be1	CJ3	A1	0 - 39	1182	8078	1854	2186	517.9	342.5
242C20DP-105-2					1209	7656	1774	2012	486.9	330.3
242C20DP-106-1	CJ3-Be2	CJ3	A2	39 - 84	1276	10300	1806	1805	460	344.2
242C20DP-106-2					1295	8783	1599	1665	471.3	347.9
242C20DP-107-1	CJ3-Be3	CJ3	A3	84 - 120	1014	8726	1378	2151	440.6	413.7
242C20DP-107-2					1105	9095	1428	2009	443.8	407
242C20DP-108-1	CJ3-Be4	CJ3	A(C)	120 - 145	847.3	9085	1077	1653	355.6	510.6
242C20DP-108-2					731.1	9023	1161	1889	447.6	523.6
242C20DP-109-1	CJ3-Be5	CJ3	AC	145 - 184	593.7	8126	901.4	1320	460.4	391.2
242C20DP-109-2					545.9	8175	942.3	1358	422.2	389.9
242C20DP-110-1	CJ3-Be6	CJ3	C	184 - 195	363.9	8305	814.2	1520	384.6	429.6
242C20DP-110-2					362.9	8271	655.4	1548	324.4	476
242C20DP-111-1	CJ4-Be1	CJ4	A	0 - 10	1645	9361	1622	3511	456.2	211.5
242C20DP-111-2					1781	9360	1806	3200	489.3	197.5
242C20DP-112-1	CJ4-Be2	CJ4	AeB	10 - 23	1823	10230	1598	2965	493.2	210.4
242C20DP-112-2					1719	9782	1836	3269	483.6	198.5
242C20DP-113-1	CJ4-Be3	CJ4	Bth	23 - 43	2608	12790	2208	1680	88.79	301.3
242C20DP-113-2					2755	13840	2319	1649	56.06	269.9
242C20DP-114-1	CJ4-Be4	CJ4	Btg	43 - 71	1945	12340	1641	821.6	0.7124	280.1
242C20DP-114-2					1961	12390	1750	793.4	1.377	314.5
242C20DP-115-1	CJ4-Be5	CJ4	Bmt	71 - 99	1381	12730	1968	907	114.6	354.3
242C20DP-115-2					1457	12570	2083	876.1	81.69	372.7
242C20DP-116-1	CJ4-Be6	CJ4	BC	99 - 127	695.4	5226	1419	451.9	140.3	415.8
242C20DP-116-2					531.3	4695	1350	528.7	256.6	416.1
242C20DP-117-1	CJ4-Be7	CJ4	Cg	127 - 147	600.7	2127	1494	362.8	35.35	437.1
242C20DP-117-2					437.6	1946	1425	459.8	36.24	485.5

Table 14: Measured meteoric ^{10}Be Inventory and inventory corrected to sample preparation blank.

	Measured							Corrected to sample preparation blank, Error includes AMS standard error		
Sample	^{10}Be counts	^9Be (LE)	$^{10}\text{Be}/^9\text{Be}$	error	Abs. error	^{10}Be	err abs.	^{10}Be	Err ^{10}Be	Err ^{10}Be
			$\times 10^{-12}$	[%]	$\times 10^{-12}$	$\times 10^6$ [at g $^{-1}$]	$\times 10^6$ [at g $^{-1}$]	$\times 10^4$ [atoms g $^{-1}$]	$\times 10^4$ [atoms g $^{-1}$]	[%]
CJ1-Be1	8539	3896	7.985	1.5	0.120	279	4	27832	813	2.9
CJ1-Be2	7789	4133	7.217	1.5	0.108	249	4	24854	726	2.9
CJ1-Be3	6024	4224	5.438	1.5	0.082	190	3	18950	554	2.9
CJ1-Be4	1383	5430	0.428	3.3	0.014	15	0	1447	61	4.2
CJ1-Be5	1754	4694	0.751	2.5	0.019	26	1	2567	92	3.6
CJ2-Be1	8379	4581	7.077	1.5	0.106	241	4	24013	701	2.9
CJ2-Be2	7784	4493	6.918	2.2	0.152	242	5	24195	807	3.3
CJ2-Be3	3912	2987	5.551	1.8	0.097	193	3	19207	588	3.1
CJ2-Be4	4853	4426	4.314	1.6	0.069	144	2	14329	427	3.0
CJ2-Be5	1487	3318	1.131	2.7	0.031	52	1	5121	191	3.7
CJ2-Be6	539	6410	0.107	4.4	0.005	4	0	332	19	5.8
CJ3-Be1	5473	2701	8.570	1.5	0.131	296	5	29513	866	2.9
CJ3-Be2	6238	3124	8.316	1.6	0.133	292	5	29184	867	3.0
CJ3-Be3	6626	3030	8.339	1.5	0.125	284	4	28321	827	2.9
CJ3-Be4	7958	4223	7.329	1.5	0.110	254	4	25389	742	2.9
CJ3-Be5	4198	3686	4.755	1.7	0.081	168	3	16787	509	3.0
CJ3-Be6	2736	4602	2.349	2.0	0.048	81	2	8078	262	3.2
CJ4-Be1	10231	2867	14.621	1.5	0.219	506	8	50540	1475	2.9
CJ4-Be2	10966	2989	15.440	1.5	0.232	490	7	48987	1430	2.9
CJ4-Be3	10106	2973	14.412	1.5	0.216	507	8	50658	1478	2.9
CJ4-Be4	8882	3074	12.184	1.5	0.183	435	7	43424	1267	2.9
CJ4-Be5	9508	2542	16.370	1.5	0.246	565	8	56457	1647	2.9
CJ4-Be6	14840	3107	19.782	1.5	0.297	716	11	71530	2087	2.9
CJ4-Be7	10663	2417	19.043	1.5	0.286	650	10	64925	1894	2.9

Table 15: Measured in-situ ^{10}Be values and corrected to blank preparation sample.

Sample	Measured Values						Corrected to sample preparation blank, Error includes AMS standard error					
	^{10}Be	^9Be	$^{10}\text{Be}/^9\text{Be}$ final	error	^{10}Be	Absolute error	$^{10}\text{Be}/^9\text{Be}$ corr Lab blk	Absolute error	^{10}Be	Err ^{10}Be	Error ^{10}Be	
	counts	counts	$\times 10^{-12}$	[%]	$\times 10^4$ [atoms g^{-1}]	$\times 10^4$ [atoms g^{-1}]	$\times 10^{-12}$	$\times 10^{-12}$	$\times 10^4$ [atoms g^{-1}]	$\times 10^4$ [atoms g^{-1}]	[%]	
CJ-Be11	665	7965	0.056	0.039	3.87	0.152	0.045	0.003	3.11	0.18	5.91	
CJ-Be12	683	6319	0.072	0.058	4.92	0.284	0.061	0.005	4.17	0.31	7.48	
CJ-Be13	755	7052	0.073	0.048	4.97	0.239	0.062	0.004	4.22	0.27	6.44	
Preparation blank	179	10314	0.011	0.086	0	0	0	0	0	0	0	

Table 16: Input data for the in-situ ^{10}Be exposure age calculation

Sample	Latitude	Longitude	Altitude	Height above surface	Inclination	Average sample thickness	Topographic Shielding Factor	^{10}Be conc.	^{10}Be conc. Error	Sample density
	[°]	[°]	[m a.s.l.]	[cm]	[°]	[cm]	[-]	[atoms g^{-1}]	[atoms g^{-1}]	[g cm^{-3}]
CJ-Be11	46.531333	23.574167	430	15	70	1.3	0.724	31141	1840	2.7
CJ-Be12	46.531333	23.574167	430	70	60	1.6	0.818	41700	3121	2.7
CJ-Be13	46.531333	23.574167	430	105	40	1.4	0.945	42184	2717	2.7

Table 17: Grain size distribution of a subset of soil samples.

Sample	Site	Horizon	Depth [cm]	<2000 μm [%]	<1000 μm [%]	<500 μm [%]	<250 μm [%]	<125 μm [%]	<63 μm [%]	<45 μm [%]	<32 μm [%]	<28.5 μm [%]	<25 μm [%]	<20 μm [%]	<15 μm [%]
DP94	CJ1	A	10 - 22	100	99.6	99.3	95.5	89.6	72	63.1	56.4	56.5	56.5	55.6	54
DP96	CJ1	A2	48 - 80	100	100	100	98.9	90.9	71.8	65.6	31.9	31.8	31.7	31.3	30.4
DP98	CJ1	C	98-140	100	100	100	99.8	96.9	84.5	41.4	35.7	35.7	35.5	35.2	34.1
DP99	CJ2	A1	0 - 30	100	99.5	99.1	96.6	91.6	72.2	60.5	52.9	52.9	52.8	52.2	50.2
DP101	CJ2	A3	53 - 89	100	99.8	99.8	99.5	93.3	77.1	70	62.2	62.2	62	60.6	57.9
DP104	CJ2	C	140 - 150	100	100	100	98.8	99.1	96.5	92.5	87.1	86.8	86.6	85.5	82.9
DP105	CJ3	A1	0 - 39	100	99.6	98.7	95.3	70.7	48.2	39.3	32	32.1	31.9	30.5	28.6
DP107	CJ3	A3	84 - 120	100	99.8	99.1	96.7	85.8	66	54.7	47.1	47.1	47.1	46.3	44.6
DP110	CJ3	C	184 - 195	100	99.6	98.9	96.2	88.7	71.5	62.9	52.5	52.2	51.9	51	49.1
DP111	CJ4	A	0 - 10	100	99.5	98.7	96.2	87.6	66	55.1	48	47.8	47.2	45.7	43.1
DP114	CJ4	Btg	43 - 71	100	99.6	98.4	93.1	83.5	63.5	56.2	48.7	48.6	49.2	50.3	49
DP117	CJ4	C	127 - 147	100	100	100	98.4	92.2	78.7	67.8	60.7	60.7	60.4	59.4	57.4
Sample	Site	Horizon	Depth [cm]	<10 μm [%]	<8 μm [%]	<7 μm [%]	<6 μm [%]	<5 μm [%]	<4 μm [%]	<3 μm [%]	<2 μm [%]	<1.5 μm [%]	<1 μm [%]	<0.5 μm [%]	<0.009 μm [%]
DP94	CJ1	A	10 - 22	50.6	49.1	48	46.7	45.1	43.2	40.9	37.6	35.5	32.3	32.3	32.3
DP96	CJ1	A2	48 - 80	28.7	27.9	27.4	26.7	25.9	24.8	23.5	21.5	20.2	18.5	18.5	18.5
DP98	CJ1	C	98-140	32	30.6	29.6	28.5	27.1	25.3	23	19.9	18	16	16	16
DP99	CJ2	A1	0 - 30	47.1	45.6	44.6	43.5	42.2	40.6	38.8	36	34.1	31.8	31.8	31.8
DP101	CJ2	A3	53 - 89	53.9	51.5	50.1	48.7	47.2	45.2	42.9	39.8	37.6	34.6	34.6	34.6
DP104	CJ2	C	140 - 150	78.3	75.1	72.9	70.2	67.1	62.9	56.9	48	42.6	37.3	37.3	37.3
DP105	CJ3	A1	0 - 39	26.5	25.1	24.5	23.8	23	22.1	21.2	19.9	18.9	16.8	16.8	16.8
DP107	CJ3	A3	84 - 120	41.8	40.3	39.4	38.5	37.3	35.9	34.2	31.5	29.5	27.3	27.3	27.3
DP110	CJ3	C	184 - 195	46	44.4	43.4	42.3	41.1	39.6	37.8	34.8	32.7	29.9	29.9	29.9
DP111	CJ4	A	0 - 10	39.4	37.6	36.5	35.4	34.1	32.6	30.9	28.6	27.1	24.9	24.9	24.9
DP114	CJ4	Btg	43 - 71	46.9	45.9	45.4	44.9	44.2	43.3	42.4	40.7	39.6	38.5	38.5	38.5
DP117	CJ4	C	127 - 147	54	52.6	51.9	50.8	50	49.1	48.1	46.5	45.3	43.2	43.2	43.2

Table 20: Measured and corrected plutonium contents and activities, batch 3

Batch 3		Measured activities and isotopic ratios										Activity corrected to average preparation blank and to standard IAEA-447			
Field sample name	Lab sample name	²⁴² Pu		²³⁹ Pu activity		²⁴⁰ Pu activity		²³⁹ Pu+ ²⁴⁰ Pu activity		²⁴⁰ Pu/ ²³⁹ Pu		²³⁹ Pu+ ²⁴⁰ Pu activity		²⁴⁰ Pu/ ²³⁹ Pu	
		CPS	RSD, %	Bq kg ⁻¹	RSD, %	Bq kg ⁻¹	RSD, %	Bq kg ⁻¹	RSD, %	mass ratio	RSD, %	Bq kg ⁻¹	RSD, %	mass ratio	RSD, %
3-D3	DP71	29221.0	4.0	0.1318	7.0	0.0982	16.7	0.2300	17.6	0.2013	17.2	0.2607	18.0	0.2015	17.2
3-D4	DP72	25385.0	1.8	0.0948	10.9	0.0620	34.4	0.1568	36.1	0.1767	36.0	0.1777	36.3	0.1769	36.1
Blank sample	BLK7	30110.0	0.9	0	0	0	0	0	0	0	0	0	0	0	0
4-A1	DP73	33739.4	2.2	0.1320	8.0	0.0958	15.3	0.2278	17.1	0.1959	16.9	0.2582	17.5	0.1961	17.0
4-A2	DP74	26877.1	1.6	0.1323	5.1	0.0935	15.5	0.2257	16.2	0.1909	16.1	0.2559	16.6	0.1911	16.2
4-A3	DP75	30109.7	3.2	0.1224	6.8	0.0847	17.4	0.2070	18.4	0.1868	18.1	0.2347	18.8	0.1870	18.2
4-A4	DP76	30518.3	6.5	0.0555	13.6	0.0403	17.7	0.0958	21.4	0.1959	20.4	0.1085	21.8	0.1963	20.4
Standard IAEA-447	STD7	6415.1	2.3	2.6120	6.2	1.8866	7.8	4.4986	9.8	0.1950	9.5	5.1052	10.4	0.1950	9.5
4-A5	DP77	19515.2	1.5	0.0022	21.6	0.0003	316.2	0.0025	316.9	0.0315	316.9	0.0025	417.0	0.0267	375.9
4-B1	DP78	31780.2	1.4	0.1388	6.9	0.0980	20.6	0.2368	21.7	0.1905	21.7	0.2684	22.0	0.1907	21.8
4-B2	DP79	25264.1	2.2	0.1304	7.3	0.1018	16.9	0.2322	18.3	0.2108	18.2	0.2633	18.7	0.2110	18.3
4-B3	DP80	24752.7	1.5	0.1044	10.4	0.0822	20.4	0.1865	22.8	0.2125	22.8	0.2114	23.1	0.2128	22.8
Rock powder	NC7	18856.1	3.6	0.0433	20.4	0.0318	36.7	0.0751	41.8	0.1983	41.7	0.0850	42.1	0.1988	41.7
4-B4	DP81	28379.4	1.3	0.0425	17.1	0.0355	23.8	0.0779	29.3	0.2256	29.3	0.0882	29.7	0.2263	29.3
4-C1	DP82	28414.8	2.0	0.1363	9.3	0.1089	21.9	0.2452	23.7	0.2157	23.6	0.2780	24.0	0.2159	23.7
4-C2	DP83	30390.7	1.9	0.1440	6.8	0.1125	15.4	0.2565	16.7	0.2109	16.6	0.2908	17.1	0.2111	16.7
4-C3	DP84	27163.8	5.1	0.1324	9.3	0.1091	15.1	0.2415	17.0	0.2225	16.2	0.2738	17.4	0.2228	16.3
4-C4	DP85	21345.6	2.2	0.0711	11.3	0.0476	28.6	0.1187	30.7	0.1810	30.6	0.1344	30.9	0.1813	30.7
Blank sample	BLK8	31008.6	0.7	0	0	0	0	0	0	0	0	0	0	0	0
4-D1	DP86	24886.4	1.1	0.2508	5.9	0.1907	13.0	0.4416	14.3	0.2053	14.2	0.5008	14.7	0.2054	14.3
4-D2	DP87	23432.9	2.2	0.1097	10.0	0.0769	29.0	0.1866	30.6	0.1891	30.5	0.2115	30.8	0.1893	30.6
4-D3	DP88	25952.5	1.7	0.0557	8.0	0.0435	37.8	0.0991	38.6	0.2107	38.6	0.1122	38.9	0.2112	38.7
4-D4	DP89	23688.0	2.4	0.0322	22.6	0.0255	35.8	0.0577	42.3	0.2135	42.2	0.0652	42.6	0.2143	42.2
Standard IAEA-447	STD8	5167.0	1.5	2.7220	4.6	1.9515	13.0	4.6735	13.7	0.1936	13.6	5.3037	14.2	0.1936	13.7
4-E1	DP90	24585.7	0.8	0.1451	5.1	0.1111	19.5	0.2562	20.1	0.2067	20.1	0.2905	20.5	0.2069	20.2
4-E2	DP91	20136.6	1.9	0.1338	11.6	0.0965	21.9	0.2303	24.7	0.1948	24.6	0.2610	25.0	0.1950	24.7
4-E3	DP92	25701.9	1.6	0.1127	7.3	0.0902	18.8	0.2029	20.1	0.2162	20.0	0.2300	20.4	0.2164	20.1
4-E4	DP93	22006.4	1.2	0.0558	17.1	0.0398	30.9	0.0956	35.3	0.1924	35.3	0.1082	35.6	0.1928	35.4
Rock powder	NC8	22438.6	1.8	0.0431	14.1	0.0305	37.0	0.0736	39.6	0.1907	39.6	0.0832	39.9	0.1913	39.6
Duplicate of 3-D4/DP72	DUP9	27021.2	1.9	0.0867	8.1	0.0661	16.7	0.1528	18.5	0.2060	18.4	0.1731	18.9	0.2063	18.4
Duplicate of 4-A1/DP73	DUP10	24737.0	2.2	0.1348	6.6	0.1033	22.8	0.2381	23.6	0.2068	23.5	0.2699	23.9	0.2070	23.6
Duplicate of 4-D3/DP88	DUP11	22541.5	2.1	0.0559	12.0	0.0396	20.1	0.0955	23.3	0.1915	23.2	0.1081	23.6	0.1919	23.3
Duplicate of 4-E4/DP93	DUP12	23290.7	1.7	0.0624	8.2	0.0434	32.4	0.1058	33.4	0.1880	33.4	0.1198	33.7	0.1884	33.4

Table 21: Short-term soil erosion rate calculated with fallout $^{239+240}\text{Pu}$.

		IM, Lal et al. (2013)	IM, Lal et al. (2013) P=1	IM, Lal et al. (2013) P=1.2	IM, Lal et al. (2013) P=1.5	PDM, Walling and He (1999)	MODERN, Arata et al. (2016b)
Site	Replicates	L=soil loss [cm]	t ha ⁻¹ yr ⁻¹	t ha ⁻¹ yr ⁻¹	tt ha ⁻¹ yr ⁻¹	t ha ⁻¹ yr ⁻¹	t ha ⁻¹ yr ⁻¹
CJ1	1	1.42	2.35	1.96	1.57	4.11	7.20
	2	1.23	1.94	1.62	1.29	3.55	
	3	1.02	1.70	1.42	1.13	2.95	
	4	4.66	8.02	6.69	5.35	13.48	
	Average	2.08	3.50	2.92	2.34	6.02	
	SD	1.73	3.02	2.52	2.02	5.00	
	SE	1.96	2.59	2.36	2.11	3.33	
CJ-2	1	1.46	2.39	1.99	1.59	4.21	7.53
	2	0.99	1.52	1.27	1.02	2.86	
	3	0.95	1.33	1.11	0.89	2.73	
	4	7.53	12.94	10.78	8.63	21.76	
	Average	2.73	4.55	3.79	3.03	7.89	
	SD	3.21	5.62	4.68	3.74	9.27	
	SE	2.67	3.53	3.22	2.88	4.53	
CJ-3	1	1.04	1.79	1.49	1.20	3.02	5.19
	2	1.60	2.82	2.35	1.88	4.62	
	3	1.26	2.12	1.76	1.41	3.64	
	4	1.07	1.78	1.48	1.19	3.09	
	Average	1.24	2.13	1.77	1.42	3.59	
	SD	0.26	0.49	0.41	0.33	0.74	
	SE	0.75	1.04	0.95	0.85	1.28	
CJ-4	1	0.70	1.60	1.33	1.07	2.03	2.78
	2	0.48	1.21	1.00	0.80	1.38	
	3	0.14	0.31	0.25	0.20	0.39	
	4	0.05	0.12	0.10	0.08	0.14	
	5	0.95	2.02	1.68	1.35	2.74	
	Average	0.46	1.05	0.88	0.70	1.34	
	SD	0.38	0.82	0.68	0.55	1.09	
	SE	0.92	1.35	1.23	1.10	1.56	

R Code MODERN by Arata et al. (2016b), modified for this thesis

```
install.packages("modeRn", repos = NULL, type="source")
# load the library
library("modeRn")

#creates a reference profile composed of 4 layers of thickness 5 cm
RDP = createReferenceProfile(FRNinv = c(24.15, 21.09, 10.19, 5.86), thickness =
5, name = 'Reference site', falloutTime = 1963, refTime = '2020-10-01', massDepth = 217.29)
plot(RDP)
print(RDP)

#creates sampling layers of thickness 20 cm
CJ1 = createSamplingProfile(FRNinv = 41.83, thickness = 20, name = 'Site 1',
falloutTime = 1963, refTime = '2020-10-1', massDepth = 178.76)
CJ2 = createSamplingProfile(FRNinv = 39.90, thickness = 20, name = 'Site 2'
, falloutTime = 1963, refTime = '2020-10-1')
CJ3 = createSamplingProfile(FRNinv = 47.66, thickness = 20, name = 'Site 3',
falloutTime = 1963, refTime = '2020-10-1')
CJ4 = createSamplingProfile(FRNinv = 55.93, thickness = 20, name = 'Site 4',
falloutTime = 1963, refTime = '2020-10-1')
print(CJ1)

# creates smoothed layers below the reference profile
RDPsmooth1 = addSmoothedLayers(RDP, CJ1)
plot(RDPsmooth1, main = 'Simulated depth profile')

RDPsmooth2 = addSmoothedLayers(RDP, CJ2)
plot(RDPsmooth2, main = 'Simulated depth profile')

RDPsmooth3 = addSmoothedLayers(RDP, CJ3)
plot(RDPsmooth3, main = 'Simulated depth profile')

RDPsmooth4 = addSmoothedLayers(RDP, CJ4)
```

```

plot(RDPsmooth4, main = 'Simulated depth profile')

# sampling profiles with eroded layers
MODERNCJ1 = MODERN(RDPsmooth1, CJ1)
png("moderncj1.png", pointsize = 10, width = 2000, height = 960, res = 350)
plot(RDPsmooth1, main = 'Simulated depth profile')
plot(MODERNCJ1)
dev.off()
print(MODERNCJ1)
ER1 <-yearlyEDRates(MODERNCJ1, samplingTime = '2020', falloutTime = '1963', massDepth
=
178.76, sampleDepth = 20)

show(ER1)

MODERNCJ2 = MODERN(RDPsmooth2, CJ2)
png("moderncj2.png", pointsize = 10, width = 2000, height = 960, res = 350)
plot(RDPsmooth2, main = 'Simulated depth profile')
plot(MODERNCJ2)
dev.off()
print(MODERNCJ2)
ER2 <-yearlyEDRates(MODERNCJ2, samplingTime = 2020, falloutTime = 1963, massDepth =
170.09, sampleDepth = 20)
show(ER2)

MODERNCJ3 = MODERN(RDPsmooth3, CJ3)
png("moderncj3.png", pointsize = 10, width = 2000, height = 960, res = 350)
plot(RDPsmooth3, main = 'Simulated depth profile')
plot(MODERNCJ3)
dev.off()
print(MODERNCJ3)
ER3 <- yearlyEDRates(MODERNCJ3, samplingTime = '2020', falloutTime = '1963', massDepth
= 184.18, sampleDepth = 20)
show(ER3)

```

```

MODERNCJ4 = MODERN(RDPsmooth4, CJ4)
png("moderncj4.png", pointsize = 10, width = 2000, height = 960, res = 350)
plot(RDPsmooth4, main = 'Simulated depth profile')
plot(MODERNCJ4)
dev.off()
print(MODERNCJ4)
ER4 <- yearlyEDRates(MODERNCJ4, samplingTime = 2020, falloutTime = 1963, massDepth =
250.88, sampleDepth = 20)
show(ER4)

```

R Code Soil Depth Computation by Egli et al. (2018), modified for this thesis

#clean environment

```
rm(list=ls())
```

#loading input file

#contains all the input parameters for modelling soil depth

```
input<-read.csv(" /Documents/UZH/Master Thesis/soilDepth/
master/input/inputRomania.csv", sep=";", header = TRUE)
```

#for performance reasons only selecting ten random parameter settings

```
input.s<-input[sample(1:nrow(input),size = 4,replace = F),]
```

#function to compute soil depth

```
soilDepthComp<-function(part,I,erosion,yearMax)
```

#compute

```

year<-1:yearMax

soilDepth<-numeric()
soilProd<-numeric()
soilDepthEr<-numeric()

soilDepth[1]<-part*(year[1]/(part/I))^ 0.53
soilDepth[2]<-part*(year[2]/(part/I))^ 0.53

soilProd[1]<-NA
soilProd[2]<-I*(1/1.87)*(part/soilDepth[2])^ .87

soilDepthEr[1]<-NA
soilDepthEr[2]<-soilDepth[1]

for(i in 3:max(year))
soilDepth[i]<-part*(year[i]/(part/I))^ 0.53
soilProd[i]<-I*(1/1.87)*(part/soilDepthEr[(i-1)])^ 0.87
soilDepthEr[i]<-soilDepthEr[(i-1)]+(soilProd[i])-(erosion)

results<-data.frame(year=year,sP=soilProd,sDE=soilDepthEr)
return(results)

#empty data.frame with all required information
all<-data.frame(Site=NA,
ProfileName=NA,
part=NA,
I=NA,
erosion=NA,
yearMax=NA,
year=NA,
sP=NA,

```

```
sDE=NA)
```

```
#computing soil depth
```

```
#executing soildepth-function for the small dataset
```

```
for(i in 1:nrow(input.s))
```

```
print(i)
```

```
results<-soilDepthComp(input$ part[i],input$ I[i],input$ erosion[i],input$ yearMax[i])
```

```
resI<-results[results$ year==input$ yearMax[i],]
```

```
all<-rbind(all,cbind(input[i,],resI))
```

```
all<-all[-1,]
```

```
all.df<-all
```

```
#writing results to csv
```

```
write.csv(all.df, " /Documents/UZH/Master Thesis/soilDepth-master/output/soilDepth.txt")
```

Acknowledgements

In the one year that I planned, carried out and wrote my Master's thesis, there were many who helped me with this project. Without them, this work would not be what it is now.

First and foremost, I would like to thank my supervisor Prof. Markus Egli for his support during the whole process, for the extremely quick answers to questions and the very helpful and detailed feedback which has always helped in keeping me motivated during the entire project.

A huge thank you to Prof. Pavel Šamonil for letting me participate in his extremely exciting project and having me in his team, for the extraordinarily great and exciting fieldwork in Romania, the hospitality at the VUKOZ in Brno and the many inputs and feedbacks on my work! Also a big thank you goes to the whole project team that was in Romania for a great team experience, inspiring moments that showed me that this is what I want to do and for the support in the field. A special thank you goes to Dr. Pavel Daněk for the great photos of the field trip.

During my measurements and examinations in the laboratory, I could always count on the guidance and support of Dr. Dmitry Tikhomirov. In addition, he took over the extractions of the in-situ ^{10}Be as well as all measurements of the ^{10}Be and the $^{239+240}\text{Pu}$ for me. Many thanks for that, I would probably have been lost without him.

The grain size distribution as well as the extractions were carried out by our laboratory technician Esmail Taghizadeh, many thanks for this effort!

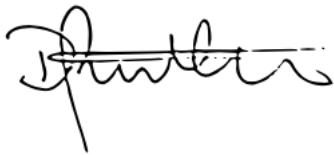
Thank you to all my fellow students for entertaining distracting moments, inspiring coffee breaks and relaxing lunches, you have made the weeks of master thesis writing much more enjoyable!

A very big thank you goes to my family, especially my parents, who made all this possible for me, for their time, encouraging words and support. Thank you for everything!

And last but not least, a big thank you to my girlfriend Sofie for putting up with my bad moods while I was writing!

Personal Declaration

I hereby declare that the submitted Thesis is the result of my own, independent work. All external sources are explicitly acknowledged in the Thesis.

A handwritten signature in black ink, appearing to read 'Dario Püntener', written in a cursive style.

Dario Püntener

Zürich, 20.09.2021